Far-field method for the characterisation of three-dimensional fields: vectorial polarimetry

Oscar Gabriel Rodríguez Herrera

Supervisor:
Prof. Chris Dainty

National University of Ireland, Galway
Ollscoil na hÉireann, Gaillimh

A thesis submitted in partial fulfilment of the requirements
for the degree of Doctor of Philosophy,

School of Physics, College of Science,
National University of Ireland, Galway

August 2009

Contents

Abstract

In the search for increasing the resolution of an optical system it is usually necessary to increase its numerical aperture (NA). For high NA the scalar theory of diffraction is no longer applicable and the vectorial nature of the electromagnetic (EM) field cannot be ignored. In this case, the EM field in the focal region of the system must be described using a vectorial theory of diffraction.

An important consequence of focusing with high NA, as predicted by the vectorial theory of diffraction, is the appearance of a longitudinal component of the field, comparable to the transversal components in the focal region. In conventional polarisation microscopy, even when high NAs are used, only the transversal components are considered for the analysis of the specimen. Although this approach has been proved to be adequate in a number of applications, it ignores the potentially valuable information contained in the longitudinal component.

The Z-polarized microscope, introduced by Huse *et al.* [J. Biomed. Opt. 6 (2001) 480], showed the other side of the approach. That is, the Z-polarized microscope only considered the interaction of the longitudinal component with the sample, ignoring the information contained in the transversal components.

In this work, we present an alternative far-field method for the analysis of the three-dimensional EM field resulting from the interaction of a tightly focused field and a sub-resolution scatterer. The method proposed here is based on the analysis of the scattering-angle-resolved polarisation state distribution across the exit pupil of a high NA objective lens and it is proved to yield high sensitivity in sub-resolution displacements of a sub-resolution specimen.

Acknowledgements

I am obliged to my supervisor, Prof. Chris Dainty, for his support, guidance, encouragement and fruitful discussions. I am also indebted to Dr. David Lara Saucedo for his support, guidance and comments as well as for all the discussions that we had since he came up with the idea that originated this work.

I thank Dr. Sumio Kumashiro for stimulating discussions on the different aspects of the project and Mr. Masahiro Takebe for discussions on FDTD modelling.

This project was funded by the Mexican National Council for Science and Technology (CONACYT), PhD scholarship No. 177627, Science Foundation Ireland (SFI), grants 01/PI.2/B039C and 07/IN.1/I906, and Shimadzu Corporation, Japan.

List of acronyms

ABC	Absorbing Boundary Condition
CCD	Charge Coupled Device
CMMP	Confocal Mueller Matrix Polarimeter
DDA	Discrete Dipole Approximation
DP-ECM	Double-Pass Eigenvalue Calibration Method
ECM	Eigenvalue Calibration Method
EM	Electromagnetic
ENZ	Extended Nijboer-Zernike
FDTD	Finite-Difference Time-Domain
FFT	Fast Fourier Transform
FPS	Frames Per Second
NA	Numerical Aperture
NTFF	Near- to Far-Field Transformation
PEC	Perfect Electric Conductor
PSA	Polarisation State Analyser
PSF	Point-Spread-Function
PSG	Polarisation State Generator
SLM	Spatial Light Modulator
STED	Stimulated Emission Depletion

Chapter 1

Introduction

The objective of the *vectorial polarimetry* method is to obtain sub-resolution information about the specimen under observation. Because of the large number of systems that have been built to image sub-resolution objects, it is appropriate to start with a review of the high resolution microscopy techniques currently available. As we shall see, the range and nature of the techniques is broad, as well as their applications.

In the second part of this chapter we shall discuss the concept of polarimetry, which includes the polarisation formalism used in this research and the principles of Mueller matrix polarimetry. Finally, we shall conclude with an introduction to the technique that we call *vectorial polarimetry*.

1.1 High resolution microscopy

Recent developments in areas such as nano-technology and biological sciences have increased the need of high resolution imaging techniques for the analysis of small structures. In this section we discuss some of the high resolution microscopy techniques currently available although it is not, and it does not intend to be, a comprehensive review.

Among the most popular high resolution imaging instruments are the electron microscope, the tunneling microscope [1] and the atomic force microscope [2]. These microscopes have resolutions as small as a fraction of a nanometer but they present drawbacks that limit their application. The electron microscope, for instance, is an excellent method to image specimens made of, or coated with, a good electric conductor. If the specimen is made of a bad electric conductor, as it is the case for biological samples, it has to be carefully prepared before the analysis. The prepara-

tion of the sample may introduce artefacts in the image of the specimen. Thus, electron microscopy is not always suitable for the analysis of biological samples. The tunneling microscope, on the other hand, works with specimens made with a good electric conductor or a semiconductor limiting, as well, the range of applications where this instrument can be used. Finally, the atomic force microscope, although does not have limitations on the material of which the specimen has to be made, relies on the correct choice of the tip for the required resolution, complicating the acquisition of good quality images of an unknown specimen.

The maximum resolution of far-field optical microscopes working in the linear regime is limited by the diffraction limit. Therefore, the maximum transversal resolution according to Rayleigh's criterion is $\approx 0.61\lambda/\mathrm{NA}$, where λ is the wavelength of the light and NA is the numerical aperture of the objective, whereas the longitudinal resolution is $\approx \lambda/(\mathrm{NA})^2$ [3]. Attempts to overcome these limits have produced a large number of different microscopy techniques based on linear and non-linear optical phenomena.

Since the NA is related to the maximum resolution of an optical system, it is possible to increase the resolution of an optical microscope by increasing its NA. The use of oil-immersion and solid-immersion microscope objectives to increase the NA, and thus the resolution of optical microscopes, has become a standard technique.

According to the vectorial theory of diffraction [4], the electromagnetic (EM) field distribution in the focal region of a lens depends, also, on the polarisation state of the incident light. This property becomes important for large values of the NA. Therefore, the reduction of the point-spread-function (PSF) using radial polarisation [5], annular apertures [6] and the combination of both [7], in a high NA objective lens, has been proposed as a way to increase the resolution. It has also been proposed the use of evanescent wave illumination combined with synthetic-aperture microscopy [8] or optical diffraction tomography [9] as an alternative way to increase the resolution. To our knowledge, the former has been proved experimentally whereas the latter is pending for experimental verification.

One of the most influential inventions of the last century, concerning the field of optical microscopy, is the confocal microscope [10]. Its capability to image objects in three dimensions has made it one of the most used microscopy techniques. The resolution of the confocal microscope is strongly dependent of the detector size, ideally a point detector. However, as Hell pointed out [11], the confocal microscope does not break

the diffraction limit but rather pushes diffraction to its limits. Another high resolution imaging technique that allows three-dimensional imaging of the sample is optical coherence tomography (OCT) [12]. In this case, the depth resolution depends on the coherence length of the illumination and broadband sources are used for high resolution imaging.

Some of the most popular microscopy techniques nowadays, due to the high resolutions that can be achieved, are based on non-linear phenomena. Stimulated-emission-depletion (STED) fluorescence microscopy [13] and two-photon absorption microscopy are two of the most used. In the following sections we shall discuss briefly the working principle of these two techniques without going deep into the details.[1]

1.1.1 STED fluorescence microscopy

Fig. 1.1 shows the energy levels involved in the absorption and emission processes of a typical fluorophore. S_0 is the ground state and S_1 is the first excited electronic state. L_0 is the low vibrational level of S_0 and L_3 its higher level. L_1 and L_2 are the directly excited and the relaxed vibrational levels, respectively, of S_1. Einstein's equations govern the absorption and emission of the fluorophore. In a typical fluorescence scanning microscope, the fluorophores within the excited area spontaneously decay and emit light that is collected and focused onto a point detector. A complete image is obtained by scanning the specimen. The resolution of such systems is related to the area covered by the PSF of the focusing lens. Thus, one way to increase the resolution of a fluorescence microscope is by reducing the area of the specimen that participates in the fluorescence.

The STED technique uses a secondary beam, known as the STED beam, to stimulate the emission of the fluorophores in the outer region of the excitation area before fluorescence occurs. Since only the fluorophores in the central region of the excitation area contribute to the fluorescence signal, the STED beam increases the resolution of the microscope. In the original STED microscope, four mirrors were used to split the STED beam, which was then focused in different positions of the outer region of the excitation area. Currently, STED fluorescence microscopes use doughnut modes for the STED beam [14], allowing a more uniform illumination of the outer region.

Because of the nature of the technique, the excitation and STED

[1]For a comprehensive discussion on non-linear high resolution microscopy techniques the reader is referred to Stefan Hell's work [11].

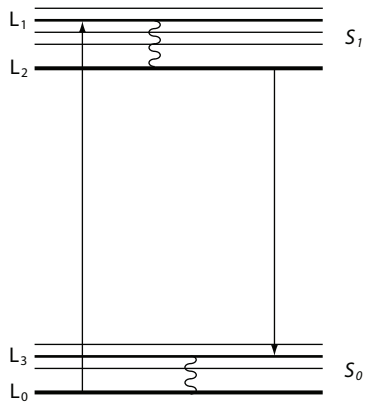

Figure 1.1: Energy levels of a typical fluorophore.

beams are pulsed laser beams. In a typical fluorophore, the average fluorescence lifetime is of the order of 2ns. Additionally, the vibrational relaxations $L_1 \rightarrow L_2$ and $L_3 \rightarrow L_0$ occur in, approximately, 1-5ps. For a maximum efficiency of the method, it is desirable for the STED beam to stimulate the emission of the fluorophores in the outer region as soon as they undergo the vibrational transition $L_1 \rightarrow L_2$. This can be achieved by using short pulses for the excitation and STED beams and choosing the appropriate time delay Δt between them. The duration of the STED pulses is, preferably, longer than 1-5ps since the rate at which L_2 can be depleted depends on the average lifetime of L_3. Resolutions as small as 35nm are achievable with STED fluorescence microscopy.

1.1.2 Two-photon absorption microscopy

Single-photon fluorescence microscopy may cause photo-bleaching and/or photo-damage to the specimen if its absorption band is close to the absorption wavelength of the fluorophores. To avoid these effects, two-photon fluorescence microscopy may be used. In this technique, the excitation of the fluorophores is done by the absorption of two photons with half the energy necessary for one photon fluorescence. In this way, the illumination wavelength is moved away from the absorption band of the specimen. Fig. 1.2 is a diagram of the energy levels for two-photon absorption of a typical fluorophore.

Two-photon fluorescence microscopy requires simultaneous absorption of two photons by the fluorophore. To satisfy this condition it is necessary to place the fluorophore in a region with high density of photons. The focal region of a lens illuminated with a short pulses laser is

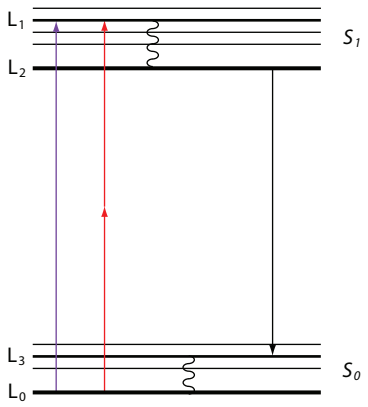

Figure 1.2: Energy levels of a typical fluorophore in single-photon and two-photon absorption. The purple arrow represents single-photon absorption whereas the two red arrows represent two-photon absorption.

a good candidate. Because of the distribution of photons in the focal region, only a small volume around the focus has a sufficiently high density for two-photon absorption to take place. Thus, the detected fluorescence comes from that small volume increasing significantly the lateral and longitudinal resolutions of the microscope.

Another two-photon absorption-based technique can be found in the work by Ramsay *et al.* [15]. In this work, instead of fluorescence, the detected signal is the current generated by the sample upon absorption of two photons. The nature of this technique makes it suitable for the analysis of integrated circuits. Resolutions below 1µm, at a wavelength $\lambda = 1530$nm, have been reported with a relatively low NA objective (NA=0.55) by combining it with a solid-immersion lens (SIL) designed with the standard prescription given to obtain the maximum NA [3].

A further improvement of this technique is of interest to us since it makes use of the properties of tightly focused polarised light. The asymmetric irradiance distribution in the focal region of a high NA lens for incident light linearly polarised [16], suggests an increment of the resolution in the direction orthogonal to the incident polarisation, as stated by Richards and Wolf. Using this property of tightly focused linearly polarised light, Serrels *et al.* [17] increased the resolution of the method presented by Ramsay *et al.*

1.2 Polarimetry

In the last decades, the study of light polarisation has gained importance due to the high sensitivity of characterisation techniques based on the measurement of the change in the polarisation state as result of the interaction with a sample. The range of techniques where the measurement of the polarisation state of a light beam is used as the method to analyse the sample is known as polarimetry. As a starting point to our discussion on polarimetry, we shall present the basics of the formalism used in this work.

1.2.1 Diattenuation and retardance

Two important concepts in polarimetry are those of diattenuation and retardance. Since these concepts are extensively used in this work, it is appropriate to present their definition.

The diattenuation of an optical element is the dependence of its transmittance on the incident polarisation state. The operational definition of the diattenuation, as given by Chipman [18], is:

$$D \equiv \frac{|\tau_q - \tau_r|}{\tau_q + \tau_r} \tag{1.1}$$

where τ_q and τ_r are the transmittances for the element's eigenpolarisations. With this definition, the possible values for the diattenuation are in the range $0 \leq D \leq 1$, where $D = 1$ corresponds to a perfect polariser and $D = 0$ to an optical element with no transmittance dependence on the incident polarisation state.

Retardance is the relative phase difference introduced to the eigenpolarisations by an optical element. The corresponding operational definition, as given by Chipman [18], is:

$$R \equiv |\delta_q - \delta_r| \tag{1.2}$$

where δ_q and δ_r are the phase change for the eigenpolarisations. The possible values for the retardance are in the range $0 \leq R \leq \pi$. In a wave-plate, the direction of the polarisation component that emerges with the leading phase is said to be along the direction of the fast axis, whereas the component polarised in the orthogonal direction is said to be along the direction of the slow axis. Thus, the fast axis is the direction for which the component of an incident wave polarised in this direction travels fastest within the wave-plate.

1.2.2 Stokes vectors and Mueller matrices

The polarisation properties of an object, as well as the polarisation state of a light beam, can be described in different ways. One possibility is to represent the object with a matrix and the beam with a vector. The interaction of the light beam with the object is then represented by the product of the matrix and the vector. Jones formalism [3] is a suitable tool to describe this interaction as long as the object is non-depolarising. Thus, Jones formalism is limited in the range of objects and light beams that can be described. A more general formalism is given by the combination of the Mueller matrix and the Stokes vectors.

The Stokes parameters, i.e. the elements of the Stokes vectors, were introduced by Sir George Stokes as a set of measurable quantities that describe the polarisation state of a light beam for completely polarised, partially polarised and unpolarised light. The definition of the Stokes vector, for quasi-monochromatic light, is [19]:

$$\mathbf{S} = \begin{pmatrix} \langle E_x E_x^* + E_y E_y^* \rangle \\ \langle E_x E_x^* - E_y E_y^* \rangle \\ \langle E_x E_y^* + E_y E_x^* \rangle \\ i\langle E_x E_y^* - E_y E_x^* \rangle \end{pmatrix} \tag{1.3}$$

where E_x and E_y are the components of the electric field in the x- and y-direction, respectively. The symbol $\langle\rangle$ indicates that the quantities are ensemble averages but, assuming stationarity and ergodicity, they can be replaced by time averages with the same result. The first element of the Stokes vector is the total irradiance, the second one is the fraction of light linearly polarised in the horizontal and/or vertical direction, the third element is the fraction linearly polarised at $\pm 45°$ and the the fourth one is the fraction of light circularly polarised with right and/or left handedness.

The Mueller matrix is a 4×4 real matrix of the form:

$$\mathbf{M} = \begin{pmatrix} m_{11} & m_{12} & m_{13} & m_{14} \\ m_{21} & m_{22} & m_{23} & m_{24} \\ m_{31} & m_{32} & m_{33} & m_{34} \\ m_{41} & m_{42} & m_{43} & m_{44} \end{pmatrix} \tag{1.4}$$

that contains all the information concerning the polarisation linear properties of the object that represents. Depending on the polarisation properties of the object, there may be symmetries between elements of the Mueller matrix. However, in the most general case, all the elements of the matrix are different.

An important property of the Mueller matrix representation of polarisation is linearity.[2] That is, the total effect over the polarisation of a light beam due to a series of N optical elements, each one represented by a Mueller matrix $\mathbf{M}_i$, $i = 1, \ldots, N$, is given by

$$\mathbf{M} = \mathbf{M}_N \cdots \mathbf{M}_2 \mathbf{M}_1 \tag{1.5}$$

For instance, non-depolarising objects can be represented by the combination of a linear-diattenuator and a linear-retarder. Therefore, the Mueller matrix of a linear-retarder, with its fast axis oriented in the horizontal direction, followed by a linear-diattenuator is [20]

$$\mathbf{R}(\tau, \Psi, \Delta) = \tau \begin{pmatrix} 1 & -\cos 2\Psi & 0 & 0 \\ -\cos 2\Psi & 1 & 0 & 0 \\ 0 & 0 & \sin 2\Psi \cos \Delta & \sin 2\Psi \sin \Delta \\ 0 & 0 & -\sin 2\Psi \sin \Delta & \sin 2\Psi \cos \Delta \end{pmatrix} \tag{1.6}$$

where τ is the transmittance for unpolarised light, Δ is the retardance and Ψ, defined as

$$\tan \Psi = \sqrt{\frac{\tau_p}{\tau_s}} \tag{1.7}$$

for τ_p and τ_s the transmittance for p and s polarisations, is an auxiliary angle related to the diattenuation of the optical element.[3] The eigenvalues of Mueller matrices of the same form as Eq. (1.6) are important for the calibration of the system developed in this work (see section 4.1). These eigenvalues are [21]

$$\begin{aligned} \lambda_{r_1} &= 2\tau \sin^2(\Psi) \\ \lambda_{r_2} &= 2\tau \cos^2(\Psi) \\ \lambda_{i_1} &= \tau \sin(2\Psi) \exp(i\Delta) \\ \lambda_{i_2} &= \tau \sin(2\Psi) \exp(-i\Delta) \end{aligned} \tag{1.8}$$

from which we can determine τ, Δ and Ψ.

To conclude this section we notice that not every 4×4 real matrix represents a physically realizable object and thus, not every 4×4 real matrix is a Mueller matrix. Conditions for a particular matrix to represent a Mueller matrix can be found in the literature [22–25]. Furthermore, the physical interpretation of the Mueller matrix is not as straightforward

[2] Linearity is not exclusive of the Mueller matrix formalism. It is, in fact, a property of all matrix representations of polarisation.

[3] Δ and Ψ are known as the ellipsometric angles.

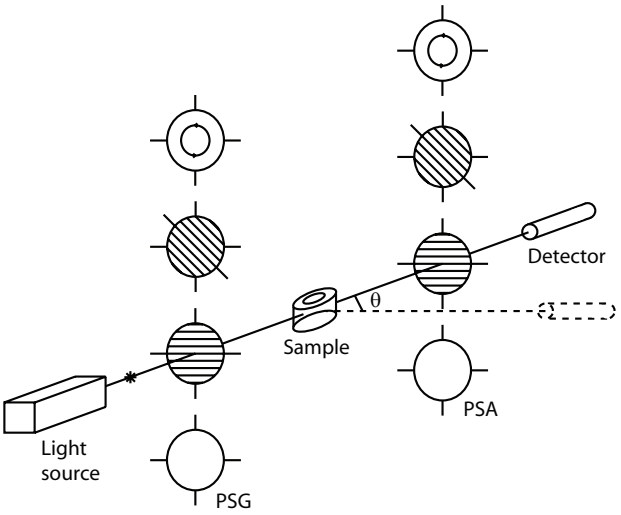

Figure 1.3: Diagram of the basic configuration of a Mueller matrix polarimeter [27].

as the interpretation of the Stokes vector. Nevertheless, a Lu-Chipman decomposition [26], for instance, reveals polarisation properties of the object represented by the matrix, in this case its retardance and diattenuation.

1.2.3 Mueller matrix polarimetry

A typical polarimeter (a device built to do polarimetry) consists of a polarisation state generator (PSG), a place to position the sample, and a polarisation state analyser (PSA). The PSG determines the polarisation state of the incident light whereas the PSA measures the change in this state after interaction with the sample. A Mueller matrix polarimeter is a polarimeter designed and built to measure the 16 elements of the Mueller matrix.

The basic configuration of a Mueller matrix polarimeter requires 4 independent incident polarisation states and 4 independent analysers. Fig. 1.3 is a diagram of this configuration as presented in [27]. The combination of the 4 incident polarisation states with the 4 analysers yields the 16 measurements required to obtain the complete Mueller matrix of a general sample. Fig. 1.4 is a diagram of the combinations polariser-analyser used in the measurement of each element of the Mueller matrix using the polarimeter in Fig. 1.3. Depending on the polarisation properties of a particular sample, and thus in the possible symmetries between

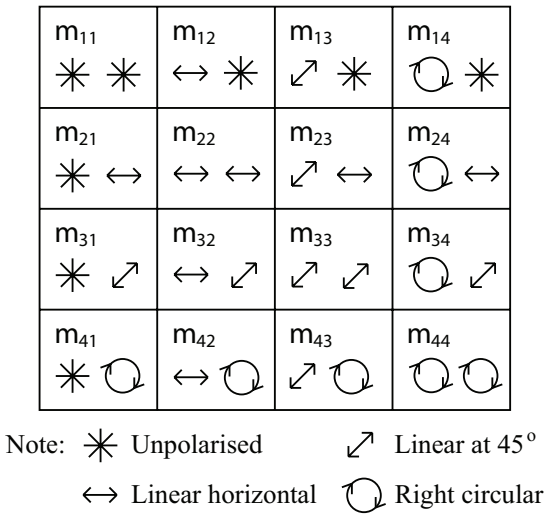

Figure 1.4: Diagram of the combinations polariser-analyser, for the polarimeter in Fig. 1.3, used in the measurement of each element of the Mueller matrix.

its elements, less measurements may be required.

The polarimeter presented above is helpful to understand the functioning of a Mueller matrix poarimeter. Nevertheless, in this configuration, as suggested in Fig. 1.3, the different polarisers and analysers are interchanged between measurements making the system highly sensitive to experimental errors.

Alternative configurations using rotating compensators [28, 29] or variable retardance elements, such as liquid crystal modulators [30], photoelastic modulators [31] and Pockels cells [32, 33], for the PSG and/or the PSA have been reported in the literature. The sensitivity to experimental errors of those polarimeters is lower and performance optimization methods [34], as well as calibration methods [21], have been proposed. The issue of calibration of a polarimeter shall be discussed further in Chap. 4 within the context of the calibration of our system.

1.3 Vectorial polarimetry

Most polarimeters measure the interaction of beam-like fields with the sample. Since light is a vectorial perturbation, in the most general case it has three-dimensional structure; that is, it has a component in each of the three spatial directions. However, this three-dimensional structure is usually ignored even in polarisation microscopes with high NA objectives,

where the three-dimensional nature of the focused EM field is apparent.

To the best of our knowledge, the first attempt to completely characterise a three-dimensional EM field, and that is what we call *vectorial polarimetry*, was done by Ellis and Dogariu [35]. Their method is based on the use of a couple of near-field probes, in nine different configurations, and produced excellent results. Nevertheless, as any near-field technique, it is only suitable for applications where the distance between the sample and the probes can be controlled with sufficiently high precision, making apparent the need for an alternative far-field method.

Richards and Wolf showed [16], using the vectorial theory of diffraction developed by the latter [4], that in the focal region of a high NA aplanatic lens (see Chap. 2), for incident light linearly polarised, there is a longitudinal component comparable to the transversal components, i.e., there is a three-dimensional field distribution. Other incident polarisation states produce a three-dimensional field distribution in the focal region of a high NA lens as well [5, 36]. We propose to use this distribution as a non-mechanical probe to perform *vectorial polarimetry* in the far-field.

In our method, a three-dimensional focused field interacts with the specimen yielding, in the most general case, a three-dimensional scattered field. The resulting scattered field propagates to the detection system where a collector lens collimates it creating a beam-like field with no component along the optical axis; the component along the optical axis is projected over the transversal components by the collector lens (see Fig. 1.5). This projection produces an angle-resolved field distribution. Therefore, by analysing the polarisation state of the scattered light across the exit pupil of the collector lens, using traditional polarimetry techniques, it is possible to retrieve information about the three-components of the field scattered by the specimen and thus, about its interaction with the focused field.

To assess the feasibility of our method, we modelled its performance using a number of numerical tools.[4] The modelling started with the calculation of the field distribution in the focal region of a lens as a function of its NA and the polarisation state of the incident light. This was done using two different methods that shall be discussed in Chap. 2. Then, we modelled the interaction of the focused field with the sample. A number of different methods to describe this interaction are readily available. In this work we chose to start with a point-scatterer and then

[4]We modelled the performance of a vectorial polarimeter in the reflection configuration but this does not mean that only this configuration is possible.

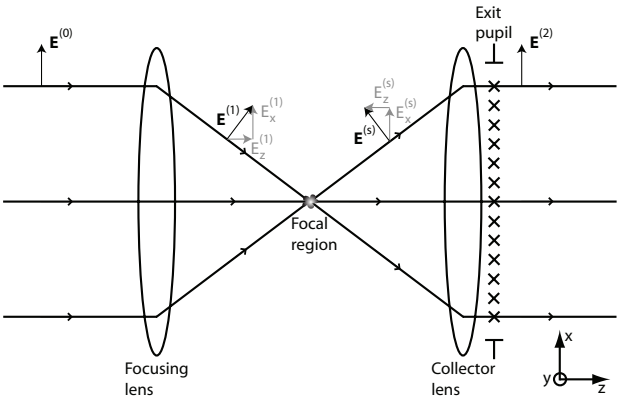

Figure 1.5: Bird's-eye view diagram of the *vectorial polarimetry* method. The longitudinal component of the scattered field, $E_z^{(s)}$, is projected over the transversal components by the collector lens. The crosses indicate sample points on the exit pupil where the polarisation state is analysed.

use the Finite-Difference Time-Domain (FDTD) method, which shall be briefly discussed in §2.3.1, to model more complex samples. Due to the limitations of the FDTD method, it is necessary to perform a near- to far-field transformation over the results obtained for the scattered field; this transformation shall be discussed in §2.4. These three steps constitute the basis of the system's performance modelling.

A fundamental part of this work is the experimental verification of the method. We built a vectorial polarimeter and performed a number of tests to get a proof of concept. The experimental setup, its calibration, and the results obtained shall be presented in Chaps. 3, 4, and 5, respectively. Finally, the conclusions of this work and comments on the future of this research are presented in Chap. 6.

Conferences and publications

The *vectorial polarimetry* method has been presented for discussion with the community in a number of international conferences and workshops. It has also originated a European patent application and a paper describing the method is in preparation.

- David Lara, Oscar Rodríguez and Chris Dainty, "Far-field three-dimensional optical polarimetry", *Workshop on Random Electromagnetic Fields*, Orlando FL, USA, May 2007.

- Oscar Rodríguez, David Lara and Chris Dainty, "Far-field method for the characterization of three-dimensional fields", *Progress in Electromagnetics Research Symposium (PIERS)*, Prague, Czech Republic, August 2007.

- Oscar Rodríguez, David Lara and Chris Dainty, "Far-field method for the characterization of three-dimensional fields", *3rd European Optical Society Topical Meeting on Advanced Imaging Techniques*, Lille, France, September 2007.

- David Lara, Oscar Rodríguez and Chris Dainty, "A vectorial polarimetry method and apparatus for analysing the three-dimensional electromagnetic field resulting from an interaction between a focused illuminating field and a sample to be observed", *European Patent Application No. 07107376.1.*

- Oscar Rodríguez, David Lara and Chris Dainty, "Far-field method for the characterization of three-dimensional fields", *Frontiers in Optics 2008*, Rochester NY, USA, October 2008.

- Oscar Rodríguez, David Lara and Chris Dainty, "Far-field vectorial polarimetry", *Novel Techniques in Microscopy*, Vancouver BC, Canada, April 2009.

- David Lara, Oscar Rodríguez and Chris Dainty, "Far-field three-dimensional optical polarimetry", *Workshop on Partial Electromagnetic Coherence and 3D Polarization*, Koli, Finland, May 2009.

- David Lara, Oscar Rodríguez and Chris Dainty, "Far-field three-dimensional optical polarimetry", *paper in preparation.*

Chapter 2

Numerical analysis

Before embarking on the rather difficult experimental verification of the *vectorial polarimetry* method introduced in this work, we used a number of numerical methods to model its performance and assess its feasibility.

The numerical tools used in this research were developed from scratch based on known techniques and a number of tests were done to verify the accuracy and reliability of our implementation of each technique, as shall be discussed in this chapter.

2.1 Vectorial theory of diffraction

It is known that the scalar theory of diffraction is only applicable when focusing with low NA. Therefore, to describe the EM field distribution in the focal region of a high NA system it is necessary to use a vectorial theory of diffraction.

Different approaches have been made to establish a vectorial theory of diffraction although, currently, the most used is the theory developed by Wolf [4]. In his theory, Wolf described the focused field as the coherent superposition of plane waves, each of which is related to a ray directed from a point in the exit pupil of the high NA system towards its geometrical focus. Wolf associated a weighted electric (or magnetic) field with each of these rays and calculated the total field using the following equations

$$\mathbf{E}(P) = -\frac{ik}{2\pi}\iint_{\Omega}\frac{\mathbf{a}(s_x,s_y)}{s_z}\exp(ik[\Phi(s_x,s_y)+\hat{s}\cdot\mathbf{r}_p])\mathrm{d}s_x\mathrm{d}s_y \qquad (2.1)$$

$$\mathbf{H}(P) = -\frac{ik}{2\pi}\iint_{\Omega}\frac{\mathbf{b}(s_x,s_y)}{s_z}\exp(ik[\Phi(s_x,s_y)+\hat{s}\cdot\mathbf{r}_p])\mathrm{d}s_x\mathrm{d}s_y \qquad (2.2)$$

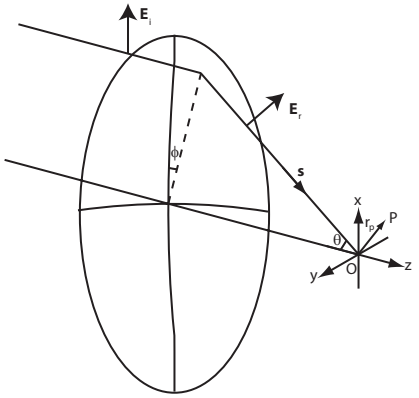

Figure 2.1: Diagram of the light focused by a high NA system [37]. The origin of the coordinate system is in the geometrical focus of the lens.

where k is the wave number, $\hat{s}$ is a unitary vector in the direction of the ray, $\Phi(s_x, s_y)$ is the aberration function, i.e. the deviation of the actual wavefront from a sphere centered in the geometrical focus, $\mathbf{a}(s_x, s_y)$ and $\mathbf{b}(s_x, s_y)$ are the so-called *strength vectors* or *strength factors*, i.e. the weighted fields, Ω is the solid angle subtended by the exit pupil as seen from the geometrical focus and $\mathbf{r}_p$ is the vector from the origin to the observation point P (see Fig. 2.1).[1] The integrals shown in Eqs. (2.1) and (2.2) are usually referred to as the Debye-Wolf integrals due to the resemblance that they bear with Debye's integrals for scalar diffraction. Using Debye-Wolf integrals, Richards and Wolf [16] calculated the field distribution in the focal plane of an aplanatic system as a function of its NA for incident light linearly polarised. An aplanatic system is a system that obeys Abbe's sine condition. Thus, in the context of Richards and Wolf work, an aplanatic system is a system for which any ray entering the system parallel to the optical axis at a height h, crosses a sphere with radius f, where f is its focal length, at a height h in the image space. Fig. 2.2 is a diagram of a system satisfying this condition. Richards and Wolf found that, for an aplanatic system, the electric field components can be written as follows

$$\begin{aligned} e_{2x} &= -iK[I_0 + I_2 \cos 2\phi_p] \\ e_{2y} &= -iK I_2 \sin 2\phi_p \\ e_{2z} &= -2K I_1 \cos \phi_p \end{aligned} \tag{2.3}$$

[1]The geometrical focus is the gaussian focus obtained by tracing rays in an aberration-free lens.

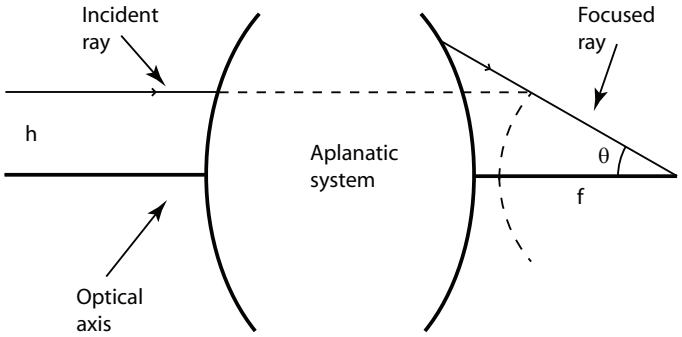

Figure 2.2: Diagram of the aplanatic system studied by Richards and Wolf [16].

with the functions I_n given by

$$\begin{aligned} I_0 &= \int_0^\alpha (\cos\theta)^{1/2} \sin\theta(1+\cos\theta) J_0(kr_p \sin\theta \sin\theta_p) \\ &\quad \times \exp[ikr_p \cos\theta \cos\theta_p] \mathrm{d}\theta \\ I_1 &= \int_0^\alpha (\cos\theta)^{1/2} (\sin\theta)^2 J_1(kr_p \sin\theta \sin\theta_p) \\ &\quad \times \exp[ikr_p \cos\theta \cos\theta_p] \mathrm{d}\theta \\ I_2 &= \int_0^\alpha (\cos\theta)^{1/2} \sin\theta(1-\cos\theta) J_2(kr_p \sin\theta \sin\theta_p) \\ &\quad \times \exp[ikr_p \cos\theta \cos\theta_p] \mathrm{d}\theta \end{aligned} \tag{2.4}$$

where $0 \leq \theta, \theta_p < \pi$ and $0 \leq \phi_p < 2\pi$ are the spherical and azimuthal angles, respectively, α is the angular semi-aperture of the exit pupil, and K is a constant factor that depends on the wavelength, the focal length of the system, and the refractive index of the surrounding medium. Equivalent relations can be readily found for the magnetic field.

An important result of Richards and Wolf work is that the irradiance distribution in the focal plane starts to differ from the Airy pattern predicted by the scalar theory as the NA is increased, and is highly asymmetric for high NA. In fact, their results showed that the principal maximum elongates beyond the theoretical Airy disc radius in the direction of the incident polarisation and shortens below this radius in the orthogonal direction. Fig. 2.3 shows the result presented by Richards and Wolf for the limiting case NA$\rightarrow$1 in air.[2]

[2]If the optical system is immersed in a medium with higher refractive index, the limiting NA is increased but the corresponding maximum angular semi-aperture is

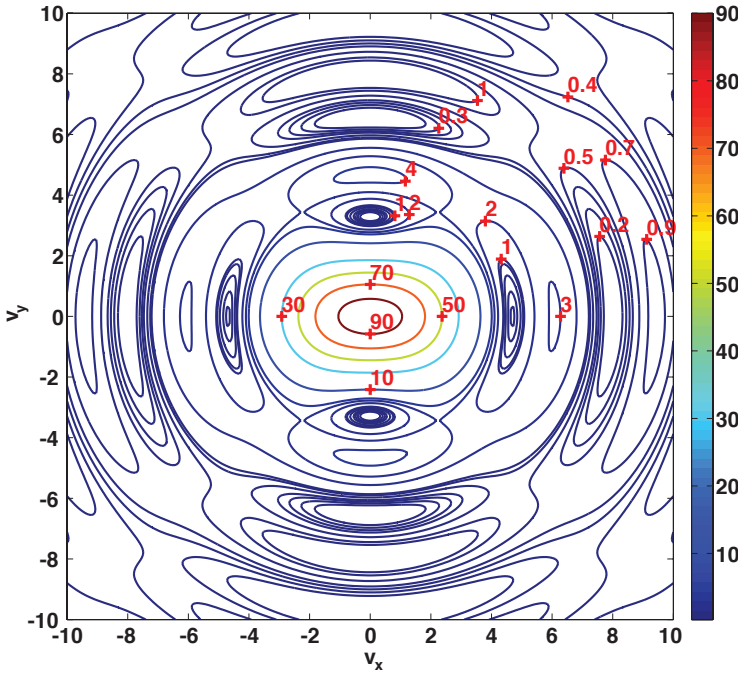

Figure 2.3: Irradiance in the focal plane of a NA→1 (in air) lens for incident light linearly polarised in the x-direction. The irradiance is normalized to be 100 in the geometrical focus and the units in the axes are optical units.

An extension of Richards and Wolf work, to consider focusing through a planar interface between two media of mismatched refractive indices, was given by Török *et al.* in [37]. This case is useful, for instance, in microscopy and optical data storage, where an intermediate medium has an effect over the focused light. The generalization given by Török *et al.* introduces the so-called *generalized Jones matrices* to compute the *strength factor* of each ray. The *generalized Jones matrices* are 3×3 matrices that account for the geometrical transformations suffered by the electric (or magnetic) field of a typical ray as it passes through the optical system.

Following the formalism introduced in [37], and assuming that the electric field remains on the same side and at constant angle with respect to a meridional plane, the *strength factor* of a typical ray is found to be

$$\mathbf{E}^{(2)}_{(x,y,z)} = \mathbf{R}^{-1}[\mathbf{P}^{(2)}]^{-1}\mathbf{I}A(\theta_1)\mathbf{P}^{(1)}\mathbf{L}\mathbf{R}\mathbf{E}^{(0)}_{(x,y,z)} \tag{2.5}$$

where $\mathbf{R}$, $\mathbf{L}$, $\mathbf{P}^{(1)}$, $\mathbf{P}^{(2)}$ and $\mathbf{I}$ are the *generalized Jones matrices* described below, $\mathbf{E}^{(0)}_{(x,y,z)}$ and $\mathbf{E}^{(2)}_{(x,y,z)}$ are the incident and focused field in the second medium, respectively, and $A(\theta_1)$ is an apodization function that accounts for energy conservation in an aplanatic system (see Fig. 2.4).[3]

The *generalized Jones matrices* describe the geometrical transformations suffered by the incident field during its pass through the lens. This transformations can be explained as follows: $\mathbf{R}$ is a rotation around the z-axis, by an angle ϕ_1, to make the incident field parallel to the meridional plane that contains the optical axis and the incident ray, $\mathbf{L}$ is a rotation around the direction orthogonal to the meridional plane, by an angle θ_1, to make the incident field orthogonal to the ray that goes from a point in the pupil to the geometrical focus, $\mathbf{P}^{(1)}$ is a coordinate system transformation to obtain the field components in terms of components parallel and orthogonal to the plane of incidence in the interface between the two mismatched media, $\mathbf{I}$ is a matrix with the Fresnel transmission coefficients for the aforementioned components, $[\mathbf{P}^{(2)}]^{-1}$ is the inverse coordinate system transformation that yields the transmitted field components in the coordinate system defined by the meridional plane and its orthogonal, and $[\mathbf{R}]^{-1}$ is the inverse rotation around the z-axis, by an angle $-\phi_1$, to obtain the focused field components in the global XYZ coordinate system.

---

the same, namely, $\alpha = \pi/2$. In this case, the value of K in Eqs. (2.3) is modified since it depends on the refractive index of the immersion medium.

[3] Richards and Wolf proved in [16] that the apodization function for an aplanatic system is $A(\theta) = \sqrt{\cos\theta}$.

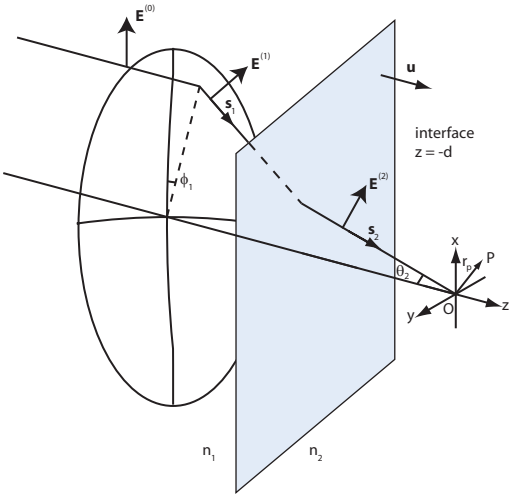

Figure 2.4: Diagram of the light focused through a planar interface between two media of mismatched refractive indices [37].

With the *strength factor* given in Eq. (2.5), Török *et al.* calculated the electric (and magnetic) field distribution in the focal region of the system shown in Fig. 2.4, for incident light linearly polarised, by setting the appropriate boundary conditions over the fields given by Debye-Wolf integrals (Eqs. (2.1) and (2.2)) at the interface between the two media. The result of their calculations can be written in the same way shown in Eq. (2.3) but with the constant factor K depending also on the refractive index of medium 1, n_1, and integrals I_n given by

$$
\begin{aligned}
I_0 = &\int_0^{\alpha} (\cos\theta_1)^{1/2} (\sin\theta_1) \exp[ik_0\Psi(\theta_1,\theta_2,-d)] \\
&\times (\tau_s + \tau_p \cos\theta_2) J_0\left(\frac{v\sin\theta_1}{\sin\alpha}\right) \\
&\times \exp\left(\frac{iu\cos\theta_2}{\sin^2\alpha}\right) \mathrm{d}\theta_1 \\
I_1 = &\int_0^{\alpha} (\cos\theta_1)^{1/2} (\sin\theta_1) \exp[ik_0\Psi(\theta_1,\theta_2,-d)] \\
&\times \tau_p (\sin\theta_2) J_1\left(\frac{v\sin\theta_1}{\sin\alpha}\right) \exp\left(\frac{iu\cos\theta_2}{\sin^2\alpha}\right) \mathrm{d}\theta_1 \\
I_2 = &\int_0^{\alpha} (\cos\theta_1)^{1/2} (\sin\theta_1) \exp[ik_0\Psi(\theta_1,\theta_2,-d)] \\
&\times (\tau_s - \tau_p \cos\theta_2) J_2\left(\frac{v\sin\theta_1}{\sin\alpha}\right)
\end{aligned}
$$

$$\times \exp\left(\frac{iu\cos\theta_2}{\sin^2\alpha}\right) \mathrm{d}\theta_1 \tag{2.6}$$

where v and u are the optical units defined as

$$\begin{aligned} v &= k_1 r_p \sin\theta_p \sin\alpha \\ u &= k_2 r_p \cos\theta_p \sin^2\alpha \end{aligned} \tag{2.7}$$

for k_1 and k_2 the wave numbers in media 1 and 2, respectively, τ_p and τ_s are the Fresnel transmission coefficients for the p and s polarisation components, respectively, at the interface between media 1 and 2, θ_1 and θ_2 are the spherical angles in media 1 and 2, respectively, α is the semi-aperture of the exit pupil in medium 1 and $\Psi(\theta_1, \theta_2, -d)$ is a spherical aberration function due to the interface.

The introduction of spherical aberration in the definition of the I_n's is the main difference between the results given by Richards and Wolf and those by Török *et al.* It is worth noticing that, as pointed out by Török *et al.*, Eqs. (2.6) reduce to Eqs. (2.4) when the special case $n_1 = n_2$ is considered, as should be expected. The numerical results obtained by Török *et al.*, based on their generalization of Debye-Wolf integrals, are shown in [38].

Another interesting example of the application of the vectorial theory of diffraction is the focusing of circularly polarised light. In that case, the electric field components in the focal region are

$$\begin{aligned} e_{2x} &= \frac{K}{\sqrt{2}}[I_0 + I_2 \exp(\mp 2i\phi_p)] \\ e_{2y} &= \frac{\mp iK}{\sqrt{2}}[I_0 - I_2 \exp(\mp 2i\phi_p)] \\ e_{2z} &= \frac{-2iK}{\sqrt{2}} I_1 \exp(\mp i\phi_p) \end{aligned} \tag{2.8}$$

where the $\mp$ sign indicates the handedness: - for right and + for left circular polarisation. The integrals I_n are the same as in the case of linear polarisation.

Note that, because of the form of the electric field components in the focal region given by Eqs. (2.3), for linear polarisation, and Eqs. (2.8), for circular polarisation, the state of polarisation in the geometrical focus is that of the incident light. This is to be expected since all the other components of the rays reaching the focal region at an angle different from zero interfere destructively in the focal point. From the mathematical point of view, the Bessel functions of the first kind and order n, $J_n(\xi)$,

are identically zero at $\xi = 0$ for all $n \neq 0$ ($J_0(0) = 1$). Thus, the only I_n different from zero at the focus is I_0, which corresponds to the incident polarisation state.

2.2 Evaluation of the diffraction integrals

In the previous section, it was briefly discussed how to calculate the electric field in the focal region of a high NA system. However, the expressions for the field components are given in terms of the integrals I_n for which no analytical solutions are known. To overcome this problem, it is possible to perform the numerical integration of these three functions. Nevertheless, it is necessary to be very careful with these integrations due to the rapid variation of the exponential term in the integrals, which can produce considerable numerical errors in the evaluation of the functions.

To simplify the evaluation of these integrals, Török *et al.* developed in [39] an analytical way to transform the highly unstable integrals I_n into more stable functions. The transformation proposed in [39] reduces the integrals to a set of infinite series that can be accurately evaluated with a relatively small number of terms due to its rapid convergence. The transformation proposed by Török *et al.* changes the integrals to the following functions

$$\begin{aligned} I_0 &= 2\frac{n_2}{n_1}\sum_{s=0}^{\infty} a_s^{(0)} i^s C_s^{(1/2)}(\cos\psi) j_s(\omega) \\ I_1 &= 2\frac{n_2}{n_1}(\sin\psi)\sum_{s=0}^{\infty} a_s^{(1)} i^s C_s^{(3/2)}(\cos\psi) j_{s+1}(\omega) \\ I_2 &= 2\frac{n_2}{n_1}(\sin^2\psi)\sum_{s=0}^{\infty} a_s^{(2)} i^s C_s^{(5/2)}(\cos\psi) j_{s+2}(\omega) \end{aligned} \tag{2.9}$$

where, for $n = 0 \ldots 2$, $C_s^{(n+1/2)}$ is the Gegenbauer polynomial of the first kind and order $n + 1/2$, j_{s+n} is the spherical Bessel function of the first kind and order $s + n$, ω and ψ are generalized optical units, and the expansion coefficients are given by

$$\begin{aligned} a_s^{(0)} &= N_s^{(0)} \int_0^{\beta} \frac{\cos\theta_2}{\sqrt{\cos\theta_1}}(\sin\theta_1)(\tau_s + \tau_p\cos\theta_2) \\ &\quad \times \exp[ik_0\Psi(\cos\theta_2)] C_s^{(1/2)}(\cos\theta_2)\mathrm{d}\theta_2 \\ a_s^{(1)} &= N_s^{(1)} \int_0^{\beta} \frac{\cos\theta_2}{\sqrt{\cos\theta_1}}(\sin\theta_1)\tau_p \exp[ik_0\Psi(\cos\theta_2)] \end{aligned}$$

$$\times \quad C_s^{(3/2)}(\cos\theta_2)(\sin^2\theta_2)\mathrm{d}\theta_2$$

$$a_s^{(2)} = N_s^{(2)} \int_0^{\beta} \frac{\cos\theta_2}{\sqrt{\cos\theta_1}}(\sin\theta_1)(\tau_s - \tau_p\cos\theta_2)$$

$$\times \quad \exp[ik_0\Psi(\cos\theta_2)]C_s^{(5/2)}(\cos\theta_2)\sin^2\theta_2\mathrm{d}\theta_2 \qquad (2.10)$$

with $N_s^{(n)}$ a normalization factor. These expressions are, at least in principle, more stable than those given by Eqs. (2.6) and thus, easier to evaluate.[4] Alternatively, the evaluation of the Debye-Wolf diffraction integrals can be done using the eigenfunctions expansion introduced by Sherif and Török [40] and by Sherif *et al.* [41].

Although the expressions given in Eqs. (2.9) and (2.10) can be implemented in a computer programme (in fact, during the development of this research this approximation was used before any other) it is also possible to evaluate the integrals I_n using the approximations shown in [42]. In this work, Wilson *et al.* showed that the form and relative magnitude of the integrals do not depend strongly on the value of the aperture and thus, they can be approximated by their values for small apertures. Using this approximation, the integrals reduce to

$$I_0(v,\alpha) \approx 2\alpha^2\frac{J_1(v)}{v}$$

$$I_1(v,\alpha) \approx \alpha^3\frac{J_2(v)}{v}$$

$$I_2(v,\alpha) \approx \frac{\alpha^4}{2}\frac{J_3(v)}{v} \qquad (2.11)$$

with v given by Eq. (2.7), which can be easily evaluated.

2.3 Calculation of the scattered field

There are many different approaches to perform scattering calculations. Some of them are analytical (T-matrix, Mie scattering, etc.) and some others numerical (Discrete Dipole Approximation, Finite Element, etc.) but most of them are only applicable in particular cases. In this work, we chose to use the Finite-Difference Time-Domain (FDTD) method [43, 44] due to its relative ease of implementation in a computer programme and its reliability proved in a number of applications [45–47].

[4] The form of the spherical aberration function, $\Psi(\cos\theta_2)$, obtained by Török *et al.* in [39], may introduce further instabilities in the calculations. However, a suitable way to avoid these instabilities was presented by Török *et al.* in the same paper.

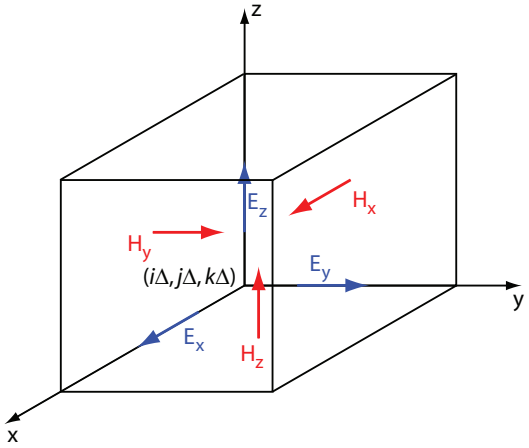

Figure 2.5: Yee's cubic *unit-cell* at location $(i\Delta, j\Delta, k\Delta)$ for i, j, k positive integers and Δ the cell's side length. The electric and magnetic field components are located in their actual position within the *unit-cell*.

2.3.1 FDTD method

The FDTD method is a numerical method for the solution of Maxwell's coupled curl equations introduced by Yee [48].[5] A comprehensive discussion of the method is beyond the scope of this thesis and only the main ideas shall be discussed here.

In the FDTD method, the region of space to be modelled is divided in so-called *unit-cells*. Each *unit-cell* has associated three components of the electric field and three components of the magnetic field. Fig. 2.5 is a schematic diagram of Yee's cubic *unit-cell* with the electric and magnetic fields positioned accordingly. To solve the Ampère-Maxwell equation for the electric field in the whole modelled space at a time $(n + 1/2)\Delta t$, with n a positive integer and Δt the duration of the *time-step*, the space derivatives of the magnetic field components are approximated by finite differences between their value in adjacent *unit-cells* at time $n\Delta t$. Then, the time derivative of the electric field is approximated by a finite difference between values of the field separated one *time-step*, and the electric field at time $(n+1/2)\Delta t$ is obtained as function of the electric field at time $(n-1/2)\Delta t$ and the magnetic field components at time $n\Delta t$. For instance, in the notation of the FDTD method, the x component of

[5] Although the FDTD method itself does not solve explicitly the divergence equations, it can be proved that the fields obtained with this method satisfy them. A proof of this statement can be found in [43].

the electric field at time $(n+1/2)\Delta t$ is written as

$$\begin{aligned} E_x|^{n+1/2}_{i+1/2,j,k} = & C_{a,E_x}|_{i+1/2,j,k} E_x|^{n-1/2}_{i+1/2,j,k} \\ & + C_{b,E_x}|_{i+1/2,j,k} [H_z|^n_{i+1/2,j+1/2,k} - H_z|^n_{i+1/2,j-1/2,k} - \dots \\ & - H_y|^n_{i+1/2,j,k+1/2} + H_y|^n_{i+1/2,j,k-1/2} - J_{source_x}|^n_{i+1/2,j,k} \Delta] \end{aligned} \tag{2.12}$$

where the subscripts indicate the *unit-cell* where the field is being evaluated, with its corresponding spatial offset, and the superscripts the *time-step* at which the field is taken. In Eq. (2.12) $C_{a,E_x}|_{i+1/2,j,k}$ and $C_{b,E_x}|_{i+1/2,j,k}$ are factors that depend on the cell's side length, the duration of the *time-step* and the physical properties of the space at the location of the *unit-cell*. $J_{source_x}|^n_{i+1/2,j,k}$ is a current density associated to external sources. Similar relations can be written for the y and z components of the electric field.

Once the electric field has been computed across the modelled space, the magnetic field is updated, half a *time-step* later, using the values of the electric field calculated as described above. Thus, the FDTD expression for the y component of the magnetic field, as given by Faraday's law, is written as

$$\begin{aligned} H_y|^{n+1}_{i+1/2,j,k+1/2} = & D_{a,H_y}|_{i+1/2,j,k+1/2} H_y|^n_{i+1/2,j,k+1/2} \\ & - D_{b,H_y}|_{i+1/2,j,k+1/2} [E_z|^{n+1/2}_{i,j,k+1/2} - E_z|^{n+1/2}_{i+1,j,k+1/2} - \dots \\ & - E_x|^{n+1/2}_{i+1/2,j,k} + E_x|^{n+1/2}_{i+1/2,j,k+1} - M_{source_y}|^{n+1/2}_{i+1/2,j,k+1/2} \Delta] \end{aligned} \tag{2.13}$$

where $D_{a,H_y}|_{i+1/2,j,k+1/2}$ and $D_{b,H_y}|_{i+1/2,j,k+1/2}$ are factors that depend on the parameters of the FDTD method (Δ and Δt) and $M_{source_y}|^{n+1/2}_{i+1/2,j,k+1/2}$ is a "magnetic current" introduced to represent external sources of magnetic field. Again, similar expressions can be written for the x and z components.

The temporal staircasing nature of the method allows for the solution of the coupled equations without solving a system of simultaneous equations. By repeating this process a sufficiently large number of *time-steps*, we can compute the stationary solution for the scattered field.

A fundamental part of the FDTD method is the modelling of the incident field. Several approaches to model this field have been proposed in the past years; the *point source* condition, the *total-field/scattered-field* formulation and the *scattered-field* formulation are three of the most commonly used. In this work we used the *scattered-field* formulation because it allows us to easily introduce fields with non-planar wavefronts,

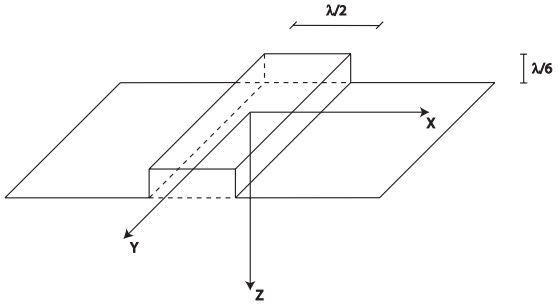

Figure 2.6: Sub-resolution rail-shaped scatterer made of a PEC.

as is the case in our tightly focused incident field. The *scattered-field* formulation stems from the fact that the total field in the surface and interior of the scatterer must satisfy the boundary conditions for the EM field. For instance, for the scatterers modelled in this work —i.e., scatterers made of a perfect electric conductor (PEC)— the boundary conditions can be written as

$$\mathbf{E}_s^t = \begin{cases} -\mathbf{E}_i^t & \text{at the interface} \\ 0 & \text{inside} \end{cases} \tag{2.14}$$

where $\mathbf{E}_s^t$ and $\mathbf{E}_i^t$ are the components of the scattered and incident electric field, respectively, tangential to the surface of the scatterer. Thus, with prior knowledge of the incident field, we can set the initial conditions within the FDTD space using Eq. (2.14) and start the *time-stepping* process for the solution of Maxwell's curl equations.

In its most simple formulation, as originally introduce by Yee and used in this work, the space modelled is divided in cubic *unit-cells*. This formulation simplifies the expressions for the calculation of the EM field components but limits the shape of the scatterers that can be accurately modelled.[6] The cubic *unit-cell* is suitable for the scatterers modelled in this work, namely: the sub-resolution rail-shaped scatterer in Fig. 2.6, the square-shaped scatterer in Fig. 2.7, and the cross-shaped scatterer in Fig. 2.8.

Another important aspect of the *unit-cell* is its size. To reduce numerical dispersion (i.e. the change in the propagation velocity as a function of the direction of propagation within the FDTD modelled space) and achieve accurate results, the *unit-cell* must have a side length much smaller than the smallest wavelength considered to interact with the

[6]For instance, modelling scatterers with round edges may produce large numerical errors.

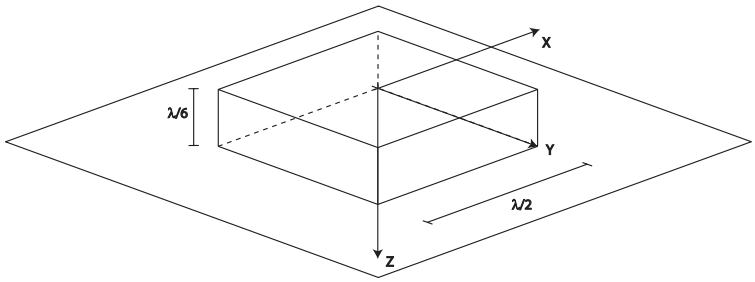

Figure 2.7: Sub-resolution square-shaped scatterer made of a PEC.

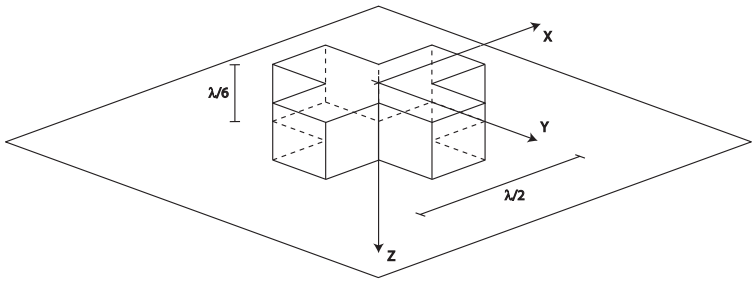

Figure 2.8: Sub-resolution cross-shaped scatterer made of a PEC.

scatterer.[7] The actual side length of the *unit-cell*, compared to the wavelength, depends on the particular application and numerical experiments have to be done to assess the effects of numerical dispersion. In our implementation of the FDTD method, we chose a side length $\Delta = \lambda/30$ which, according to our numerical experiments, reduces sufficiently the numerical dispersion.

The length of the *time-step* is also important in the FDTD method. Large *time-steps* generate numerical instability that yields noisy, inaccurate results. In fact, the shortest the *time-step*, the highest the stability and accuracy of the results. However, if a very small *time-step* is chosen, a larger number of *time-steps* is required to reach the stationary state, increasing the computation time. The upper limit for the duration of the *time-step*, that guaranties the numerical stability of the FDTD method, is given by the Courant factor. For a three-dimensional cubic *unit-cell* space, the Courant factor limits the length of the *time-step* to the following range

$$\Delta t \leq \frac{\Delta}{c\sqrt{3}} \tag{2.15}$$

[7] In our case, we modelled monochromatic incident light with $\lambda = 532\text{nm}$ but the FDTD method itself allows for the modelling of broadband sources.

where c is the speed of light *in vacuo*.

In many applications it is necessary to model the propagation of the scattered field in free space. However, if the simulations need to be run for a long time, the computed fields reach the outer boundaries of the modelled space and spurious, i.e. non-physical, reflections occur. The spurious reflections propagate back into the computational space corrupting the calculated fields. The effect of these reflections can be reduced to a minimum using absorbing boundary conditions (ABCs). The ABCs permit the absorption of the scattered field in the outer regions of the modelled space and, in this way, reduce the spurious reflections. The optimization of the ABCs is, perhaps, one of the most important parts of its implementation. Nevertheless, no standard method for this is available making it very tricky.

2.4 Near- to far-field transformation

Although the FDTD method is useful for the calculation of the scattered-field, the size of the space region that can be modelled is limited by the computer resources available, particularly by the memory. Therefore, usually it is only possible to model small regions of space around the scatterer.[8] In many applications, the far-scattered field is required, as it is in our case, and a near- to far-field (NTFF) transformation must be performed.

Török *et al.* [49] introduced a method for the calculation of the far-field from the near-field using a modified version of the Stratton-Chu integrals for diffraction [50]. In their method, as in any NTFF transformation, the far-field at any point in the space outside a volume containing all the sources and sinks of EM field can be calculated from the value of the EM field over a surface enclosing the volume. The advantage of Török *et al.* method over similar methods is that the far-field EM components are given in terms of the cartesian components of the near-field, which simplifies its application to FDTD results.

Based on Török *et al.* method, we developed a programme to perform the NTFF transformation of our FDTD results. This programme calculates the far-field over a surface at an arbitrary distance form the scatterer. For instance, it can be used to calculate the far-field over a plane parallel to the XY plane at a distance z_p from the scatterer.[9] To

[8] By small we mean regions with dimensions comparable to the wavelength.

[9] The size of the plane and the distance form the scatterer are parameters that can be modified in the programme.

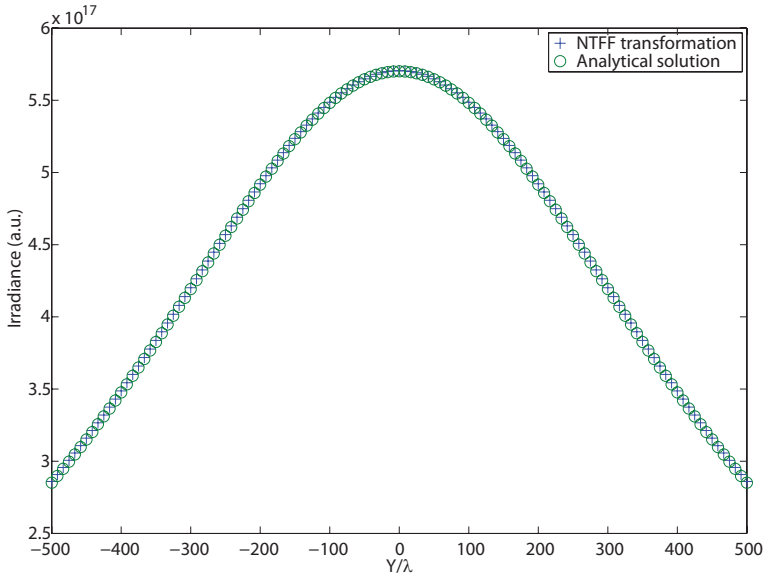

Figure 2.9: Comparison between the analytical solution and the NTFF transformation for the electric field irradiance radiated by an electric dipole with dipole moment oriented along the x-axis. The observation plane is a square with side $a = 1000\lambda$ at a distance $z_p = 500\lambda$ from the dipole.

test our NTFF programme, we used the analytical solution of the field radiated by a dipole to calculate the field components over the surface of a small parallelogram (with sides comparable to the wavelength) enclosing the dipole. These results were used to feed the NTFF transformation programme. Then, we calculated the far-field radiated by the dipole, with the analytical solution, and compared it with the field obtained with the NTFF transformation programme over a square plane of side $a = 1000\lambda$ at a distance $z_p = 500\lambda$ from the scatterer. The comparison between the electric field irradiance distribution obtained using the analytical solution and the NTFF transformation along the y-axis is shown in Fig. 2.9 for a dipole with dipole moment in the x-direction. The relative error, defined by Török *et al.* as

$$\epsilon = \frac{\sum_{i=1}^{N} |\mathbf{E}^{sc}(\mathbf{r}_i) - \mathbf{E}^{An}(\mathbf{r}_i)|^2}{\sum_{i=1}^{N} |\mathbf{E}^{An}(\mathbf{r}_i)|^2}, \tag{2.16}$$

was calculated and a maximum value $\epsilon = 1.3181 \times 10^{-6}$, which is small enough for our application, was obtained. A close look at Fig. (2.9) shows that the error between the analytical solution and the NTFF transformation is larger at the edges of the plot, even if it is hard to notice it due to the scale, indicating that the numerical errors are smaller at the center of the observation plane.

2.5 McCutchen's method

The vectorial theory of diffraction introduced by Wolf has been proved suitable for the calculation of the EM field distribution in the focal region of a high NA lens. However, the definition of the *strength factor*, apart from a few well known cases such as linear, circular, azimuthal and radial polarisation, can be difficult. This is particularly difficult for non-homogeneous incident polarisation states.[10] Thus, it is appropriate to look for alternatives to simplify the calculation of the focused field for non-homogeneous incident polarisations. McCutchen's method [51, 52] is a good alternative to Wolf's vectorial theory of diffraction in these cases.

McCutchen's method states that the field in the focal region of a lens can be calculated as the three-dimensional Fourier transform of the so-called *generalized aperture*. The *generalized aperture* is the projection of the exit pupil over the surface of a sphere limited by the solid angle subtended by the exit pupil as seen from the geometrical focus, i.e., the angular semi-aperture of the *generalized aperture* is limited by the maximum angle permitted by the NA.

The calculation of the *generalized aperture* in McCutchen's method is equivalent to the calculation of the *strength factor* in the vectorial theory of diffraction. Thus, during the projection of the pupil over the spherical surface, the different components of the incident field are combined giving the contribution of each ray to the different components of the focused field. Each component is calculated independently of the others, which implies three Fourier transforms but, since the method can be implemented in a computer programme using an FFT algorithm, the calculations are considerably faster than direct integration of Debye-Wolf integrals.

For the implementation of McCutchen's method in a computer programme it is necessary to do a sampling of the *generalized aperture*. Note

[10] A non-homogeneous incident polarisation state is that where the polarisation varies across the aperture of the beam.

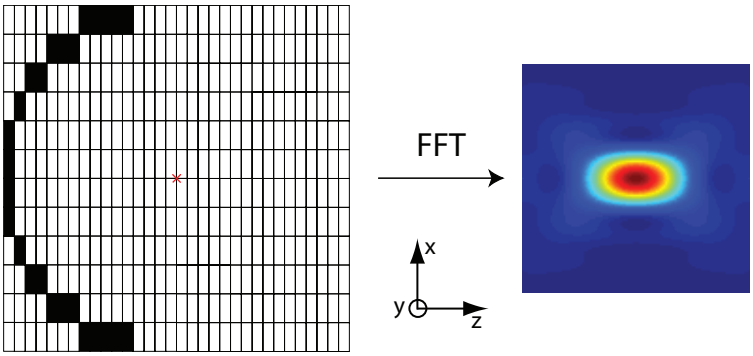

Figure 2.10: Representation of the implementation of McCutchen's method in a computer programme. An FFT algorithm is applied to the sampling of the *generalized aperture* to obtain the field distribution in the focal region of the lens. The sampling is finer in the z-direction to obtain the same number of sampling pixels over the *generalized aperture* in the three spatial directions.

that the sampling is done in three-dimensions since the *generalized aperture* is a surface embedded in a three-dimensional space. In our case, the sampling was done according to the Whittaker-Shannon sampling theorem [53] (Fig. 2.10) for a pixel size of $\lambda/30$ in the focal region. This pixel size is the same used for the evaluation of Debye-Wolf integrals and is consistent with the *unit-cell* side length of our FDTD programme.

Since Debye-Wolf integrals have become a standard for the calculation of high NA focused fields, we tested our implementation of McCutchen's method by comparing the results obtained with both methods for incident light linearly polarised in the x-direction. Fig. 2.11 shows this comparison as a profile along the x-direction in the focal plane of a NA=0.95 aplanatic lens at $\lambda = 532$nm.

Although the profiles agree quite well, a close look at the results reveals slight differences between the two methods. The main reason for the differences is the numerical errors due to the sampling of the *generalized aperture*. A finer sampling yields results more similar to Debye-Wolf integrals but the demand for computer resources increases enormously.

The definition of non-homogeneous incident polarisation states in McCutchen's method is relatively easy, compared to Debye-Wolf integrals, since the polarisation state over the sampling of the *generalized aperture* can be described pixel-wise and then the application of an FFT algorithm is straightforward. This characteristic can be used to tailor the field distribution in the focal region by engineering the incident polari-

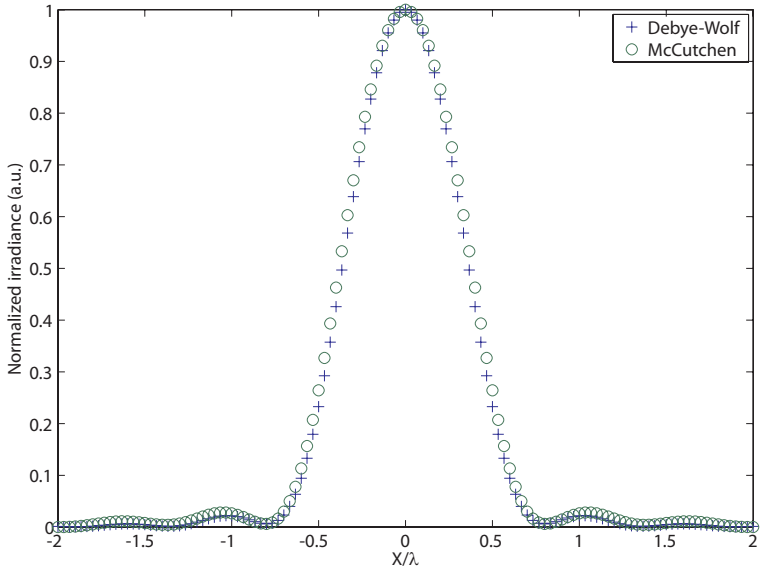

Figure 2.11: Comparison between McCutchen's method and Debye-Wolf integrals for incident light linearly polarised. The profile and incident polarisation are taken along the x-direction.

sation [36]. The ability to tailor the EM field distribution in the focal region of a high NA focusing system plays a key role in our method since it can be used to improve its sensitivity by choosing the field distribution that produces the largest effect over the polarisation pattern in the exit pupil of the collector lens for a particular kind of specimens.

Another appealing characteristic of McCutchen's method is the direct connection that can be established between the sampling of the *generalized aperture* and the aperture of a pixel-wise spatial light modulator. This connection has been investigated by Iglesias and Vohnsen [36] in the context of using a tandem of pixel-wise spatial light modulators to mimic continuous polarisation states. An example of this is the similar EM field distributions obtained in the focal region of a high NA lens for radial and pseudo-radial incident polarisations. Fig. 2.12 is a schematic diagram of both polarisation states.

The largest component of the focused field for incident radial polarisation is the z component. The spot produced by this component is smaller than the corresponding Airy disc and it has been proposed as a way to increase the resolution of optical scanning microscopes (see §1.1). Fig. 2.13 is a comparison between profiles of the z component's normalized modulus squared along the x-direction of the focal plane for

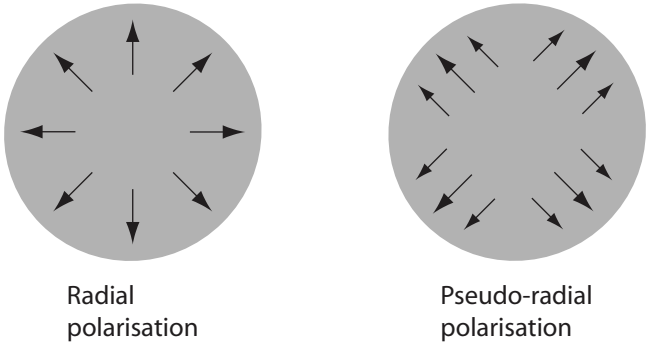

Figure 2.12: Radial and pseudo-radial polarisation.

incident radial and pseudo-radial polarisation. This figure shows that the two profiles are different in the secondary maxima but have the same central lobe. Since most of the energy is localized in the central lobe, and is this lobe what gives the resolution of imaging systems with radial illumination, it is apparent that, to a large extent, the use of pseudo-radial polarisation yields similar results as pure radial polarisation.

2.6 Performance of the method

The preceding sections introduced the basic ideas of the tools used to model the performance of the *vectorial polarimetry* method. In this section we shall present examples of the polarisation patterns in the exit pupil of the collector lens as obtained with the tools developed in this research.

2.6.1 Point-scatterer

It is a common practice in the modelling of the performance of optical microscopes to analyse as a first specimen a point-scatterer. Such specimen is usually modelled as a point-dipole with dipole moment, $\mathbf{p}$, proportional to the incident field. This assumption is valid as long as the point-scatterer is much smaller than the wavelength of the illumination [54]. Under these circumstances, the scattered field can be obtained using the analytical solution for the radiation of a dipole which, in the far-field region, is given by [54]

$$\mathbf{E}^{(s)}_{(x,y,z)} = -\frac{1}{4\pi\epsilon_0}\left\{\frac{k^2 e^{ikr}}{r}\mathbf{r}\times(\mathbf{r}\times\mathbf{p})\right\} \tag{2.17}$$

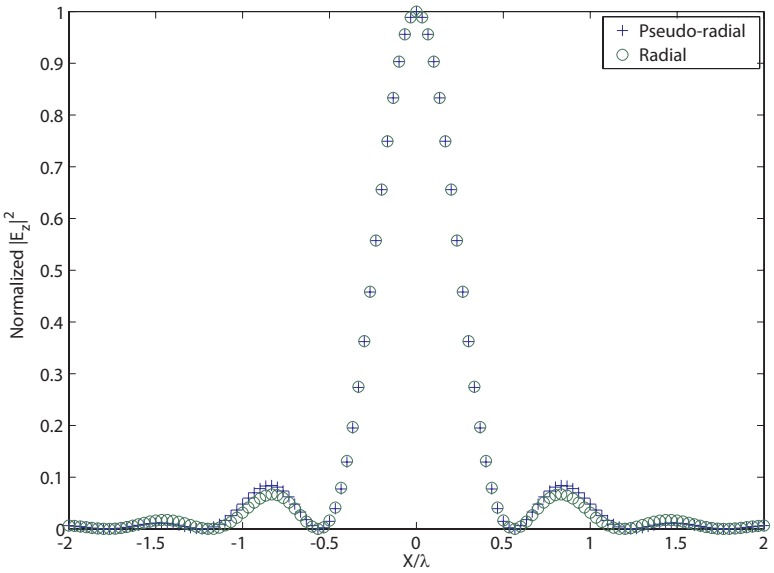

Figure 2.13: Comparison between profiles of the z component's normalized modulus squared in the focal plane along the x-direction for incident radial and pseudo-radial polarisation.

where $\mathbf{r}$ is the unit vector in the direction of observation, r is the distance from the dipole to the point of observation, k is the wavenumber and ϵ_0 is the free space permittivity.

Taking the dipole as placed in the geometrical focus, the scattered field is calculated over the surface of a sphere, with radius equal to the focal length, for each ray directed from the focus to a point in the exit pupil of the collector lens.[11] This field is then collected and collimated by the collector lens. Thus, the field in the exit pupil of the collector lens is obtained as

$$\mathbf{E}^{(2)}_{(x,y,z)} = B(\theta)\mathbf{R}^{-1}\mathbf{L}^{-1}\mathbf{R}\mathbf{E}^{(s)}_{(x,y,z)} \tag{2.18}$$

where $\mathbf{R}$ and $\mathbf{L}$ are the same as in Eq. (2.5) and $B(\theta)$ is the reciprocal of the apodization function $A(\theta)$, introduced to account for the conservation of energy. Fig. 2.14 shows the Stokes parameters in the exit pupil of the collector lens for an *on axis* point-scatterer in the focal plane with incident light linearly polarised in the x-direction ($\mathbf{p}$ is given by Eqs. (2.3)).[12] Each point in the exit pupil corresponds to a particular

[11] The calculation of the scattered field has to be done over a spherical surface to satisfy the aplanatism assumed for the lens.

[12] In this work the terms *on axis* and *off axis* refer to the position of the point-scatterer with respect to the optical axis, i.e. the z-axis in our coordinate system.

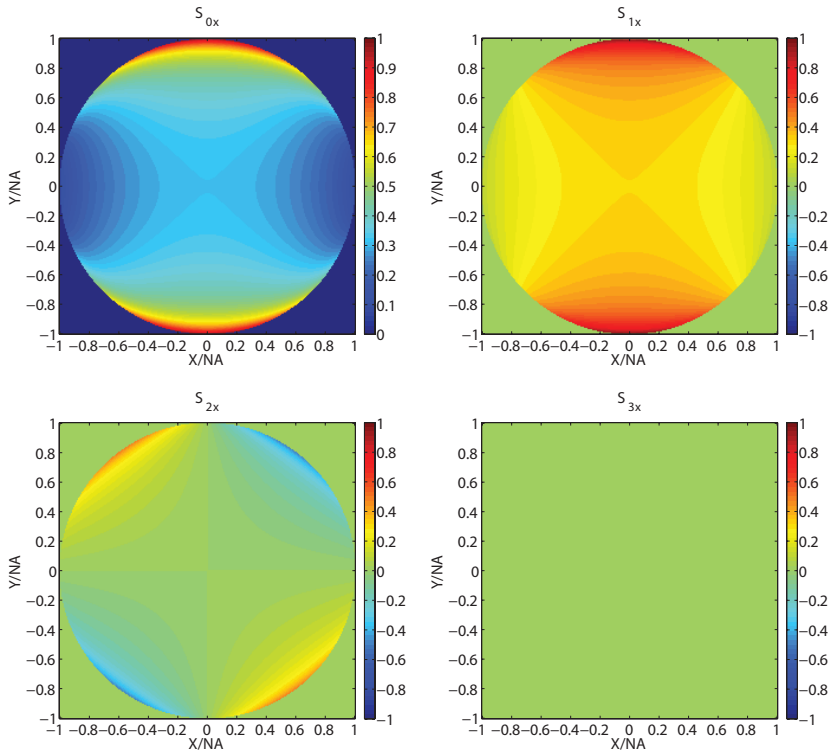

Figure 2.14: Stokes parameters in the exit pupil of the collector lens for an *on axis* point-scatterer in the focal plane with incident light, i.e. before focusing, linearly polarised in the x-direction. The Stokes parameters are normalized with respect to the maximum irradiance.

scattering angle, i.e. the four pupils in Fig. 2.14 are the scattering-angle-resolved Stokes parameters of the scattered field. From the figure, it is apparent that the polarisation state, described by the Stokes parameters, is not homogeneous across the exit pupil of the collector lens. This inhomogeneity stems from the scattering-angle dependence of the scattered field components and the projection of the longitudinal component over the transversal components; this is the kind of information that the *vectorial polarimetry* method retrieves.

To understand the Stokes parameters shown in Fig. 2.14 recall that the dipole field detected by an observer depends on the angle between the dipole moment and the direction of observation, as well as on the distance to the point of observation. That is, for a given direction of observation, the observer sees a dipole moment equal to the projection of the actual dipole moment over a plane orthogonal to the direction of observation. Thus, its magnitude and orientation are different for different directions of observation. This characteristic of the radiated field gives the dipole its particular toroidal radiation distribution. On the other hand, large values of θ correspond to large values of $B(\theta)$, the reciprocal of the apodization function. Recall that $B(\theta)$ was introduced for the conservation of energy. Therefore, the irradiance of the radiated field is larger at the rim of the exit pupil. The combination of both effects is observed in elements S_{0x}, S_{1x} and S_{2x} of Fig. 2.14, whereas S_{3x} equal to zero indicates that there is no circularly polarised component of the radiated field; this is to be expected, from the discussion above, for a linearly polarised incident field. Fig. 2.15 shows the Stokes parameters for the same case shown in Fig. 2.14 but normalized with respect to the irradiance distribution, i.e. pixel by pixel. This kind of normalization removes the irradiance variations in the Stokes parameters distribution and is useful to analyse the polarisation state distribution. However, as it shall be discussed in Chap. 5, we decided to analyse our results using a normalization by the maximum irradiance in the pupil.

Another possibility which is of interest, as we shall see later in this section, is to analyse the Stokes parameters in the exit pupil of the collector lens for incident light circularly polarised. Fig. 2.16 shows the results obtained for an *on axis* point-scatterer in the focal plane with right circular incident polarisation. From the figure, we see that S_{0r} is circularly symmetric whereas S_{1r} and S_{2r} have a two-fold symmetry. Note that S_{2r} is rotated 45°, around the optical axis, with respect to S_{1r}. These distributions can be understood using the same argument of the direction of observation given above, but for a dipole whose dipole

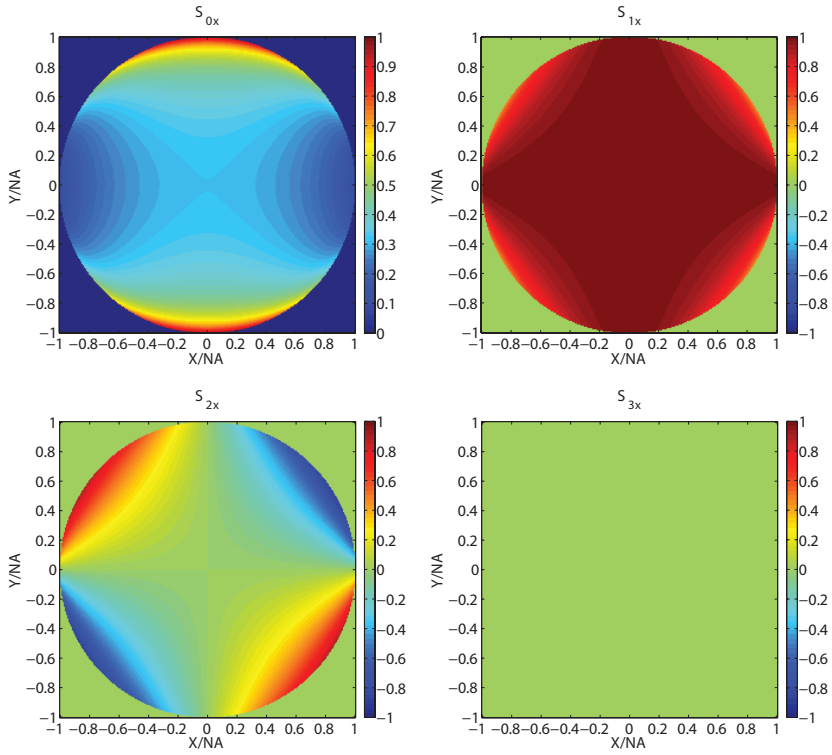

Figure 2.15: Stokes parameters in the exit pupil of the collector lens for an *on axis* point-scatterer in the focal plane with incident light, i.e. before focusing, linearly polarised in the x-direction. The Stokes parameters, except S_{0x}, are normalized pixel by pixel with respect to the irradiance distribution. S_{0x} is normalized with respect to the maximum irradiance.

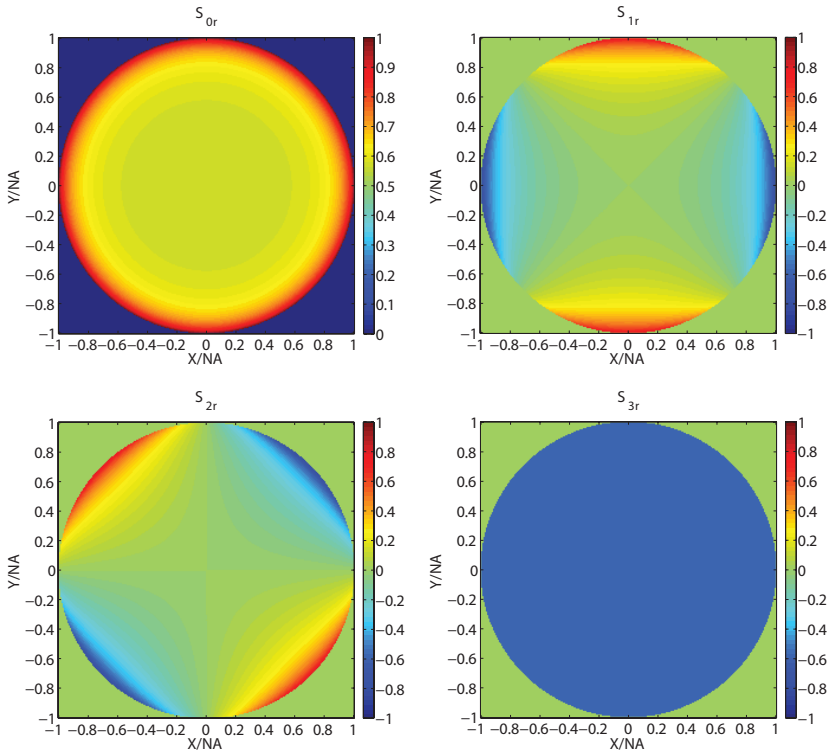

Figure 2.16: Stokes parameters in the exit pupil of the collector lens for an *on axis* point-scatterer with incident light circularly polarised to the right. The Stokes parameters are normalized with respect to the maximum irradiance. The constant value in the distribution of S_{3r} is the same, in absolute value, as the normalized total irradiance in the centre of the pupil, namely, 0.569.

moment is describing a circle around the optical axis. Since the dipole is describing a circle in the focal plane, an observer, at a distance equal to the focal length from this plane, moving away from the optical axis sees a dipole moment equal to the projection of the circular dipole moment over a plane perpendicular to the direction of observation. Thus, when the distance from the optical axis is increased, the ellipse described by the projection of the circular dipole moment shortens in the direction parallel to the direction of the displacement, remaining constant in the orthogonal direction. As a consequence, as the distance from the optical axis is increased, the component of the scattered field linearly polarised in the direction orthogonal to the direction of the displacement is increased.

In Fig. 2.16, we can also see that S_{3r} is different from zero with a constant value across the pupil; this value corresponds to the total irradiance in the centre of the pupil (0.569 when normalized with respect to the maximum irradiance in the pupil). The existence of a circularly polarised component is not surprising since the incident light is circularly polarised. The handedness, on the other hand, is changed because we are modelling the performance of the vectorial polarimeter in a reflection configuration. Finally, we note that, although S_{3r} remains constant across the exit pupil, its relative irradiance, with respect to the total irradiance given by S_{0r}, is reduced as we go further from the centre of the pupil.

So far, we have discussed two different illuminations for an *on axis* point-scatterer. As we saw, the distribution of the Stokes parameters in the exit pupil depends on the characteristics of the incident field. Since the EM field distribution has a non-constant profile around the focal region, it is worth analysing the polarisation distribution in the exit pupil of the collector lens for a slightly *off axis* point-scatterer. Fig. 2.17 is a diagram of the focal plane with the *on axis* and *off axis* positions of the point-scatterer analysed in this work marked. For *off axis* positions, the z components of the electric field for the different rays coming from the pupil to the point of observation do not cancel out and an effective z component appears. The change in the relative phase between the z components, at positions different from the geometrical focus, is the main reason for the existence of the z component.

Figs. 2.18 and 2.19 show the Stokes parameters in the exit pupil for a point-scatterer in the focal plane at $x = -\lambda/3$ and $x = +\lambda/3$, respectively, with incident light linearly polarised. From the figures, it is clear that the Stokes vector for the *off axis* point-scatterer is different from that for the *on axis* scatterer shown in Fig. 2.14. However, the first

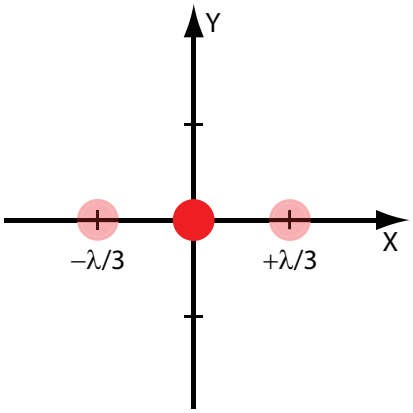

Figure 2.17: Diagram of the focal plane marking the three positions of the point-scatterer analysed. The origin of the XY coordinate system corresponds to the *on axis* position.

three Stokes parameters are the same in both vectors indicating that the information contained in them is not enough to differentiate between the two positions of the scatterer. The fourth elements have a similar distribution in both vectors but the handedness is reversed. Therefore, S_{3x} can be used to distinguish between the two *off axis* positions of the scatterer.

A look at the components of the EM field in the focal region reveals that the E_y component is zero along the x-axis and the E_x component has the same value at both positions of the scatterer. The value of the E_z component at $x = -\lambda/3$, on the other hand, is the negative of its value at $x = +\lambda/3$. Thus, the key to distinguish between the two *off axis* positions is in the E_z component of the focused field. The fact that E_y is zero along the x-axis, for incident light linearly polarised in the x-direction, whereas E_x and E_z are non-zero, shows that the electric field along this axis oscillates in a plane orthogonal to the focal plane.[13] Therefore, using the same arguments about the direction of observation, we can see that, for an observer moving along the x-axis, the effective dipole moment is always a linear dipole with magnitude that increases as he moves away from the optical axis. If the observer now moves along the y-axis, he sees an ellipse with increasing circularly polarised component as the distance from the optical axis is increased. The handedness of the circularly polarised component depends on the phase of the z component,

[13]Richards and Wolf showed in [16] that for every point in the focal plane, the polarisation ellipse is orthogonal to that plane.

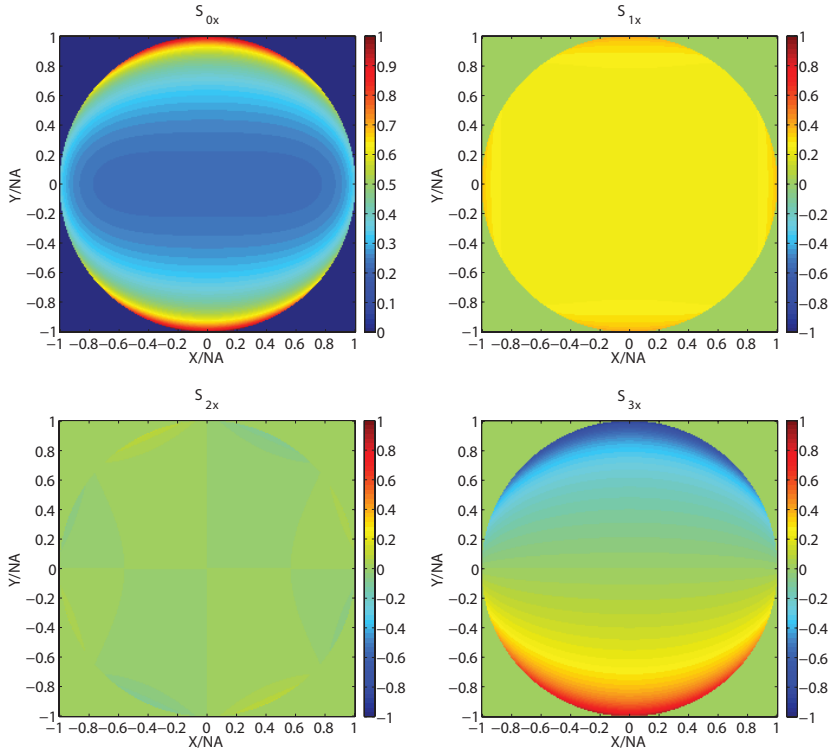

Figure 2.18: Stokes parameters in the exit pupil of the collector lens for a point-scatterer in the focal plane at $x = -\lambda/3$ with incident light linearly polarised. The Stokes parameters are normalized with respect to the maximum irradiance.

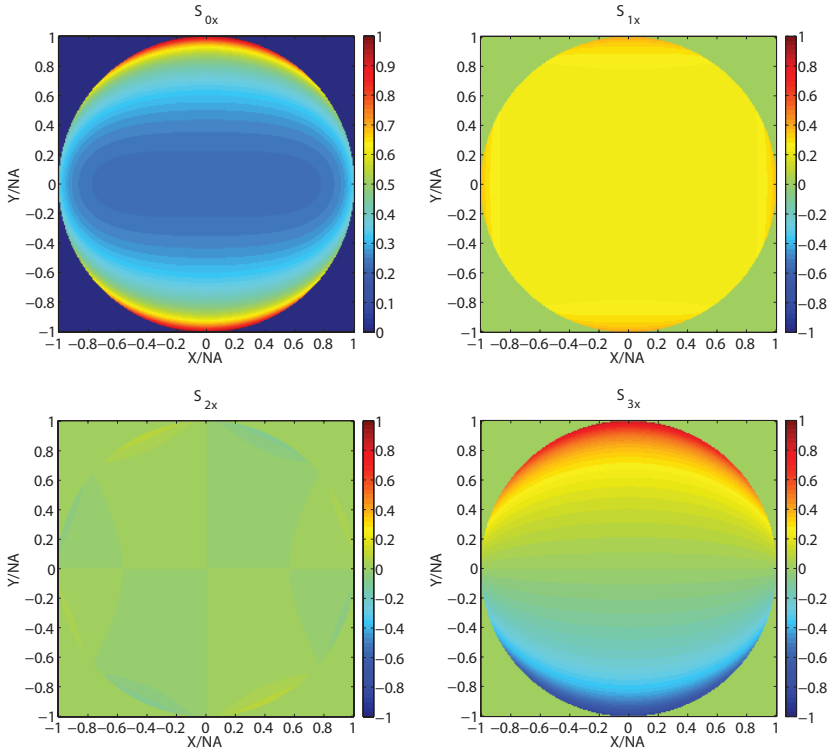

Figure 2.19: Stokes parameters in the exit pupil of the collector lens for a point-scatterer in the focal plane at $x = +\lambda/3$ with incident light linearly polarised. The Stokes parameters are normalized with respect to the maximum irradiance.

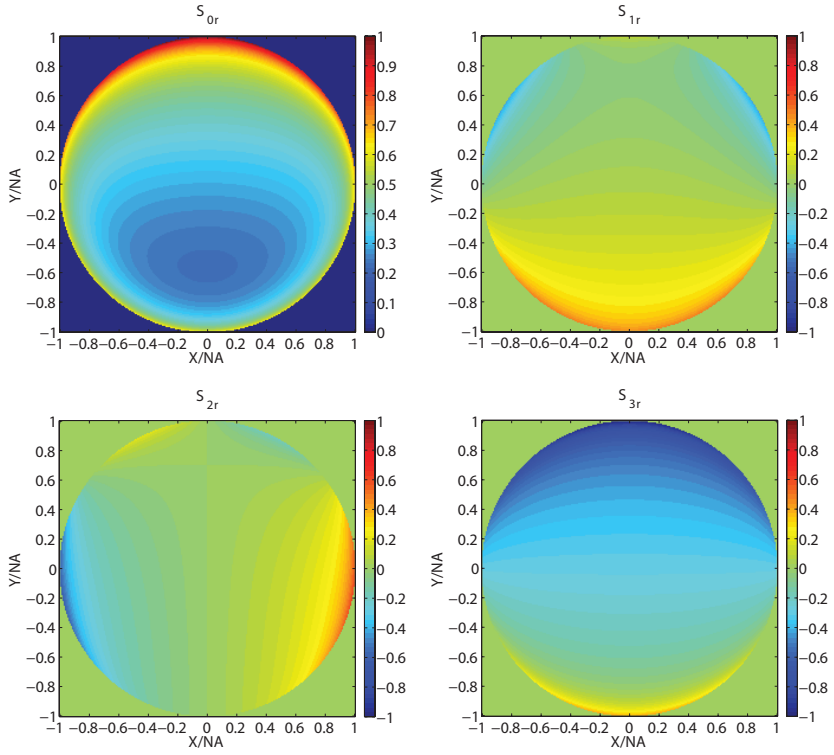

Figure 2.20: Stokes parameters in the exit pupil of the collector lens for a point-scatterer in the focal plane at $x = -\lambda/3$ with incident light circularly polarised to the right. The Stokes parameters are normalized with respect to the maximum irradiance.

which is consistent with the π phase difference between the two *off axis* positions.

The Stokes vectors in the exit pupil of the collector lens for an *off axis* point-scatterer with incident light circularly polarised to the right are shown if Figs. 2.20, for $x = -\lambda/3$, and 2.21, for $x = +\lambda/3$.

In this case, it is also clear that the *off axis* Stokes parameters are different from the *on axis* ones. Furthermore, the four Stokes parameters are different for the two positions of the *off axis* point-scatterer. The analysis of the EM field distribution in the focal region reveals that the E_x and E_y components are different from zero, and from each other, and have the same value at both *off axis* positions. Furthermore, just as for the case of incident light linearly polarised, the value of the E_z component at $x = -\lambda/3$ is the negative of its value at $x = +\lambda/3$, indicating the importance of the E_z component to differentiate between the two positions of the scatterer. Since the E_x and E_y components are

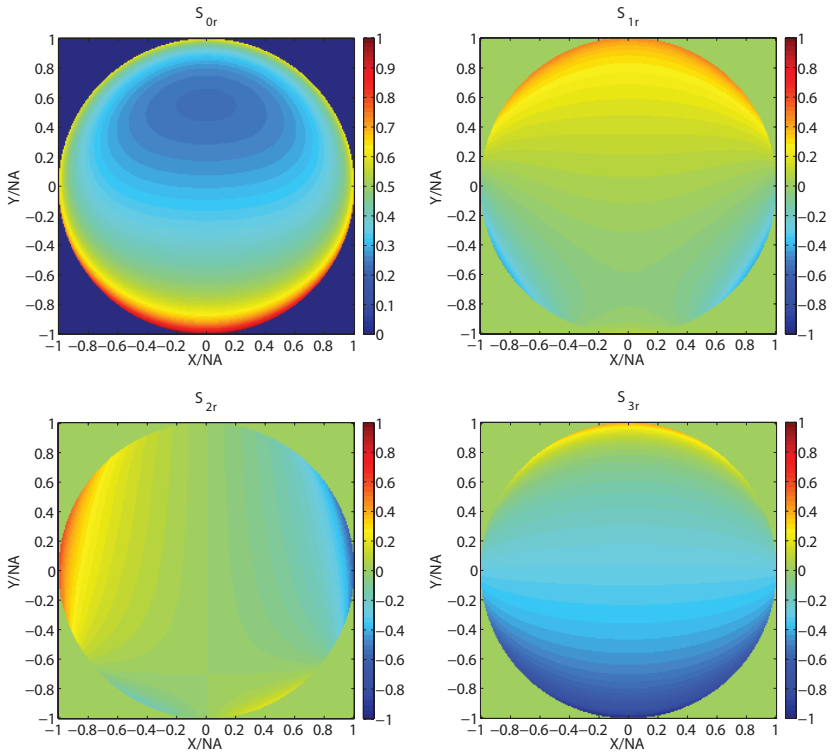

Figure 2.21: Stokes parameters in the exit pupil of the collector lens for a point-scatterer in the focal plane at $x = +\lambda/3$ with incident light circularly polarised to the right. The Stokes parameters are normalized with respect to the maximum irradiance.

different from zero, the polarisation ellipse will be tilted when compared to the case of incident light linearly polarised. However, the scattered field distribution in this case is not as straightforward to interpret as the previous case and requires further analysis.

An important remark concerning the results presented in this section is that, for all the cases analysed, the degree of polarisation remained unity at every pixel. Thus, just as expected, the point-scatterer does not affect the degree of polarisation.

It is important to notice that the displacement of the point-scatterer in each direction ($\lambda/3$) is well below the diffraction limit (0.61λ according to Rayleigh's criterion). Therefore, Figs. 2.18–2.21 show that the *vectorial polarimetry* method can be used to retrieve sub-diffraction information of the scatterer's position.

The maximum resolution that can be achieved with the *vectorial polarimetry* method depends on the variations of the focused field, which can be engineered by tailoring the incident polarisation state (see §2.5), and on the ability to differentiate between exit pupil distributions of the Stokes parameters. In this section we have done a qualitative analysis of the differences between pupil distributions. However, a good way to determine the maximum resolution of the *vectorial polarimetry* method would be to define a metric to measure, quantitatively, the difference between two pupil distributions of a given Stokes parameter. This metric should consider the statistics of the distributions, the noise in the measurements (not included in the analysis above) and an appropriate threshold to determine if a change in the position has occurred.

With the FDTD method-based programme and the NTFF transformation we modelled the Stokes parameters in the exit pupil for the sub-resolution objects shown in Figs. 2.6–2.8. Nevertheless, we could not reduce the spurious reflections (see §2.3.1) enough and thus, we obtained unreliable results that we do not present here.

Rather than continuing with a theoretical analysis of the capabilities and limitations of the *vectorial polarimetry* method, we decided to work in getting an experimental proof of concept. The following chapters present the work done in this direction, including the construction of a vectorial polarimeter, its calibration and the first experimental results.

Chapter 3

Experimental setup

The numerical results presented in the previous chapter show that, using the *vectorial polarimetry* technique, high sensitivity on sub-diffraction displacements of a point-scatterer can be obtained from the analysis of the polarisation distribution in the exit pupil of a high NA collector lens.

In this chapter, we shall describe the setup built to obtain an experimental proof of concept. The instrument developed, the vectorial polarimeter, is a division of amplitude Mueller matrix polarimeter with extended detectors to obtain, simultaneously, scattering-angle-resolved information of the three-dimensional scattered field.

3.1 Vectorial polarimeter

Division of amplitude is one of the many possible configurations for a polarimeter with the advantage of no moving parts and, thus, high speed data acquisition. The main limitation of this type of polarimeters is that, since the detected light is divided between all of the detection channels, the light available for each channel is reduced and signal to noise ratio might be an issue.

As mentioned in §1.2.3, the basic elements of a polarimeter are the polarisation state generator (PSG) and the polarisation state analyser (PSA). The following two subsections describe the configuration of the PSG and the PSA in the vectorial polarimeter. The description of both elements is given in reference to the diagram of the vectorial polarimeter setup presented in Fig. 3.1.

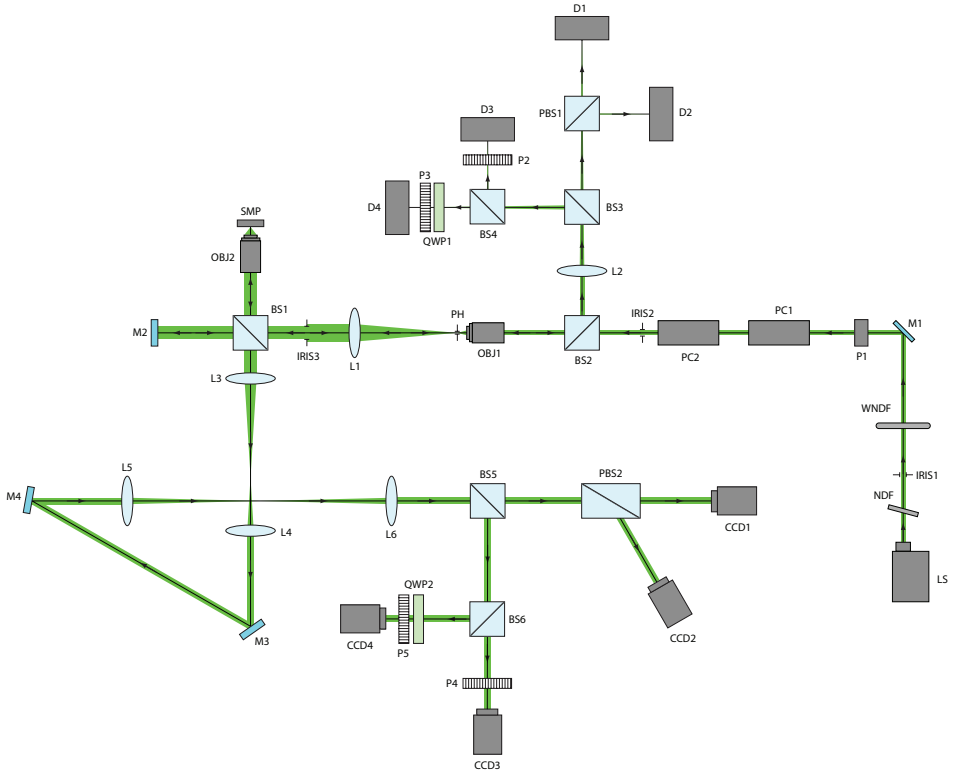

Figure 3.1: Diagram of the vectorial polarimeter setup.

3.1.1 Polarisation state generator (PSG)

The configuration of the vectorial polarimeter's PSG is the following: a linearly polarised diode pumped solid state laser, LS, is the light source.[1] Neutral density filters NDF and WNDF are used to control the amount of light in the system; WNDF is a wheel with different neutral density filters.

Because of the limited size of the optical table, the laser beam is redirected towards the longest side of the table by mirror M1. Then, a Glan-Taylor linear vertical polariser, P1, increases the purity of the reference incident polarisation state. The advantage of using a crystal linear polariser rather than, for instance, a dichroic polymer film polariser, is that the crystal polariser is less likely to produce interference fringes; this point, which became and issue in the measurement of the

[1] MellesGriot 85-GCA-005, λ=532nm. This laser was inherited from a previous setup due to its high stability. However, as we shall discuss in Chap. 6, a more suitable source might be used in future realizations of the vectorial polarimeter.

scattering-angle-resolved Mueller matrices, is further discussed in §4.2.

Two Pockels cells with their fast axis at $-45°$ and $0°$ from the horizontal, PC1 and PC2, respectively, are modulated to convert the linearly polarised incident light into any polarisation state over the Poincaré sphere. Details on the modulation of the Pockels cells are presented in §3.2. Aperture stops IRIS1 and IRIS2 are used as aids in the alignment of the system and to block undesired back reflections from the optical elements. Mirror M2 is an auxiliary mirror used in the alignment of the system. PC2 is the last element of the PSG, the rest of the optical elements described in this subsection are only auxiliary optics.

The light transmitted by the second Pockels cell is spatially filtered with the combination of an objective with focal length f=15.5mm, OBJ1, and a 20μm pinhole, PH.[2] Lens L1, at a distance equal to its focal length from PH, collimates the filtered light and aperture stop IRIS3 chops off the rim of the beam producing a more homogeneous irradiance beam with an aperture diameter of ∼7.5mm. The light is then directed by beam-splitter BS1 towards OBJ2, the high NA objective, which focuses it onto the specimen, SMP. The high NA objective used in the first part of this research is an MPLAPO 100x Olympus objective (of the MPlanApo series) with focal length f=1.8mm and NA=0.95 in air.

The configuration of the vectorial polarimeter shown in Fig. 3.1 corresponds to a reflection type microscope. This is not a necessary condition and the method works, in principle, on transmission as well. In the reflection configuration, OBJ2 is also the collector lens. Therefore, OBJ2 collects and collimates the backscattered light sending it to two different PSAs, namely: the confocal PSA and the pupil PSA, as shall be described in the following subsection.

3.1.2 Polarisation state analyser (PSA)

The first PSA in the vectorial polarimeter measures the polarisation state of the fraction of light collected by OBJ2 that is reflected by BS1 and refocused by L1 onto the position of PH. Pinhole PH limits the light that goes through to a small fraction corresponding to the conjugate of the objective's focus. This is the basic configuration of a confocal microscope. Thus, the PSA associated to this part of the system is known as the confocal PSA.

The light that passes through PH is collimated by OBJ1 and the

[2]The objective is a Linos 038722 which, for a nominal laser beam diameter of 1.1mm, produces an Airy disc with a diameter of 18.8μm.

fraction reflected by BS2 is then refocused by lens L2 onto the position of point detectors D1-D4.[3] Each detector measures a different component of the polarisation state of the light backscattered by the specimen. BS3 is a non-polarising beam-splitter that splits the light in two, sending 50% to the polarising beam-splitter PBS1 and the rest to the non-polarising beam-splitter BS4. PBS1 separates the linear horizontal component, detected by D1, from the linear vertical component, detected by D2. The fraction of light sent to BS4 is divided in two and sent to D3, which has a linear polariser, P2, with its transmission axis at +45° in front of it, and D4, with a combination of a quarter wave-plate with its fast axis at +45°, QWP1, followed by a linear horizontal polariser, P3, in front of it. The combination of QWP1 and P3 constitutes a left-circular analyser. This part of the vectorial polarimeter's PSA is a slight modification of the PSA used in the CMMP developed by Lara [33], being different from the latter only in the position of the confocal pinhole with respect to the incident light. Note that the confocal PSA is formed by detectors D1-D4, polarisers P2-P3 and quarter-wave-plate QWP1. The rest of the optical elements are auxiliary optics.

For the pupil PSA (formed by cameras CCD1-CCD4, polarisers P4-P5 and quarter-wave-plate QWP2), the exit pupil of the collector lens, OBJ2, is imaged onto the position of the cameras by the combination of two simple telescopes.[4] The first telescope, formed by L3 and L4, has a transverse magnification $M_T = 0.5$ and the second one, formed by L5 and L6, has an $M_T = 1$.[5] Mirrors M3 and M4 are used to keep the light within the limits of the optical table.[6] Similarly to the case of the confocal PSA, non-polarising beam-splitter BS5 splits the light sending 50% to the Glan-Thompson polarising beam-splitter, PBS2, that separates the linear vertical component, detected by CCD1, from the linear horizontal, detected by CCD2. The rest of the light is sent to non-polarising beam-splitter BS6. The light impinging on BS6 is divided between CCD3, with a linear polariser at +45° in front of it, P4, and CCD4, with a left-circular analyser (just as the one described above for the confocal PSA) formed by quarter-wave-plate QWP2 and linear polariser P5.

[3] Model 2001 manufactured by New Focus, Inc.

[4] The four CCD cameras are of the model Flea2-08S2M-C manufactured by Point Grey Research, Inc.

[5] L3 is a G063212000 achromat, L4 is a G063215000 achromat and L5 and L6 are G063207000 achromats, all of them from the Linos catalogue.

[6] Both mirrors are Newport Laser Line Dielectric Mirrors with Part No. 10D20DM.11.

3.2 Modulation of the Pockels cells

3.2.1 General remarks

The modulation of the Pockels cells used for the vectorial polarimeter is similar to that presented in [33] with the difference that, in the present work, only 6 of the 256 pairs of voltages, each pair defining an incident polarisation state, were used. The 6 polarisation states chosen are: linear horizontal (H), linear vertical (V), linear at $+45°$ ($+$), linear at $-45°$ ($-$), right circular (R), and left circular (L).

The main reason to limit the number of incident polarisation states to only 6 is that a slower data acquisition rate is used in the pupil PSA because of the limitations of the CCD cameras which have a maximum frame rate of 30 frames per second (FPS). Thus, a larger number of incident polarisation states would increase the time spent in a set of measurements for a given sample. Another disadvantage of a larger number of incident polarisation states is that it would increase the number of image files created by the cameras, increasing the use of disc space for a single measurement.

As it is known in polarimetry, the minimum number of measurements required to determine the complete Mueller matrix of a general sample is 16; the combination of 4 independent incident polarisation states and 4 independent analysers is required. Therefore, with the 6 incident polarisation states, and 4 detection channels in each PSA of the vectorial polarimeter, the total number of measurements is 24 for each PSA, allowing us to obtain the complete Mueller matrix of the sample from an over-determined set of measurements. The over-determination of the measurements implies that some of them are equivalent. However, more than a limitation this is an advantage since the extra information may be used to reduce errors in the experimentally determined Mueller matrices.

A figure of merit commonly used as a measure of the sensitivity of the PSG and PSA to random noise propagation is the condition number. This quantity can be used as long as the set of polarisation states generated (for the PSG) or analysed (for the PSA) is linearly independent; if the set is not linearly independent, the associated matrix is singular and the condition number is not a good measure of the system's sensitivity.

The modulation matrix associated to our 6 polarisation states PSG

is

$$\mathbf{PSG}_6 = \begin{pmatrix} 1 & 1 & 1 & 1 & 1 & 1 \\ 1 & -1 & 0 & 0 & 0 & 0 \\ 0 & 0 & 1 & -1 & 0 & 0 \\ 0 & 0 & 0 & 0 & 1 & -1 \end{pmatrix} \tag{3.1}$$

which has a condition number $\text{cond}(\mathbf{PSG}_6) = \sqrt{3}$. This value is exactly the same as the value for the *Tetrahedron* that corresponds to the optimum configuration for a 4 reconstructed Stokes parameters polarimeter [55, 56].

The analysis matrix associated to each PSA, recall that both PSAs have the same configuration, is

$$\mathbf{PSA}_4 = \frac{1}{2} \begin{pmatrix} 1 & 1 & 0 & 0 \\ 1 & -1 & 0 & 0 \\ \frac{1}{2} & 0 & \frac{1}{2} & 0 \\ \frac{1}{2} & 0 & 0 & -\frac{1}{2} \end{pmatrix} \tag{3.2}$$

with a condition number $\text{cond}(\mathbf{PSA}_4) = 3.6123$. This number is far from the optimum value for a 4 detectors polarimeter but the 4 measurements are completely independent and their experimental implementation is straightforward.

3.2.2 Theoretical modelling of the modulation

Following the treatment presented in [33], each Pockels cell was modelled as a linear retarder with variable retardance. Therefore, its Mueller matrix, when its fast axis is oriented at 0° from the horizontal, is given by

$$\mathbf{P}_{0^\circ}(\tau, \Delta(t)) = \tau \begin{pmatrix} 1 & 0 & 0 & 0 \\ 0 & 1 & 0 & 0 \\ 0 & 0 & \cos\Delta(t) & \sin\Delta(t) \\ 0 & 0 & -\sin\Delta(t) & \cos\Delta(t) \end{pmatrix} \tag{3.3}$$

where τ is the transmittance for unpolarised light and $\Delta(t)$ is the variable retardance.

To calculate the Mueller matrix of a polariser (or a retarder) with transmission (or fast) axis at an arbitrary angle θ, $\mathbf{M}_\theta$, the following expression can be used

$$\mathbf{M}_\theta = \mathbf{R}(\theta)\mathbf{M}_{0^\circ}\mathbf{R}(-\theta) \tag{3.4}$$

where $\mathbf{M}_{0^\circ}$ is the Mueller matrix of the optical element with its axis (whether it is the transmission or the fast axis) parallel to the horizontal direction and $\mathbf{R}(\theta)$ is the rotation matrix given by

$$\mathbf{R}(\theta) = \begin{pmatrix} 1 & 0 & 0 & 0 \\ 0 & \cos 2\theta & -\sin 2\theta & 0 \\ 0 & \sin 2\theta & \cos 2\theta & 0 \\ 0 & 0 & 0 & 1 \end{pmatrix} \tag{3.5}$$

From Eqs. (3.3) and (3.5), the Mueller matrix of the first Pockels cell, PC1, with its fast axis at -45° from the horizontal, is given by

$$\mathbf{P}_{-45^\circ}(\tau_1, \Delta_1(t)) = \tau_1 \begin{pmatrix} 1 & 0 & 0 & 0 \\ 0 & \cos\Delta_1(t) & 0 & \sin\Delta_1(t) \\ 0 & 0 & 1 & 0 \\ 0 & -\sin\Delta_1(t) & 0 & \cos\Delta_1(t) \end{pmatrix} \tag{3.6}$$

where the variable retardance, $\Delta_1(t)$, and the transmittance, τ_1, have a subscript to indicate that they correspond to the first Pockels cell.

Since the fast axis of the second Pockels cell, PC2, is oriented at 0°, its Mueller matrix is given by

$$\mathbf{P}_{0^\circ}(\tau_2, \Delta_2(t)) = \tau_2 \begin{pmatrix} 1 & 0 & 0 & 0 \\ 0 & 1 & 0 & 0 \\ 0 & 0 & \cos\Delta_2(t) & \sin\Delta_2(t) \\ 0 & 0 & -\sin\Delta_2(t) & \cos\Delta_2(t) \end{pmatrix} \tag{3.7}$$

where the subscript in the variable retardance, $\Delta_2(t)$, and the transmittance, τ_2, indicates that they correspond to the second Pockels cell.

The light emerging from the Glan-Taylor polariser, P1, is linearly polarised in the vertical direction. The Stokes vector corresponding to this polarisation state is

$$\mathbf{S}_i = \begin{pmatrix} 1 \\ -1 \\ 0 \\ 0 \end{pmatrix} \tag{3.8}$$

Therefore, the polarisation state of the light after PC2, as a function of the two variable retardances, is given by

$$\begin{aligned} \mathbf{S}_o(t) &= \mathbf{P}_{0^\circ}(\tau_2, \Delta_2(t)) \cdot \mathbf{P}_{-45^\circ}(\tau_1, \Delta_1(t)) \cdot \mathbf{S}_i \\ &= \tau_1\tau_2 \begin{pmatrix} 1 \\ -\cos\Delta_1(t) \\ \sin\Delta_1(t)\sin\Delta_2(t) \\ \sin\Delta_1(t)\cos\Delta_2(t) \end{pmatrix} \end{aligned} \tag{3.9}$$

Eq. (3.9) shows that, with the proper choice of the modulation for the variable retardances, $\Delta_1(t)$ and $\Delta_2(t)$, it is possible to generate any polarisation state over the surface of the Poincaré sphere. However, as mentioned earlier in this chapter, only six linearly independent polarisation states were used in the measurements with the vectorial polarimeter. Their corresponding pairs of retardance, in wavelengths, are shown in Table 3.1. The variable retardances, Δ_1 and Δ_2, have been written without time dependence to emphasize that their values were kept constant during the time taken for the measurements with a given incident polarisation state.

Table 3.1: Retardance pairs, in wavelengths, used in the measurements with the vectorial polarimeter.

Polarisation state	Δ_1	Δ_2
$+$	$-\frac{3}{4}$	$-\frac{3}{4}$
H	$-\frac{1}{2}$	$-\frac{5}{8}$
R	$-\frac{1}{4}$	$-\frac{1}{2}$
V	0	$-\frac{3}{8}$
$-$	$-\frac{3}{4}$	$-\frac{1}{4}$
L	$-\frac{1}{4}$	0

In the following two sections we present the azimuthal alignment of the Pockels cells and the adjustment of the amplitude and bias of the modulation functions. In these adjustments to the experimental setup, we used the modulation programme developed in [33], where the following

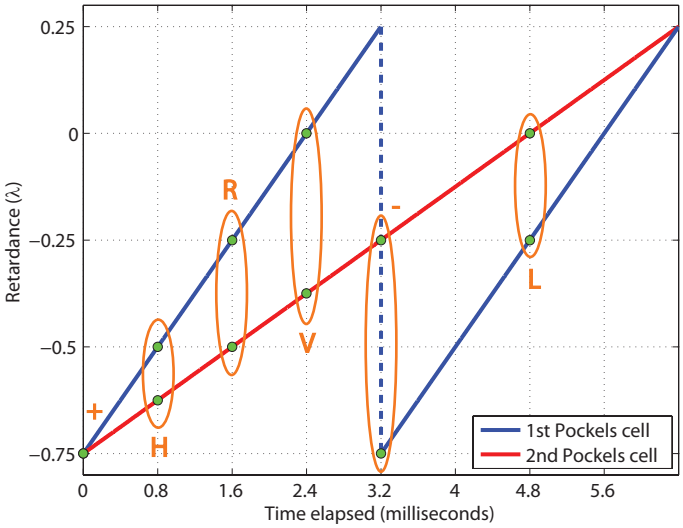

Figure 3.2: Retardance modulation of the the two Pockels cells as a function of time. The 6 pairs of retardances used during the measurements are marked with green dots and labeled with their corresponding polarisation state. The blue and red solid lines are the retardance induced in PC1 and PC2, respectively, during calibration and alignment of the system.

sawtooth modulation parameters were used

$$\Delta_1(t) = 4\pi \text{frac}(\frac{2t}{T_0}) - \frac{3\pi}{2} \tag{3.10}$$

$$\Delta_2(t) = 2\pi \text{frac}(\frac{t}{T_0}) - \frac{3\pi}{2} \tag{3.11}$$

where frac(x) is the fractional part of x and T_0 is the period of the modulation for PC1. Fig. 3.2 is a plot of the retardance modulation, as a function of time, with the 6 incident polarisation states used in the measurements ($+$, H, R, V, $-$ and L) marked and labeled.

3.2.3 Azimuthal alignment of the Pockels cells

To model the alignment of the two Pockels cells at the correct azimuthal orientation of their fast axis, $-45°$ and $0°$, we start by noting that when the reference linear vertical polarisation impinges on PC1 the polarisation

state of the output is given by

$$\mathbf{S}_{o_1} = \mathbf{P}_{-45^\circ}(\tau_1, \Delta_1(t)) \cdot \mathbf{S}_{i_1} = \tau_1 \begin{pmatrix} 1 \\ -\cos\Delta_1(t) \\ 0 \\ \sin\Delta_1(t) \end{pmatrix} \tag{3.12}$$

where $\mathbf{P}_{-45^\circ}(\tau_1, \Delta_1(t))$ is given by Eq. (3.6) and $\mathbf{S}_{i_1}$ is the same as $\mathbf{S}_i$ given by Eq. (3.8). From Eq. (3.12) we can see that $\mathbf{S}_{o_1}$ does not have a linear component at $\pm 45^\circ$ for any value of the modulation parameter $\Delta_1(t)$; the third element of the Stokes vector is identically zero. Thus, by placing PC1 between the linear vertical Glan-Taylor polariser and a linear polariser at, for instance, $+45^\circ$, its fast axis can be aligned by minimizing the transmitted irradiance modulation for all the values of $\Delta_1(t)$.

Similarly, if the light incident on PC2 is linearly polarised at $+45^\circ$, the light transmitted by PC2 will be given by

$$\mathbf{S}_{o_2} = \mathbf{P}_{0^\circ}(\tau_2, \Delta_2(t)) \cdot \mathbf{S}_{i_2} = \tau_2 \begin{pmatrix} 1 \\ 0 \\ \cos\Delta_2(t) \\ -\sin\Delta_2(t) \end{pmatrix} \tag{3.13}$$

where $\mathbf{P}_{0^\circ}(\tau_2, \Delta_2(t))$ is given by Eq. (3.7) and $\mathbf{S}_{i_2}$ is the Stokes vector of light linearly polarised at $+45^\circ$, i.e.

$$\mathbf{S}_{i_2} = \begin{pmatrix} 1 \\ 0 \\ 1 \\ 0 \end{pmatrix} \tag{3.14}$$

We can see that the resulting polarisation state does not have a component linearly polarised in the horizontal and/or vertical direction for any value of the modulation $\Delta_2(t)$; the second element of the Stokes vector is identically zero. Thus, PC2 can be aligned by minimizing the transmitted irradiance modulation, for any value of $\Delta_2(t)$, when the cell is placed between a linear polariser at $+45^\circ$ and, for instance, a linear horizontal polariser.

3.2.4 Adjustment of the amplitude and bias

The modulation of the Pockels cells given by the ramp functions described in §3.2.2 depends on the correct adjustment of the voltage functions sent

to the amplifiers connected to the cells. An error in the amplitude and/or bias of these functions affects the polarisation states generated by the Pockels cells.

To determine the correct amplitude and bias of the voltages sent to the cells, each cell was placed between crossed polarisers, one at a time, and the transmitted irradiance was measured for a set of consecutive modulation cycles. The method can be explained as follows: placing the first Pockels cell between the vertical Glan-Taylor polariser and a horizontal polariser, the polarisation state of the transmitted light, as a function of the retardance modulation, is given by

$$\mathbf{S}'_{o_1} = \frac{\tau_1}{2} \begin{pmatrix} 1 - \cos\Delta_1(t) \\ 1 - \cos\Delta_1(t) \\ 0 \\ 0 \end{pmatrix} \tag{3.15}$$

From the expression above, the irradiance transmitted through the horizontal polariser is, except for a constant factor, $I_H = 1 - \cos\Delta_1(t)$, which corresponds to a cosine function displaced and mirror reflected in a horizontal plane. Thus, the transmitted irradiance has a cosine profile that can be measured with a power meter and an oscilloscope, and the amplitude and bias (or initial phase) of the function sent to the amplifier connected to PC1 can be adjusted to produce a continuous cosine profile, for the transmitted irradiance, with the appropriate initial phase. A discontinuous profile is an indication that the modulation cycle has an incorrect amplitude whereas the bias, or initial phase, can be adjusted to make the voltage pass through zero at the beginning of each cycle.

Placing the second Pockels cell between polarisers at $+45°$ and $-45°$, the Stokes vector after the second polariser is

$$\mathbf{S}'_{o_2} = \frac{\tau_2}{2} \begin{pmatrix} 1 - \cos\Delta_2(t) \\ 0 \\ -(1 - \cos\Delta_2(t)) \\ 0 \end{pmatrix} \tag{3.16}$$

In this case, the transmitted irradiance is $I_- = 1 - \cos\Delta_2(t)$ which, just as for PC1, corresponds to a cosine profile. Therefore, the amplitude and bias of the function sent to the amplifier connected to PC2 can be adjusted to obtain a continuous cosine variation of the transmitted irradiance with the correct initial phase.

The experimental procedure used to adjust the amplitude and bias of the functions sent to the amplifiers, using the method described above,

is discussed in detail in [33], where the Pockels cells were controlled by sending analog voltages to their amplifiers via a digital-to-analog (D/A) PCI board connected to a PC.[7] The resolution of the D/A converter in the board is 16-bit and the same board was also used to read the signals from the point detectors in the confocal PSA.

3.2.5 Stability of the PSG

An important aspect of the vectorial polarimeter is the stability of the PSG; the reliability of measurements taken with the system depends on this property. Every time a set of measurements was done, the amplitude and bias were adjusted and recorded in the logbook. The data recorded showed that these quantities have to be readjusted after a few minutes in order to get the correct modulation for the Pockels cells.[8] This effect was reported by Lara in [33] and it was suggested that it is related to the increase in room temperature due to the heat produced by the equipment and the operator.

Fig. 3.3 is a plot of the values for the adjusted amplitude and bias, inequivalent wavelengths of retardance, for 19 measurements taken at different times during two laboratory sessions. Measurements 1-9 correspond to the first laboratory session and the remaining measurements, 10-19, correspond to the second session. The results presented in the figure show that the variations in the amplitude and bias of the function sent to PC2 are larger than those of the function sent to PC1. If the only source of these variations were the increment in room temperature, we would expect that both Pockels cells would be affected in a similar way. Since this is not the case, we conclude that the voltage function driving PC2 is inherently more instable than the one driving PC1.

Among the possible sources for the instability are the DaqBoard/2000, used to send the functions to the amplifiers, and the amplifier connected to PC2 itself. However, with the currently available data is not possible to determine which of the aforementioned sources, if any, is responsible for the observed instability.

Finally, we note that there is a quite large jump between measurements number 9 and 10, except for the amplitude of PC2, which correspond to the final measurement of the first session and the first measurement of the second session, respectively, indicating that there is an actual dependence of the adjusted amplitude and bias in room temperature.

[7] Digital-to-analog PCI board DaqBoard/2000 manufactured by IOtech.

[8] In some cases the variation in the amplitude and bias was noticeable after each measurement cycle which takes, approximately, 4-5 minutes.

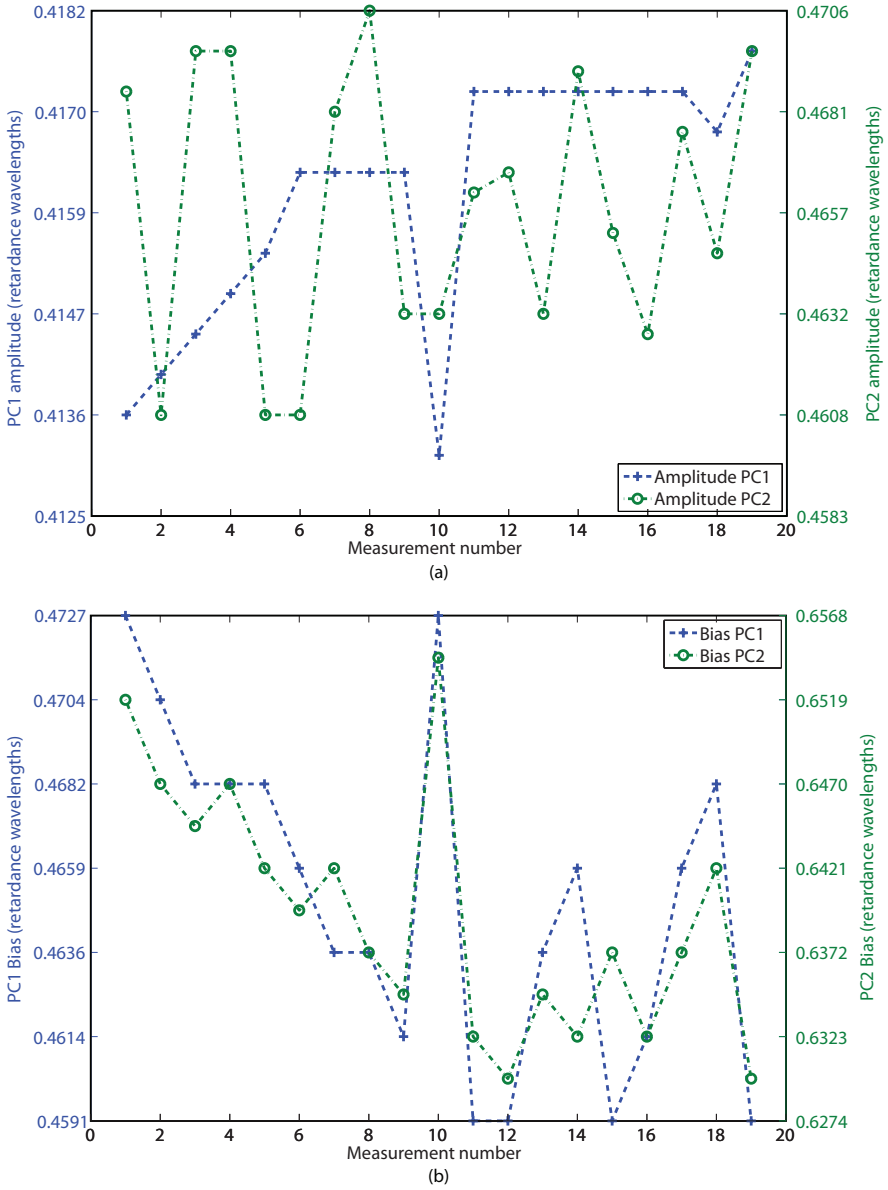

Figure 3.3: Variation of the adjusted (a) amplitude and (b) bias of the functions sent to PC1 and PC2, in equivalent wavelengths of retardance, for 19 different measurements taken in two laboratory sessions. Measurements 1-9 correspond to the first session and measurements 10-19 correspond to the second session.

3.3 Calculation of the Mueller matrix

The calculation of the Mueller matrix from experimental data depends on the nature of the measurement technique. For instance, the Mueller matrix can be obtained from the spectral analysis of the polarimetric measurements [32] or from direct algebraic relations between the measurements [27].

The experimental data obtained with the vectorial polarimeter is suitable for the calculation of the Mueller matrix of the specimen using the method presented in [27].[9] The method presented by Bickel and Bailey establishes four properties of the experimental data and their relation with the elements of the Mueller matrix. However, only two of them are relevant for our analysis, namely:

- The combination polariser-analyser used in a particular measurement determines uniquely the elements of the Mueller matrix mixed in that measurement.
- Measurements taken with the complementary polariser-analyser configurations produce combinations of the same elements of the Mueller matrix that differ only in the sign of the elements.

The analytic relations describing the irradiance measured for a particular combination polariser-analyser are used to determine what set of measurements is necessary to obtain each element of the Mueller matrix. For instance, m_{12} can be obtained as:

$$m_{12} = \frac{1}{2}(I_{H0} - I_{V0}) \tag{3.17}$$

That is, m_{12} is obtained as the difference between the total scattered irradiance for incident light polarised in the horizontal direction and the total scattered irradiance for incident light polarised in the vertical direction. None of the PSAs in the vectorial polarimeter measures the total irradiance and, thus, this quantity is obtained indirectly as the incoherent superposition of the horizontal and vertical components. Therefore, m_{12} for the vectorial polarimeter is obtained as:

$$m_{12} = \frac{1}{2}[(I_{HH} + I_{HV}) - (I_{VH} + I_{VV})] \tag{3.18}$$

[9] The original CMMP obtained the Mueller matrix using spectral analysis. The modified CMMP, included in the vectorial polarimeter as the confocal PSA, uses the method described in this section.

Similar expressions can be found for the rest of the elements. Fig. 3.4 shows the measurements and operations necessary to calculate the complete Mueller matrix of a specimen. The expressions presented in the figure are given in terms of measurements that are not available in the vectorial polarimeter; none of the PSAs includes neither a $-45°$ nor a right-circular analyser. Nevertheless, since some of the measurements are redundant, we can write most elements of the Mueller matrix, except m_{11}, in terms of other elements previously calculated. As an example, let us consider again the element m_{12} given by Eq. (3.18).

The first element of the Mueller matrix in the vectorial polarimeter is given by

$$m_{11} = \frac{1}{2}[(I_{HH} + I_{HV}) + (I_{VH} + I_{VV})] \tag{3.19}$$

Therefore,

$$m_{11} + m_{12} = I_{HH} + I_{HV} \tag{3.20}$$

from which

$$m_{12} = I_{HH} + I_{HV} - m_{11} \tag{3.21}$$

Thus, m_{12} is given in terms of a couple of measurements and m_{11}. Again, similar relations can be found for the rest of the elements of the Mueller matrix.

Because of the configuration of the PSA in the vectorial polarimeter, an extra clarification is required. Non-polarising beam-splitter BS6, in the pupil PSA, halves the irradiance impinging on CCD3 and CCD4 compared to the irradiance impinging on CCD1 and CCD2.[10] This extra reduction in the relative irradiance has to be taken into account in the calculation of the Mueller matrix.

3.4 Alignment and synchronization of the CCD cameras

The operations involved in the calculation of the Mueller matrix from the data obtained with the pupil PSA are done pixel by pixel. Therefore, the correct alignment of the CCD cameras, to make sure that corresponding pixels in the cameras coincide and that all of the images are in focus, is paramount.

The cameras were focused using a custom-made alignment target and an incoherent extended light source. The alignment target consisted of

[10] BS4 has the same effect over the irradiance detected by D3 and D4, compared to D1 and D2, in the confocal PSA.

m_{11} ✳ ✳	m_{12} ↔ ✳	m_{13} ⤢ ✳	m_{14} ↻ ✳
I_{00}	$\frac{1}{2}[I_{H0} - I_{V0}]$	$\frac{1}{2}[I_{+0} - I_{-0}]$	$\frac{1}{2}[I_{R0} - I_{L0}]$
m_{21} ✳ ↔	m_{22} ↔ ↔	m_{23} ⤢ ↔	m_{24} ↻ ↔
$I_{0H} - I_{0V}$	$\frac{1}{2}[(I_{HH} + I_{VV}) - (I_{VH} + I_{HV})]$	$\frac{1}{2}[(I_{+H} + I_{-V}) - (I_{-H} + I_{+V})]$	$\frac{1}{2}[(I_{RH} + I_{LV}) - (I_{LH} + I_{RV})]$
m_{31} ✳ ⤢	m_{32} ↔ ⤢	m_{33} ⤢ ⤢	m_{34} ↻ ⤢
$I_{0+} - I_{0-}$	$\frac{1}{2}[(I_{H+} + I_{V-}) - (I_{V+} + I_{H-})]$	$\frac{1}{2}[(I_{++} + I_{--}) - (I_{-+} + I_{+-})]$	$\frac{1}{2}[(I_{R+} + I_{L-}) - (I_{L+} + I_{R-})]$
m_{41} ✳ ↻	m_{42} ↔ ↻	m_{43} ⤢ ↻	m_{44} ↻ ↻
$I_{0R} - I_{0L}$	$\frac{1}{2}[(I_{HR} + I_{VL}) - (I_{VR} + I_{HL})]$	$\frac{1}{2}[(I_{+R} + I_{-L}) - (I_{-R} + I_{+L})]$	$\frac{1}{2}[(I_{RR} + I_{LL}) - (I_{LR} + I_{RL})]$

Note: ✳ Unpolarised ⤢ Linear at 45°
↔ Linear horizontal ↻ Right circular

Figure 3.4: Measurements and operations necessary to compute each of the 16 elements of the Mueller matrix [27]. From left to right, the first symbol, and subscript of I, represents the polarisation state of the incident light whereas the second symbol, and subscript, represents the analyser used in the corresponding measurement. The convention followed for the subscripts is the same as in §3.2.1 with the extra '0' indicating unpolarised light, for the incident light, or total irradiance, for the analyser.

a cross made with a piece of wire tied-up to a cage of the same type as those used to built the vectorial polarimeter. The incoherent extended light source was a torch with a piece of ground tape in front of it. The custom-made alignment target was placed in the position were the exit pupil of the microscope objective is, when the system is complete, and the extended source was pointed from the position of the sample towards the relay imaging optics of the pupil PSA.

Although this technique might seem rough at a first glance, it proved to be appropriate to bring the CCD cameras to focus. In fact, the alignment of the cameras using the coherent light source of the vectorial polarimeter, LS, instead the incoherent extended light source, was more difficult due to diffraction by the wire.

The right correspondence between pixels was achieved in two steps:

- Coincidence of the pupil images in the cameras, i.e. same spherical angle, θ, for the corresponding set of pixels
- Correct orientation of the cameras, i.e. same azimuthal angle, ϕ, for corresponding pixels.

The alignment of the spherical angle, θ, was done taking the cross-correlation between three images (CCD2-CCD4) with the reference image (CCD1) and adjusting their horizontal and vertical position, x and y, respectively, until the cross-correlation function had its maximum in the center; this indicates that the two pupils are covering the same area of the CCD detectors (Fig. 3.5a).

The azimuthal alignment of the cameras (Fig. 3.5b) was done using a vertical wire passing through the center of the aperture and rotating the cameras until the image of the wire was vertical in all of them. Then, a fine adjustment was done taking the cross-correlation of the reference image (CCD1) with the other three images (CCD2-CCD4) and adjusting the azimuthal orientation of the cameras to maximize the cross-correlation.

The detection and analysis of sub-resolution features requires an active scanning of the specimen. Thus, the polarimetric measurements have to be done synchronously. From the beginning, the Pockels cells modulation was synchronized with the data acquisition of the confocal PSA; the CMMP was built with this in mind [33]. The integration of the CCD cameras with the rest of the system required the synchronization of each camera with the others and with the modulation cycle. The cameras were synchronized using the programme MultiSync©, developed by PointGrey Research, Inc., and the synchronization with the modulation

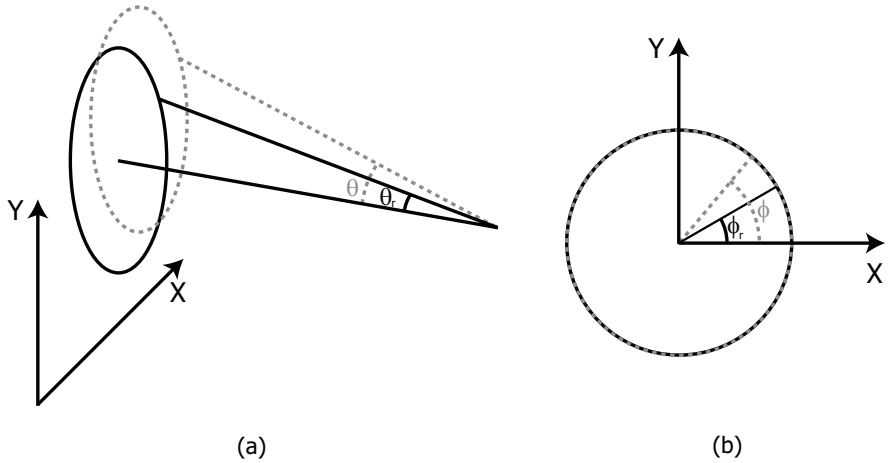

Figure 3.5: Diagram of the (a) spherical angle, θ, and (b) azimuthal angle, ϕ, alignment of the CCD cameras. θ_r and ϕ_r are the spherical and azimuthal angles of pixels in the reference camera (CCD1).

cycle was done in software by keeping the modulation constant during the acquisition of the images with the cameras. An extra line was included in the programme to beep whenever a picture, taken by any of the cameras, is out of synchronization and to display the number of frames, and camera number, out of sync.

The maximum frame rate achievable with the CCD cameras is 30FPS. However, to avoid recording out of sync images, we reduced the frame rate to the minimum, 1.875FPS. This does not represent a problem in the measurements presented in this work since we are only considering static samples. In this configuration, each measuring cycle, for a single image recording, takes ∼36-40 seconds.

This concludes our discussion on the vectorial polarimeter setup. The following chapter describes the calibration of the system.

Chapter 4

System calibration

Although the theoretical performance of a polarimeter can be optimized to obtain accurate measurements of the Mueller matrix of a specimen, the experimental realization of such a system is not always straightforward. Thus, the performance of a polarimeter is limited by experimental constraints.

Due to the polarisation dependence of Fresnel coefficients, whenever light passes through an optical element its polarisation state is affected. The amount and exact nature of the artefacts introduced in the polarisation depend on the geometry and material properties of the optical element. To take into account these effects, the polarimeter has to be properly calibrated. Compain *et al.* [21] introduced a calibration method, to minimize the effects of the polarisation artefacts introduced by the optical elements in a polarimeter, that does not require an accurate modelling of the optics in the system. Their method is known as the *eigenvalue calibration method* and, with a slight modification with respect to the original formulation, is the method used to calibrate the vectorial polarimeter.

4.1 Eigenvalue calibration method

The modified *eigenvalue calibration method* (ECM) used in this work is based on the idea that the polarisation artefacts introduced by the optical elements between the PSG and the sample can be represented by a system matrix $\mathbf{W}$. In a similar way, the artefacts introduced by the elements between the sample and the PSA can be represented by another system matrix $\mathbf{A}$. Therefore, if $\mathbf{W}$ and $\mathbf{A}$ are known, and they are invertible (as it is expected for a complete polarimeter), the Mueller

matrix of the sample can be obtained from the experimental data by multiplying the experimentally determined Mueller matrix, $\mathbf{M}_{\text{exp}}$, by the inverse of $\mathbf{W}$ and $\mathbf{A}$.

The main difference between the original ECM and the modified version used in this work is that $\mathbf{W}$ and $\mathbf{A}$ are the modulation and analysis matrices of the PSG and PSA, respectively, in the original formulation whereas, in the variation used herein, they are 4×4 square matrices containing only the polarisation artefacts introduced by the system. That is, in the absence of experimental errors, $\mathbf{W}$ and $\mathbf{A}$ reduce to Eqs. (3.1) and (3.2), respectively, in the original ECM whereas, in the modified ECM, they reduce to identity matrices.

The modified ECM can be further explained as follows: the Stokes vector of the light impinging onto the sample is obtained as the product of the Stokes vector generated by the PSG multiplied by $\mathbf{W}$. After interaction with the sample, represented by the multiplication by its Mueller matrix, the resulting Stokes vector is then multiplied by the second system matrix, $\mathbf{A}$, producing the polarisation state that is measured with the PSA. Mathematically, this can be expressed as follows:

$$\mathbf{S}_{\text{PSA}} = (\mathbf{A} \cdot \mathbf{M} \cdot \mathbf{W})\mathbf{S}_{\text{PSG}} \tag{4.1}$$

where $\mathbf{S}_{\text{PSG}}$ and $\mathbf{S}_{\text{PSA}}$ are the Stokes vectors that represent the polarisation state generated by the PSG and measured with the PSA, respectively, and $\mathbf{M}$ is the Mueller matrix of the sample. Thus, the Mueller matrix obtained from the measurements with the system is

$$\mathbf{M}_{\text{exp}} = \mathbf{A} \cdot \mathbf{M} \cdot \mathbf{W} \tag{4.2}$$

The problem now is to determine $\mathbf{W}$ and $\mathbf{A}$. Compain *et al.* [21] proved that $\mathbf{W}$ can be obtained as the null space of the system

$$\mathbb{H}_M : \mathbf{X} \rightarrow (\mathbf{M}) \cdot \mathbf{X} - \mathbf{X} \cdot (\boldsymbol{aw})^{-1}(\boldsymbol{a}(\boldsymbol{m})\boldsymbol{w}) \tag{4.3}$$

where the uppercase variables represent theoretical matrices and the lowercase italic variables represent their experimentally obtained counterparts. In Eq. (4.3), $\mathbf{X}$ is the unknown to be determined. When $\mathbf{X}$ is equal to $\mathbf{W}$, as Compain *et al.* proved it, the right hand side of Eq. (4.3) is identically zero in the absence of experimental errors; that is the key to find $\mathbf{W}$.

To determine $\mathbf{W}$ unambiguously it is necessary to use a sufficiently large number of linearly independent calibration samples with known theoretical Mueller matrix. De Martino *et al.* [57] showed that $\mathbf{W}$ can

be obtained from the experimental Mueller matrices of four samples, namely: free space, a linear horizontal polariser, a linear vertical polariser and a linear retarder with fast axis at 30°. The details of Compain *et al.* method, as well as De Martino *et al.* optimum selection of calibration samples, are beyond the scope of this work and the interested reader is referred to their original work.

Once the matrix $\mathbf{W}$ is known, $\mathbf{A}$ can be determined from the experimental Mueller matrix of free space as

$$\mathbf{A} = \boldsymbol{aw} \cdot (\mathbf{W}^{-1}) \tag{4.4}$$

where the Mueller matrix of free space is given by the identity matrix and thus, it is not explicitly written in Eq. (4.4).

The vectorial polarimeter developed in this research was built to work in reflection. This configuration was chosen due to the high reflectivity of the specimens considered in the numerical modelling of the system. Under these circumstances, it is not possible to calibrate the system by direct application of the modified ECM since the light passes twice through the calibration samples.

In [33], Lara introduced the *double-pass eigenvalue calibration method* (DP-ECM) as an extension of the original ECM for systems working in the double-pass reflection configuration. During the double-pass through the calibration samples, an optical element with its axis at an angle θ for the first-pass will have its axis at an angle $-\theta$ for the second-pass. This introduces an extra constraint to the ECM, as Lara pointed out in his original work, that has to be considered.

The analysis presented in [33] concluded that the double-pass Mueller matrices of the calibration samples, $\mathbf{B}_\mathbf{i}^{\mathrm{dp}}$, and the calibration matrix $\mathbf{W}$ can be obtained in the same way as in the original ECM, whereas the second calibration matrix, $\mathbf{A}$, is given by

$$\mathbf{A} = \mathbf{B}_\mathbf{0}^{\mathrm{dp}} \cdot \mathbf{W}^{-1} \cdot \mathbf{M}_{\mathrm{Mirror}} \tag{4.5}$$

where the matrix $\mathbf{B}_0^{\mathrm{dp}}$ is the double-pass Mueller matrix measured for free space and $\mathbf{M}_{\mathrm{Mirror}}$ is the Mueller matrix of an auxiliary mirror used in the calibration. By choosing the coordinate system for the representation of the double-pass measurements as the system given by the first-pass, Lara showed that the second calibration matrix is given by the following expression

$$\mathbf{A}^{\mathrm{dp}} = \mathbf{A} \cdot \mathbf{M}_{\mathrm{Mirror}} = \mathbf{B}_\mathbf{0}^{\mathrm{dp}} \cdot \mathbf{W}^{-1} \tag{4.6}$$

Therefore, the calibrated matrices are obtained as

$$\mathbf{M} = (\mathbf{A}^{\mathrm{dp}})^{-1} \cdot \mathbf{M}_{\mathrm{exp}} \cdot (\mathbf{W}^{-1}) \tag{4.7}$$

where, as mentioned above, $\mathbf{M}_{\text{exp}}$ is the Mueller matrix of the specimen as obtained from the measurements.

4.2 Calibration of the pupil PSA

As mentioned in the previous section, the ECM uses the experimentally determined Mueller matrix of four samples, with known theoretical Mueller matrices, to calculate the system matrices $\mathbf{W}$ and $\mathbf{A}$. Since the system was built to work in reflection, an auxiliary mirror, normal to the incident beam, was placed during the calibration, after the calibration samples, to reflect the light transmitted in the first-pass back to the calibration samples and then to the relay optics.

High NA microscope objectives have a short focal length, and an even shorter working distance, that makes impossible to place the calibration samples, other than free space, between the objective and the auxiliary mirror. Therefore, the calibration of the system was done without the objective; the polarisation artefacts introduced by the objective were measured separately (see §4.3).

The difference between the calibration of the confocal PSA, as discussed in [33], and the pupil PSA is that the latter has to be calibrated pixel by pixel for every pixel within the aperture of the beam. That is, the DP-ECM has to be applied to corresponding pixels in the 16 images that form the scattering-angle-resolved Mueller matrix of the specimen.

Although the application of the DP-ECM might seem straightforward once the method has been applied to measurements done with a point detector, in practice it is important to set an appropriate threshold to the values of the Mueller matrix elements to discriminate between pixels within the aperture of the beam, where the matrix has to be calibrated, and pixels outside, where no calibration is required.

To determine if a particular pixel was within the aperture of the beam, a threshold was set on the minimum value of the determinant of the raw Mueller matrix of free space, $\mathbf{B_0}$, for that pixel.[1] This matrix was chosen because, as it is the identity matrix, it is easy to differentiate between pixels within and outside the aperture of the beam. The actual value of the threshold was established, according to the limitations of the analysis programme, to take pixels with associated singular or near-to-singular matrices as pixels outside the aperture of the beam. That is, pixels with a determinant of their corresponding Mueller matrix smaller

[1] In what remains of this thesis, we shall omit the superscript in the double-pass Mueller matrices since no single-pass matrices are considered in this work.

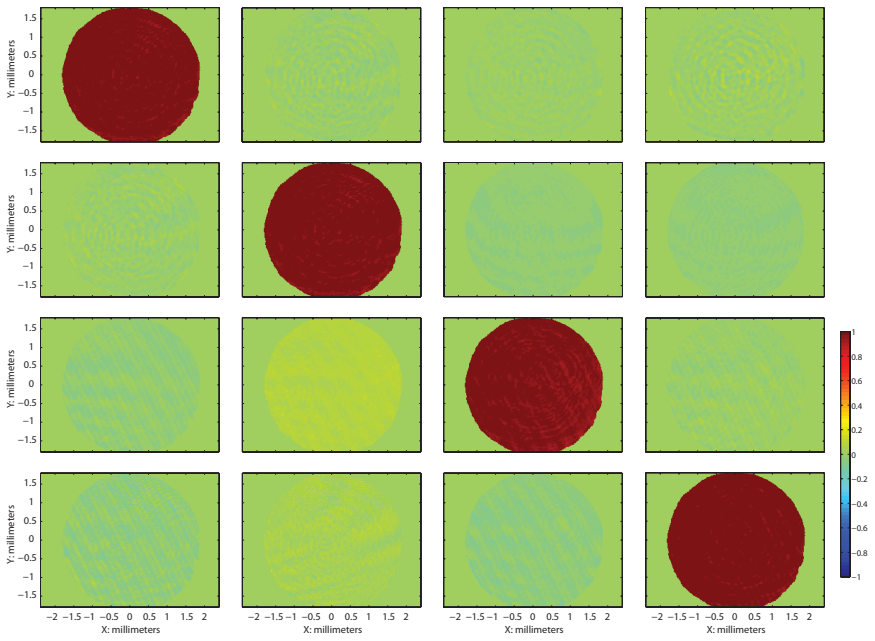

Figure 4.1: Calibrated Mueller matrix of free space, $\mathbf{B_0}$, within the aperture of the incident beam.

than the floating-point relative accuracy of the analysis programme are considered as being outside of the aperture.

The raw images obtained from the experiment were reduced from 768×1024 pixels to 192×256 pixels by applying a 4×4 binning to reduce noise and speed up the data analysis; the pixel by pixel calibration routine takes $\sim$6 hours if the total number of pixels in the raw images is used compared to $\sim$30 minutes for the reduced images. After the binning, a total of 26248 pixels were obtained within the aperture of the pupil for a 49152 pixels image.

The calibration of the system was done with the average of 30 measurements taken with each combination polariser-analyser for all the calibration samples. Then, an independent set of measurements with the calibration samples was taken to use them as experimental data to be calibrated. Fig. 4.1 is the calibrated Mueller matrix of free space obtained as the average of 30 measurements of each combination polariser-analyser. This figure shows the stability of the vectorial polarimeter. Note that most of the polarisation artefacts introduced by the optical elements in the system have been reduced with the calibration. However, it is apparent that there are still some residual artefacts as can be seen in, for instance, m_{42}. These artefacts have a very peculiar form that resembles

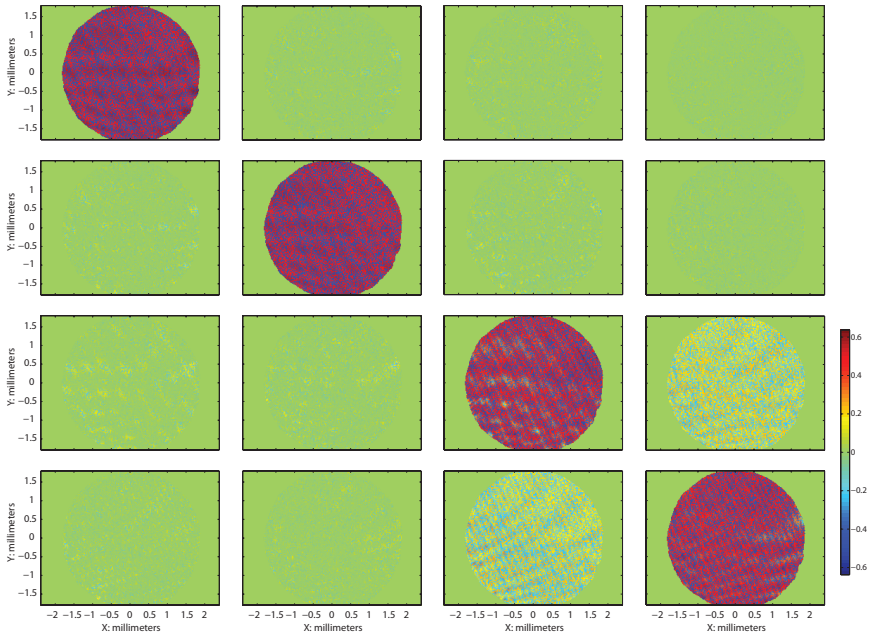

Figure 4.2: Distribution of the calibration matrix **W** within the aperture of the incident beam.

low frequency interference fringes and, in fact, that is their origin. The presence of these fringes is due to a backreflection in the glass pane that protects the CCD detectors and is clearer in elements of the raw Mueller matrix whose calculation is related to the +45° polarised component of the scattered light. Therefore, the low frequency fringes are experimental errors that propagate to the final results during the calibration of the system. This effect can be observed in the distribution of the calibration matrices, **W** and **A**, shown in Figs. 4.2 and 4.3, respectively. As discussed in §4.1, in the absence of errors, **W** and **A** are equal to the identity matrix. From the figures, we can see that this is not the case for the vectorial polarimeter. The distributions obtained for the calibration matrices have the form of the Mueller matrix of a retarder.

The experimentally obtained Mueller matrices for the rest of the calibration samples, also obtained as the average of 30 measurements, are shown in Figs. 4.4, 4.5, and 4.6, for the linear horizontal polariser, linear vertical polariser and linear retarder, respectively.[2] The calibrated Mueller matrices that we would expect for homogeneous specimens, in

[2]The polarisers used in the calibration are Newport 10LP-VIS and the linear retarder is a 633nm third-order quarter-wave-plate that introduces an effective nominal retardance, at 532nm, of $\sim 0.26\lambda$ in double-pass.

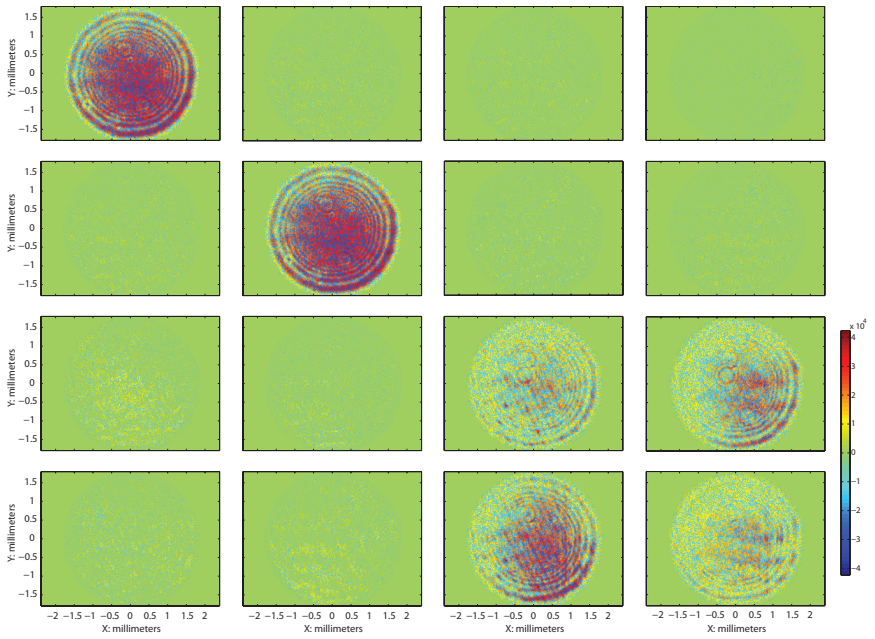

Figure 4.3: Distribution of the calibration matrix **A** within the aperture of the incident beam.

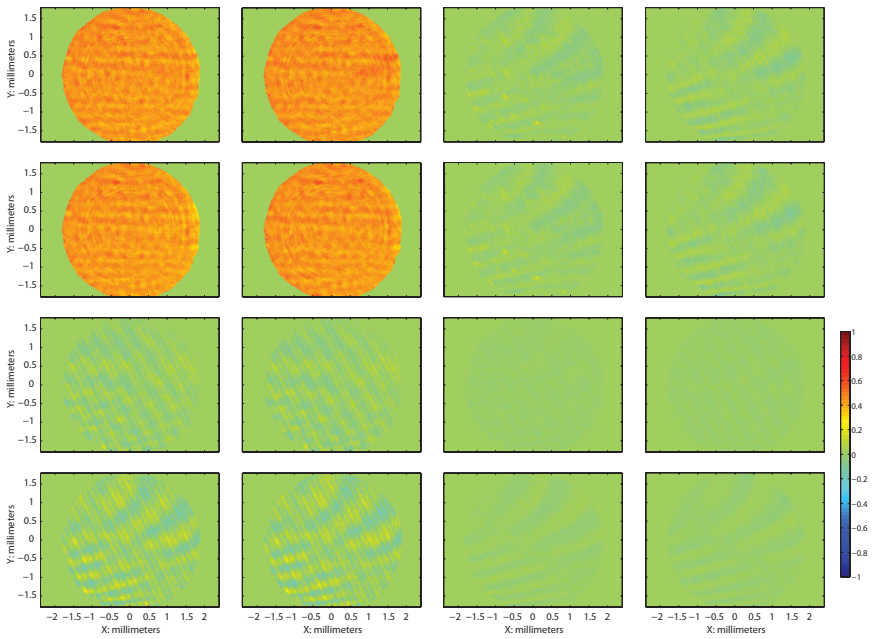

Figure 4.4: Calibrated Mueller matrix of the horizontal polariser, $\mathbf{B_1}$, within the aperture of the incident beam.

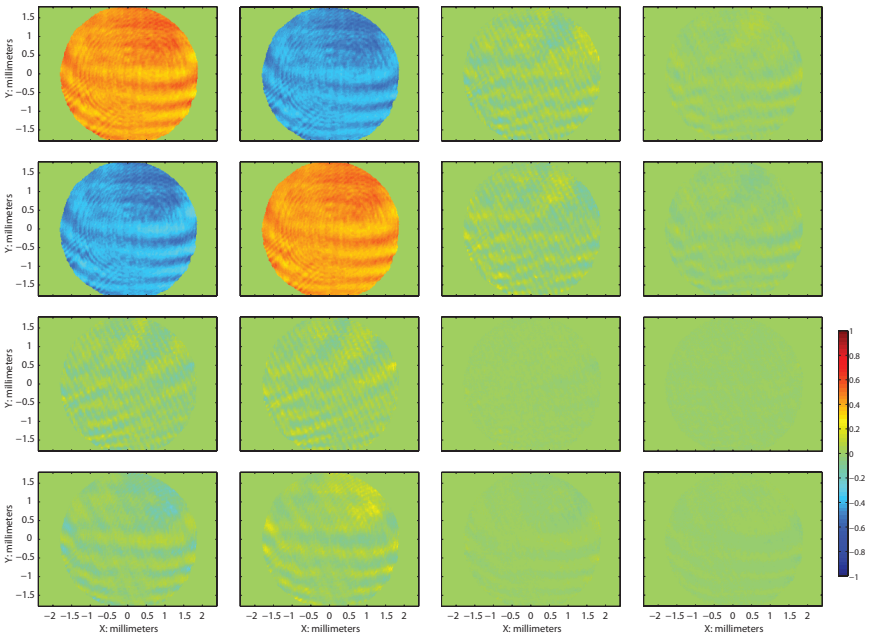

Figure 4.5: Calibrated Mueller matrix of the vertical polariser, $\mathbf{B_2}$, within the aperture of the incident beam.

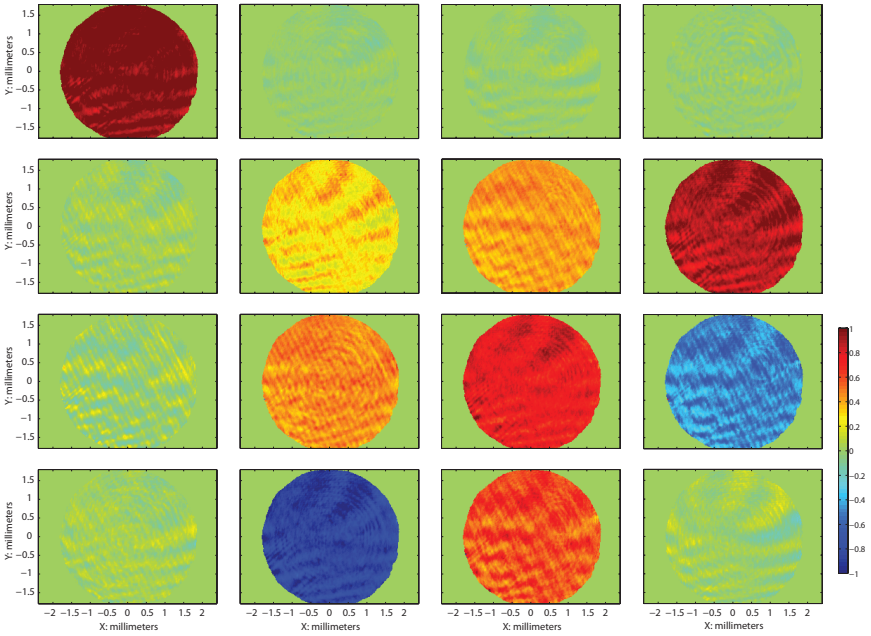

Figure 4.6: Calibrated Mueller matrix of the linear retarder at 30°, $\mathbf{B_3}$, within the aperture of the incident beam.

the ideal case, are constant values across the aperture of the beam, as long as diffraction during propagation is not important. However, variations in the values, other than the fringes discussed above, can be observed in the elements of the Mueller matrix for each calibration sample. Part of these variations are concentric circles around the centre of the aperture, present in the irradiance distribution of the incident beam, that appear as a consequence of chopping-off the rim of the incident beam with IRIS3 (see Fig. 3.1). Other variations observed are high frequency fringes at $-45°$. These fringes were traced back to the linear polariser at $+45°$ (a dichroic polymer film polariser) in front of CCD3; the internal structure of the polymer film polariser is responsible for the high frequency fringes. Finally, dust particles in the optics are also a source of variations in the measured irradiance distributions. Note that all these sources of experimental errors are present in Fig. 4.3, the distribution of calibration matrix **A**. Thus, most of the residual polarisation artefacts are introduced by the optical elements between the sample and the PSA.

To get rid of the variations, it has been suggested to divide by m_{11} all the elements of the Mueller matrix, except m_{11} itself [58]. This method may help to reduce the effect of irradiance variations when a single detector is used in the measurements. However, division by m_{11} is not the best option when different detectors are used since each detector, not necessarily involved in the measurement of a particular element of the matrix, measures different irradiance variations due to the optical elements in front of it. Thus, in this work we have chosen to present the Mueller matrices just as obtained after calibration.

As part of the analysis of the experimental results, we calculated the errors propagation in the vectorial polarimeter by associating to the experimental data an error equal to the standard deviation of the 30 averaged measurements. Fig. 4.7 shows the absolute error in each element of the Mueller matrix of free space. These errors are given in the range $[0, 0.1]$, i.e. the maximum variation is 10% of the maximum experimental value for m_{11}, and have an almost radial distribution similar to the irradiance variations of the incident beam. From the figure, it is apparent that the maxima errors occur at the rim of the beam. Note that the high frequency fringes at $-45°$ are also present. Thus, since the exit pupil of the collector lens only covers a fraction of the centre, the effect of these errors is negligible. It is interesting that the largest errors occur in the elements of the Mueller matrix associated to the measurements with the $+45°$ polariser. This is an indication that the measurements with the largest variations are taken with camera CCD3, which is consistent with

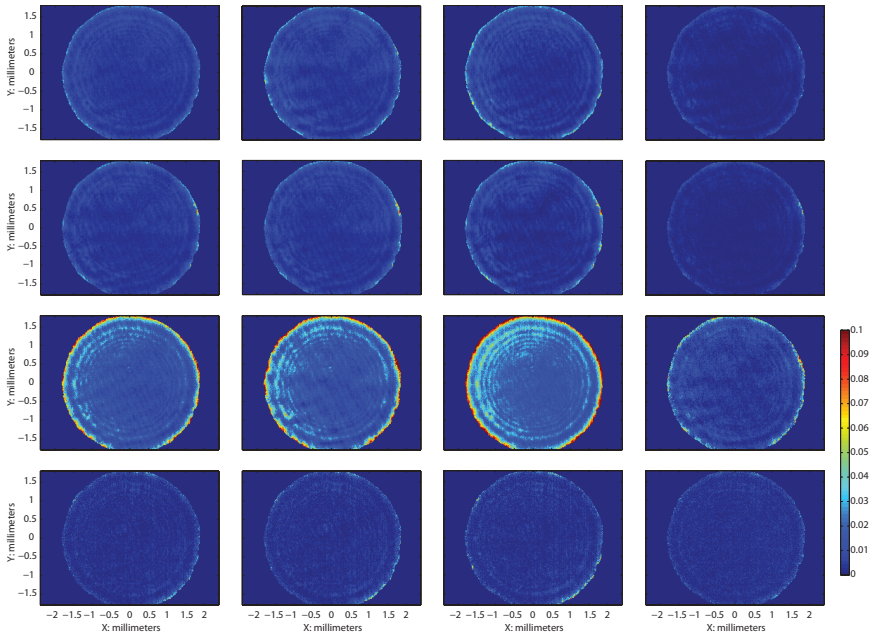

Figure 4.7: Experimental absolute errors in the aperture of the beam for each element of the scattering-angle-resolved Mueller matrix of free space, $\mathbf{B_0}$. The maximum in the scale corresponds to 10% of the maximum value measured for m_{11}. The area covered by the exit pupil of the collector lens is in the central part of the aperture. A zoom in to this region does not reveal further details of the distribution.

the variations discussed above. Similar errors where obtained for the other calibration samples and, thus, are not presented here.

Fig. 4.8 is a matrix with a histogram of the pixel value distribution, within the aperture of the beam, for $\mathbf{B_0}$. The mean and standard deviation of the pixel value distribution, for the Mueller matrix of each calibration sample, are shown in Table 4.1.

For the sake of comparison, we calculated the corresponding theoretical Mueller matrices fitted with the retardance, transmission coefficients, and orientation angles obtained from the average of the values calculated with the DP-ECM within the aperture of the beam. These results are shown in Table 4.2.

The agreement between the theoretical and experimental values is below the standard deviation for almost every element of the matrices; the only exceptions are m_{24} and m_{32} in $\mathbf{B_0}$. Thus, to a good extent, the experimentally determined Mueller matrices correspond with their theoretical counterparts.

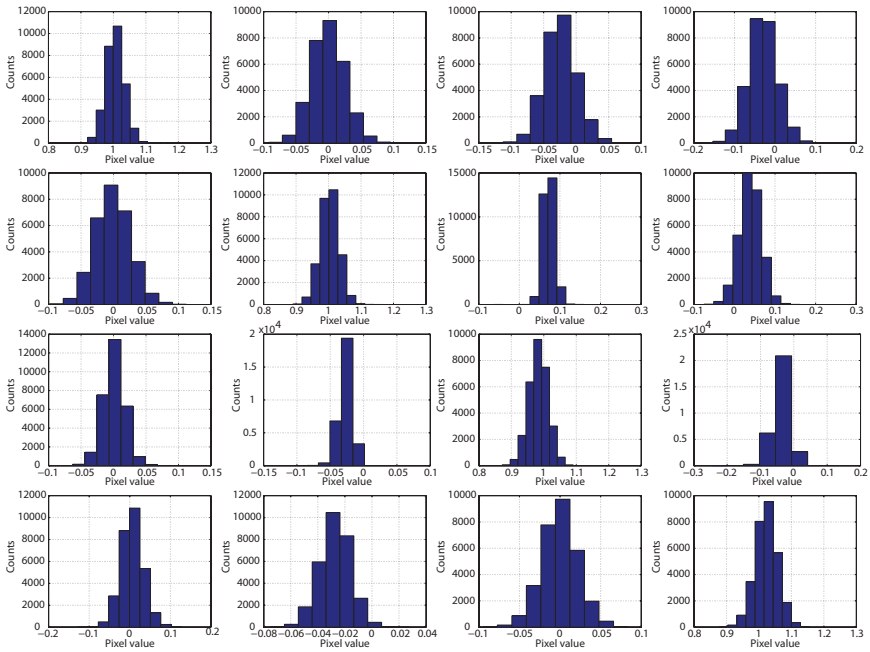

Figure 4.8: Histogram of the pixel value distribution, within the aperture of the beam, for $\mathbf{B_0}$. The mean and standard deviation of this distribution are shown in Table 4.1.

Table 4.1: Mean and standard deviation of the pixel value distribution, within the aperture of the beam, for the Mueller matrix of each calibration sample.

Sample	Mean **M**	Standard deviation
$\mathbf{B_0}$	$\begin{pmatrix} 1.0056 & -0.0011 & 0.0008 & 0.0061 \\ -0.0005 & 1.0031 & -0.0270 & -0.0272 \\ -0.0240 & 0.0726 & 0.9838 & -0.0003 \\ -0.0296 & 0.0389 & -0.0375 & 1.0229 \end{pmatrix}$	$\begin{pmatrix} 0.0280 & 0.0270 & 0.0165 & 0.0277 \\ 0.0256 & 0.0286 & 0.0098 & 0.0114 \\ 0.0246 & 0.0135 & 0.0296 & 0.0222 \\ 0.0355 & 0.0269 & 0.0240 & 0.0343 \end{pmatrix}$
$\mathbf{B_1}$	$\begin{pmatrix} 0.4374 & 0.4431 & -0.0006 & 0.0009 \\ 0.4310 & 0.4372 & -0.0004 & 0.0009 \\ -0.0012 & -0.0010 & -0.0007 & -0.0009 \\ 0.0022 & 0.0029 & 0.0012 & -0.0011 \end{pmatrix}$	$\begin{pmatrix} 0.0316 & 0.0317 & 0.0275 & 0.0360 \\ 0.0325 & 0.0316 & 0.0267 & 0.0293 \\ 0.0387 & 0.0392 & 0.0071 & 0.0072 \\ 0.0615 & 0.0627 & 0.0168 & 0.0154 \end{pmatrix}$
$\mathbf{B_2}$	$\begin{pmatrix} 0.4276 & -0.4315 & 0.0029 & 0.0062 \\ -0.4213 & 0.4249 & -0.0029 & -0.0063 \\ -0.0074 & 0.0072 & 0.0046 & -0.0007 \\ -0.0184 & 0.0168 & 0.0022 & -0.0007 \end{pmatrix}$	$\begin{pmatrix} 0.0522 & 0.0455 & 0.0558 & 0.0268 \\ 0.0549 & 0.0479 & 0.0545 & 0.0263 \\ 0.0318 & 0.0524 & 0.0100 & 0.0069 \\ 0.0529 & 0.0528 & 0.0157 & 0.0117 \end{pmatrix}$
$\mathbf{B_3}$	$\begin{pmatrix} 1.0278 & -0.0128 & -0.0056 & -0.0110 \\ 0.0192 & 0.2961 & 0.4254 & 0.8939 \\ 0.0040 & 0.4603 & 0.7579 & -0.4858 \\ 0.0255 & -0.8482 & 0.5860 & 0.0131 \end{pmatrix}$	$\begin{pmatrix} 0.0889 & 0.0297 & 0.0388 & 0.0344 \\ 0.0532 & 0.0776 & 0.0523 & 0.0701 \\ 0.0807 & 0.0578 & 0.0641 & 0.0807 \\ 0.0542 & 0.0666 & 0.0880 & 0.0639 \end{pmatrix}$

Since the specimens that the vectorial polarimeter is intended to analyse are well below the diffraction limit, it is convenient to have an extra aid to localize the region of interest in the specimen; the confocal PSA was included in the experimental setup to help in this task. However, the calibration of the confocal PSA is tricky, as discussed by Lara in [33], and the pinhole plays a key role in this process. In Lara's work, the calibration of the system was finally done without the confocal pinhole to avoid problems in the calibration. In the vectorial polarimeter the confocal pinhole is part of the spatial filter for the incident light, making unpractical to remove it for calibration. As a consequence, the calibration of the confocal PSA yield results in disagreement with the theoretical Mueller matrices of the calibration samples. Nevertheless, getting correct polarimetric measurements with the confocal PSA is not paramount in the vectorial polarimeter since these measurements are only used as an aid to locate the feature of interest. Thus, excluding the calibration of the confocal PSA from this work does not affect the results to be presented in the next chapter.

Table 4.2: Fitted theoretical Mueller matrix of each calibration sample with its corresponding parameters.

Sample	Theoretical **MM**
$\mathbf{B_0}$ $\tau = 1$	$\begin{pmatrix} 1.0000 & 0.0000 & 0.0000 & 0.0000 \\ 0.0000 & 1.0000 & 0.0000 & 0.0000 \\ 0.0000 & 0.0000 & 1.0000 & 0.0000 \\ 0.0000 & 0.0000 & 0.0000 & 1.0000 \end{pmatrix}$
$\mathbf{B_1}$ $\tau = 0.8658$ $\theta = 0.0002°$	$\begin{pmatrix} 0.4329 & 0.4329 & 0.0000 & 0.0000 \\ 0.4329 & 0.4329 & 0.0000 & 0.0000 \\ 0.0000 & 0.0000 & 0.0000 & 0.0000 \\ 0.0000 & 0.0000 & 0.0000 & 0.0000 \end{pmatrix}$
$\mathbf{B_2}$ $\tau = 0.8530$ $\theta = 90.8574°$	$\begin{pmatrix} 0.4265 & -0.4263 & -0.0128 & 0.0000 \\ -0.4263 & 0.4261 & 0.0128 & 0.0000 \\ -0.0128 & 0.0128 & 0.0003 & 0.0000 \\ 0.0000 & 0.0000 & 0.0000 & 0.0000 \end{pmatrix}$
$\mathbf{B_3}$ $\tau = 1.0280$ $\theta = 29.6550°$ $\Delta = -1.5236$ $\Psi = 0.7652$	$\begin{pmatrix} 1.0280 & 0.0000 & 0.0000 & 0.0000 \\ 0.0000 & 0.3037 & 0.4299 & 0.8830 \\ 0.0000 & 0.4299 & 0.7728 & -0.5241 \\ 0.0000 & -0.8830 & 0.5241 & 0.0485 \end{pmatrix}$

4.3 Characterisation of the objective

The characterisation of the objective is important to obtain reliable measurements of the Mueller matrix with the vectorial polarimeter. As mentioned in the previous section, it was not possible to include the objective during the calibration with the DP-ECM due to practical limitations. Instead, we used a spherical reference surface to asses the polarisation artefacts introduced by the objective. The method used in this assessment is described in this section.

When the focus of the objective coincides with the centre of curvature of the spherical reference surface, the polarisation state of the light reflected by the surface will be the same, except for a constant phase resulting from the Fresnel reflection coefficients for normal incidence on the air-glass interface, as that of the incident light. That is, the polarisation

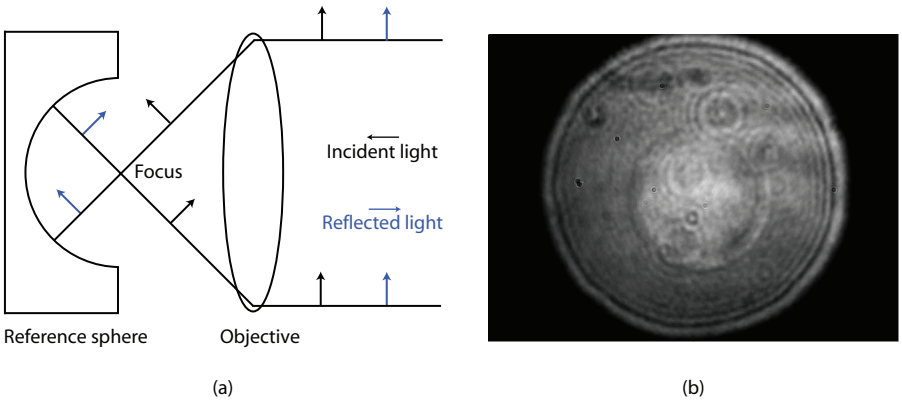

Figure 4.9: (a) Diagram of the method used to characterise the polarisation properties of the microscope objective. The electric field of the incident and reflected light is represented by the black and blue arrows, respectively. (b) Interferogram (centre of the image) for the reference sphere aligned. Note that the exit pupil of the objective is smaller than the aperture of the incident beam.

state distribution of the reflected light across the exit pupil of the objective should be the same as the distribution of the incident light across its entrance pupil. Any change in the polarisation distribution will be directly related to artefacts introduced by the objective. Fig. 4.9a is a diagram showing the geometry of the method. The reference sphere used in the characterisation of our objective is a custom-made BK7 sphere with no coating and polished to high standards to avoid introducing extra artefacts.[3] To align the sphere we used the interference pattern generated by the superposition of the light reflected by the sphere, collimated by the objective, and the light reflected by the reference mirror M2 (see Fig. 3.1). Fig. 4.9b is a picture of the interference pattern when the reference sphere is properly aligned.

Fig. 4.10 is the Mueller matrix measured for the reference sphere. This matrix is similar to the matrix of free space with a quite homogeneous distribution. The value of the matrix coefficients is reduced, with respect to the values for $\mathbf{B_0}$ obtained without the objective, because the reflectivity of the uncoated reference sphere is lower than the reflectivity of the calibration mirror. Note that the circularly symmetric irradiance variations discussed in the previous section are also present in this matrix, confirming that they are part of the illumination.

Any non-depolarising optical element can be represented by a di-

[3]Reference sphere manufactured by IC Optical Systems Ltd.

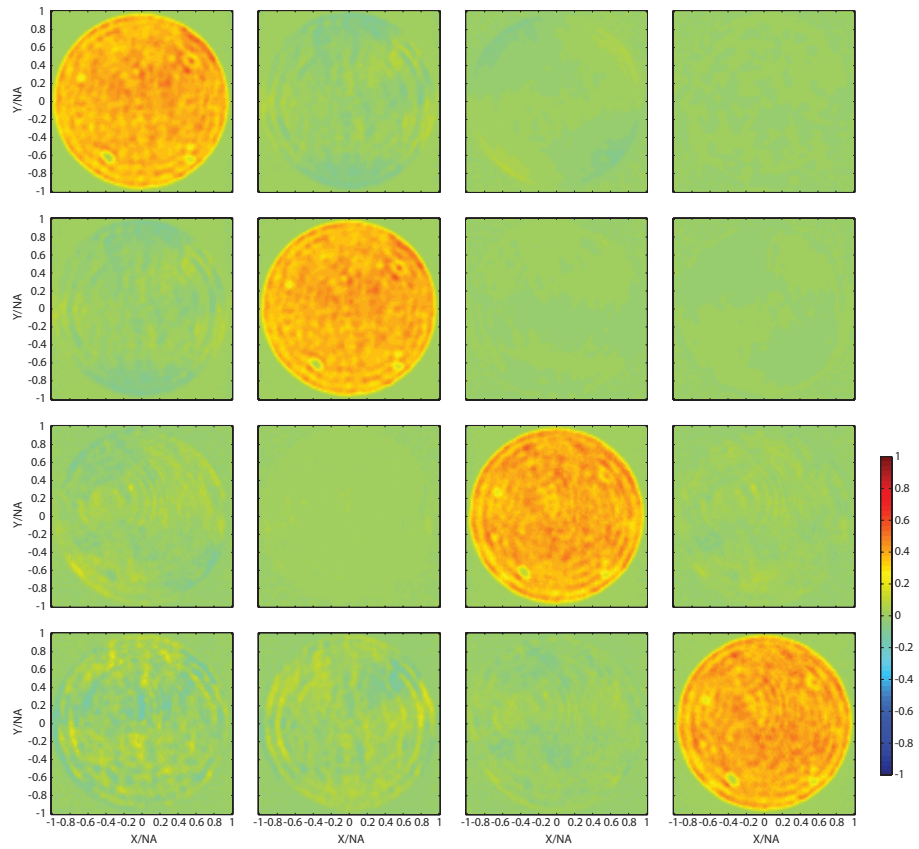

Figure 4.10: Mueller matrix of the reference sphere used to characterise the polarisation artefacts introduced by the high NA microscope objective. The spot in the lower-left corner of the pupil is due to a scratch in the surface of the sphere accidentally produced during the alignment. Note that the images correspond to a zoom-in on the region of interest, i.e., the pupil itself.

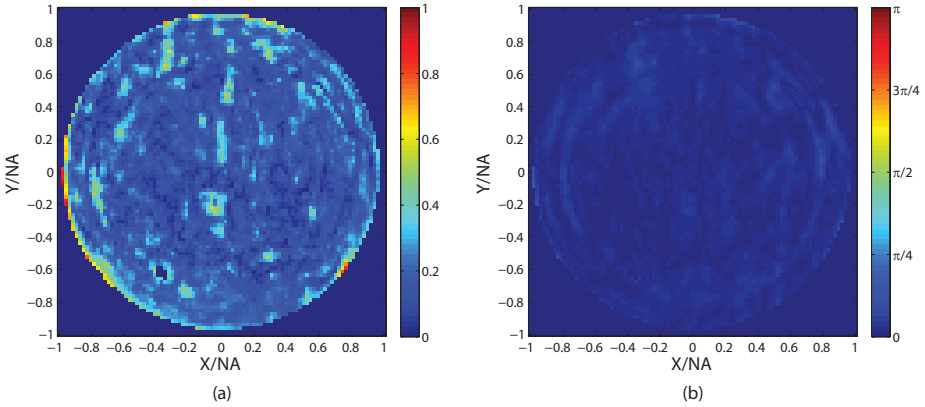

Figure 4.11: (a) Diattenuation, Ψ, and (b) retardance, Δ, of the reference sphere across the exit pupil of the objective.

attenuation, Ψ, and a retardance, Δ [26]. Therefore, it is of interest to determine Ψ and Δ for the objective. Lu-Chipman decomposition [26] is an analysis tool to obtain this kind of information from experimentally determined Mueller matrices that has become a standard in the field of Mueller matrix polarimetry. Fig. 4.11 shows the diattenuation and retardance, across the pupil of the objective, obtained from the Lu-Chipman decomposition of the experimental Mueller matrix for the reference sphere. The diattenuation distribution shows variations that do not have a well defined structure and follow the distribution of the variations in m_{11}. Thus, the diattenuation distribution in Fig. 4.11 is a consequence of the residual polarisation artefacts, after calibration, rather than a property of the objective. The retardance has a similar distribution but with variations much smaller than the variations in the diattenuation. Therefore, we conclude that the variations in the diattenuation and the retardance obtained for the reference sphere are due to errors propagated during the calibration and that the objective introduces, at a first approximation, negligible polarisation artefacts in the measurements.

Chapter 5

Experimental results

The experimental verification of the numerical results presented in Chap. 2 for a point-scatterer is presented in this chapter. However, before presenting the results for a point-scatterer —as a final test of the system— we shall present the scattering-angle-resolved Mueller matrix of a flat mirror. This kind of measurement, with flat surfaces, has been reported by De Martino *et al.* [59] and Ben Hatit *et al.* [58] as a calibration method for a high NA objective in a system built to measure critical dimensions in diffraction gratings.

The measurements presented by De Martino *et al.* and Ben Hatit *et al.* are based on the use of a high NA objective lens as a means to measure, simultaneously, a large range of scattering-angles. Therefore, their results show the kind of distributions for the elements of the Mueller matrix that can be expected in the exit pupil of a high NA lens for a flat surface specimen.

5.1 Scattering-angle-resolved Mueller matrix of a flat mirror

The flat mirror used in these measurements is a Newport Broadband SuperMirror.[1] The alignment of the mirror, with respect to the incident beam, was done without the microscope objective. The method used is the same as the one used for the alignment of the auxiliary mirror during the calibration of the system (see Chap. 4). That is, the interference pattern between the flat mirror and the reference beam reflected by M2 was used to adjust the tilt of the flat mirror and make its surface perpen-

[1] Newport dielectric Broadband SuperMirror model 10CM00SB.1.

dicular to the incident beam. Then, the microscope objective was placed in its position and the mirror was brought into focus.

Two different methods were used to determine if the mirror was in focus. In the first method, the image of the exit pupil in one of the CCD cameras was used to assess the position of the mirror. As the mirror approached the position of the focus, a light spot appeared at the center of the pupil and increased its size until it filled completely the exit pupil of the objective. This was an indication that the mirror was in focus or, at least, very close to it. When the mirror continued moving closer to the objective, the amount of light in the exit pupil reduced until it disappeared. This, of course, indicated that the mirror had surpassed the focal plane for a distance larger than half the depth of focus.

In the second method, the interference between the reference beam, reflected from M2, and the light collimated by the objective was used to determine the position of the mirror. This method is similar to the method used for the alignment without the objective. The difference is that, in this case, what varies is the distance between the flat mirror and the objective rather than the tilt of the mirror.

The experimental results obtained for the flat mirror are presented in Fig. 5.1. These results have symmetries similar to those reported in [59] and [58] for flat semiconductor surfaces. The differences between the results are due to the different physical properties of the samples. Note that the results in Fig 5.1 are given as obtained directly from the experiment. Thus, they are presented in the global XY coordinate system. Although this might seem to be a natural choice, at a first glance, this is not the case as can be seen from the two-fold and four-fold symmetries present in many of the Mueller matrix elements. This kind of symmetries are not expected for the Mueller matrix of a homogeneous sample, as it was pointed out by Ben Hatit *et al.* in [58]. Because of the nature of the reflection on the flat mirror, it is more appropriate to present the results in a local PS coordinate system, where P and S are the directions parallel and perpendicular, respectively, to the plane of incidence.[2]

The definition of both coordinate systems is shown in Fig. 5.2, where the exit pupil is represented by the green circles. The transformation of the experimental results from the XY coordinate system to the PS coordinate system is shown in Fig. 5.3. After the transformation, the two-fold and four-fold symmetries present in many of the Mueller matrix elements disappeared. The transformed matrix is more homogeneous,

[2]The transformation of the coordinate system was also proposed by Ben Hatit *et al.* in [58].

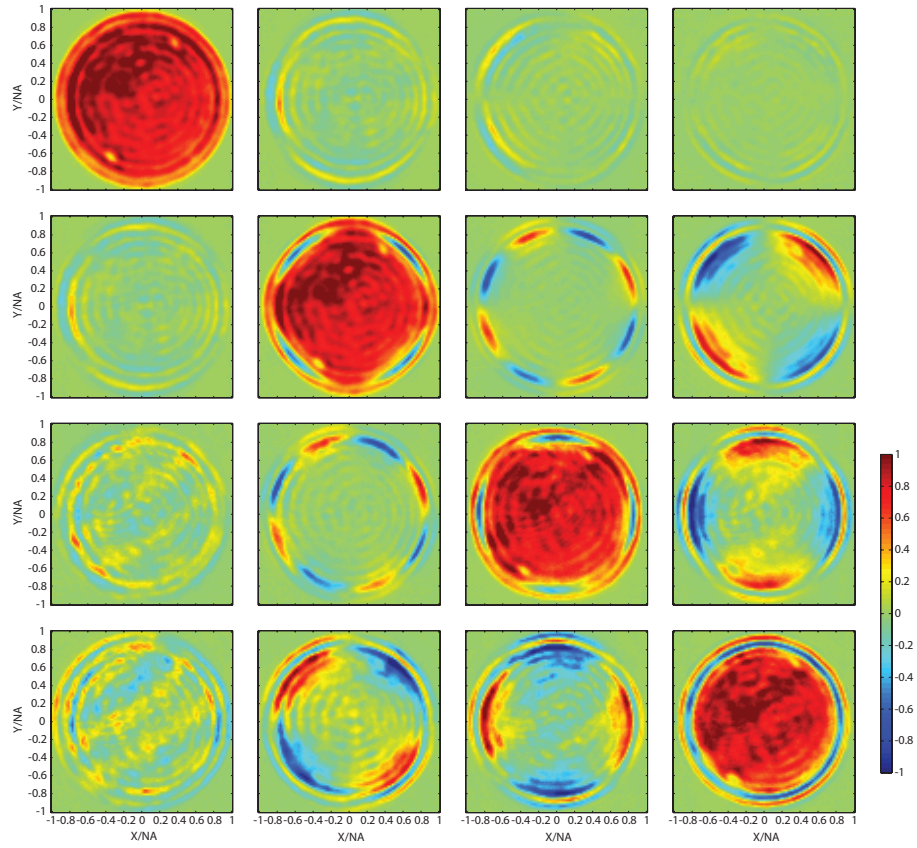

Figure 5.1: Experimentally determined Mueller matrix in the exit pupil of the collector lens for the flat mirror. The results are presented in the global XY coordinate system as obtained from the experiment.

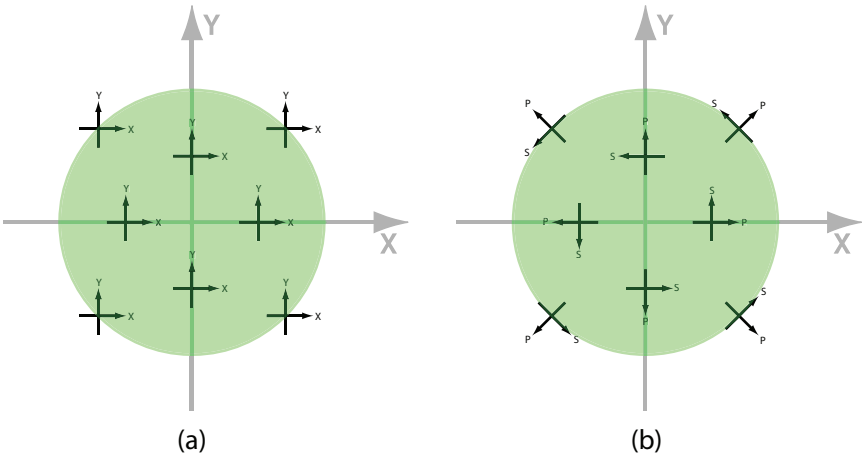

Figure 5.2: Definition of the (a) global XY and (b) local PS coordinate systems in the exit pupil of the collector lens.

despite the variations in irradiance discussed in Chap. 4, as it is expected for a homogeneous sample.

The form of the Mueller matrix in Fig. 5.3 reveals a radial symmetry that indicates that the mirror behaves like a linear retarder with fast axis perpendicular to the plane of incidence and retardance dependent on the angle of incidence. For instance, in the center of the images, which correspond to small angles of incidence, the Mueller matrix corresponds to that of a perfect mirror.[3] However, as the angle of incidence is increased, the retardance, as can be seen in elements m_{34} and m_{43}, increases slowly to π, then it drops quickly to zero and finally increases quickly until the rim of the pupil. A Lu-Chipman decomposition of the matrix, which is independent of the chosen coordinate system, can be used to better appreciate the retardance distribution. Figs. 5.4a and 5.4b are the diattenuation and retardance distributions, respectively, in the exit pupil of the collector lens for the flat mirror. While the retardance follows the behaviour described above, the diattenuation exhibits a rather noisy distribution with no clear information about the properties of the sample. The sudden increase in the diattenuation observed at the rim of the pupil is an artefact due to a quick drop in irradiance within this region; this is an indication that the mirror was not exactly in focus.

During the measurements with the flat mirror, the control on the position of the mirror with respect to the objective was limited by the

[3]Recall that the calibration matrices change the Mueller matrix of a mirror by the matrix of free space.

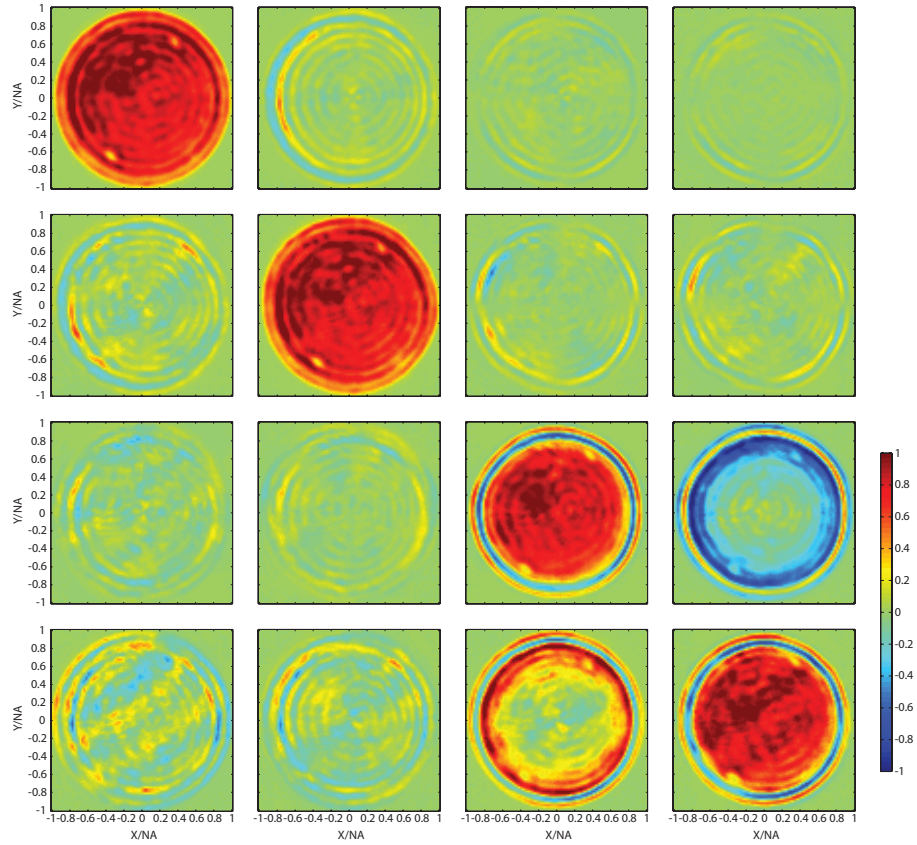

Figure 5.3: Experimentally determined Mueller matrix in the exit pupil of the collector lens for the flat mirror. The results are presented in the local PS coordinate system as obtained from the transformation of the experimental results in Fig. 5.1.

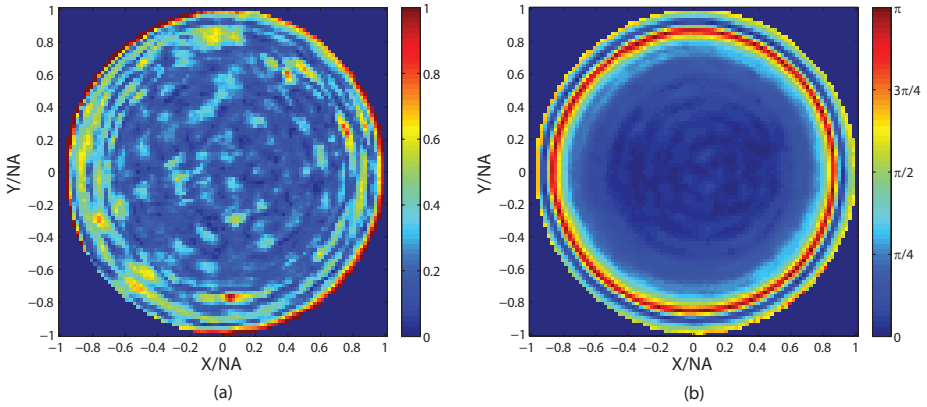

Figure 5.4: (a) Diattenuation and (b) retardance of the flat mirror across the exit pupil of the objective.

minimum incremental motion and repeatability of the translation stages used.[4] The nominal depth of focus of the MPLAPO 100x Olympus objective used in these measurements is 0.3μm whereas the minimum incremental motion of the translation stages is 0.050μm with a bidirectional repeatability of 2μm. Thus, since a scanning along the optical axis had to be done to determine if the objective was in or out of focus, the bidirectional repeatability of the linear stages limited the performance of the vectorial polarimeter.

5.2 Scattering-angle-resolved Stokes parameters of a point-scatterer

The limitation in the performance of the vectorial polarimeter described in the previous section was acceptable for the measurements with the flat mirror. However, it constitutes a real drawback for the measurements intended to verify the numerical results for a point-scatterer. Since this is important to obtain an experimental proof of concept of the *vectorial polarimetry* method, a piezo-positioning system —or piezo-stage—, with a nominal resolution of 2nm in closed-loop, was included in the experimental setup to improve the control over the position of the sample.[5]

A microscope slide with 80nm diameter gold nano-spheres was used as a sample; each gold nano-sphere was considered as a point-scatterer.[6] The main assumption in the numerical analysis of the field scattered by a point-scatterer is that the point-scatterer behaves like an electric dipole with dipole moment proportional to the incident field. This condition is fulfilled by a metallic sphere as long as the radius of the sphere is much smaller than the wavelength [54]. The gold nano-spheres used in this work satisfy this condition. Besides, this is consistent with a previous work where the same kind of nano-spheres were used as point-scatterers at visible wavelengths [60].

Because of practical limitations in the system, further modifications to the experimental setup were necessary for the measurements with the gold nano-spheres. Among these limitations is the correct positioning of the piezo-stage.

[4] A three-axis array formed by three Newport miniature linear stages model MFA-CC.

[5] The piezo-positioning system is a three-axis Tritor100SG manufactured by PiezoSystem Jena.

[6] The slides with gold nano-spheres were prepared and donated by Klas Lindfors from the Helsinki University of Technology.

Piezo-stages are made of ceramic materials that are very strong but brittle when mechanical strain forces are applied. Thus, it is important to position the piezo-stage in the right orientation and with a load within the limits prescribed by the manufacturer. To place the piezo-stage in the correct position it was necessary to modify the system to make the microscope objective face down to the optical table. Therefore, an extra mirror at 45° with respect to the incident beam, M5, was introduce before the objective to reflect the light downwards (see Fig. 5.5).

The introduction of the extra mirror increased the distance between the exit pupil of the objective and the first lens in the relay optical system used to image the pupil in the CCD cameras. Thus, the two lenses on the first relay telescope, L3 and L4 in Fig. 3.1, were replaced by a couple of lenses, L3' and L4', respectively, with a larger focal length.[7] The new relay telescope has a transverse magnification slightly larger than the original one ($M_T = 0.57$ as compared to the original $M_T = 0.5$). Nevertheless, the final size of the pupil image remains within the limits of the CCD detectors.

The modified system was re-calibrated to include the effects of the extra mirror and the new relay telescope in the system calibration matrices. This calibration was done in the same way as described in Chap. 4 with similar results. The actual results are not included herein for the sake of brevity and because they do not contribute further to our discussion.

Finding a gold nano-sphere by scanning the sample with the light focused by the high NA objective proved difficult. To facilitate the localization of the nano-spheres, the light from laser LS (see Fig. 3.1) was blocked and an auxiliary laser beam, ALS, was included.[8] The auxiliary laser impinged on the microscope slide from one side rather than from the top or the bottom. This arrangement is similar to darkfield illumination in the sense that the light collected by the objective is light purely scattered by the sample, i.e. does not include neither transmitted nor specularly reflected light. Fig. 5.5 is a diagram of the modified system. A mirror in a flip-in mount, M6, was introduced between M3 and M4 to deviate the light towards lens L7, and form an image of the microscope slide in CCD5; this image is the same that would be obtained in a typical optical microscope with darkfield illumination. When the flip-in mount is in the upright position, the light is deviated towards L7; when it is lying down, the light continues to form an image of the pupil in CCD1-CCD4.

[7] L3 was replaced by a G063235000 achromat and L4 by a G063213000 achromat from the Linos catalogue.

[8] ALS is a Spectra-Physics He-Ne laser model 196-1 with $\lambda = 633$nm.

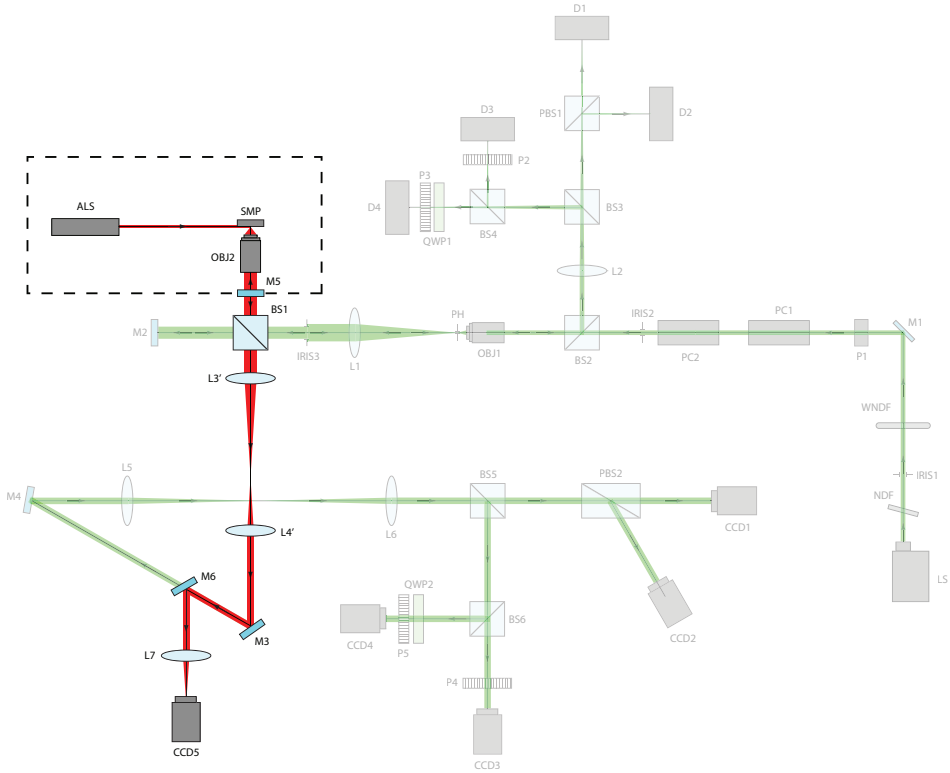

Figure 5.5: Modified setup diagram. The part of the system not used in the localization of the nano-spheres is shaded. The section within the dashed lines box is orthogonal to the plane of the image due to the reflection in M5 (the mirror at 45° included before the objective). Auxiliary laser, ALS, impinges on the side of the microscope slide. Lenses L3' and L4' are the replacements for L3 and L4, respectively, in the new first relay telescope. Mirror M6 is in a flip-in mount to deviate the beam towards L7 and form an image of the microscope slide in CCD5.

Placing the nano-sphere in the focal region of the objective using the image in CCD5 was straightforward. However, measuring the polarisation state distribution in the exit pupil for the nano-sphere was impossible due to a strong backreflection in the microscope slide that screened the light scattered by the nano-sphere. Therefore, an extra modification was required.

To reduce the backreflection on the microscope slide, the MPLAPO 100x Olympus objective was replaced by an UPLSAPO 100x oil immersion Olympus objective —of the UPlanSApo series— with NA=1.40 in $n = 1.518$ immersion oil. The refractive index matching between the immersion oil and the microscope slide reduced the backreflection sufficiently to obtain usable information from the light scattered by the nano-sphere.

It was impractical to fill the reference sphere used to calibrate the MPLAPO objective with immersion oil to measure the Mueller matrix of the UPLSAPO immersion objective. Thus, the assessment of the polarisation artefacts introduced by the UPLSAPO objective was not directly done. The information provided by the manufacturer states that the polarisation properties of both objectives are within the same specifications. Therefore, since the Mueller matrix of the MPLAPO objective does not show any strong polarisation artefact, the effect of the UPLSAPO objective on the polarisation measurements was assumed to be negligible as well.

With the dry objective, the microscope slide did not require any further preparation; the sample was just placed over the piezo-positioning system and brought to focus. However, for the oil immersion objective we put a drop of immersion oil over the slide and covered it with a cover glass for protection. Fig. 5.6a is a diagram of the prepared sample illuminated by the auxiliary laser, ALS, in position to be analysed with the oil immersion objective. Fig. 5.6b is the corresponding image obtained with CCD5.

The image in CCD5 was useful to position the gold nano-sphere in the focal region of the high NA objective. However, this image was not sufficient to place the nano-sphere exactly at the focus. A fine adjustment on the transversal position of the nano-sphere was done by maximizing the irradiance in the CCD2 image of the pupil —i.e. the component horizontally polarised of the scattered field— for incident light linearly polarised in the horizontal direction.[9]

[9]Note that other corresponding combinations polariser-analiser might have been used for the fine adjustment as well; the linear horizontal case was chosen arbitrarily.

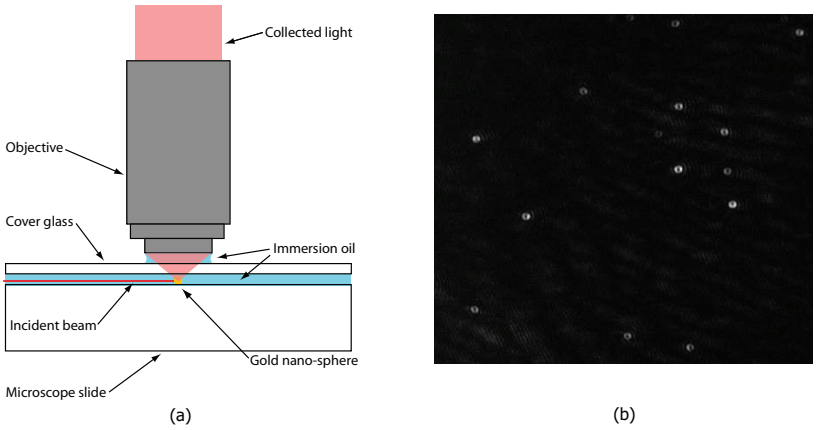

Figure 5.6: (a) Diagram showing the preparation of the sample for analysis with the oil immersion objective. The sample is being illuminated by the auxiliary laser, ALS. (b) Corresponding image of the nano-spheres as obtained by CCD5 with the flip-in mount mirror in the upright position.

The fine adjustment on the position of the nano-sphere along the optical axis was done by verifying that the pupil was completely filled with light, just as described in §5.1. Afterwards, also as described in the aforementioned section, the interference pattern between the light collected by the objective and the reference beam reflected by M2 was checked.

Although the measurements performed with the vectorial polarimeter may be used to reconstruct the complete Mueller matrix of the samples, the results presented in §2.6 are limited to the pupil distribution of the Stokes parameters. Thus, we shall omit the experimental Mueller matrix of the gold nano-sphere and present the comparison between numerical and experimental results for the Stokes parameters in the exit pupil.

Fig. 5.7a shows the experimental results obtained for the *on axis* gold nano-sphere with incident light horizontally polarised. Fig. 5.7b shows the corresponding numerical results for a point-scatterer under the same oil-immersion conditions. These results are normalized with respect to the maximum S_{0x} and are similar to the numerical results presented in Fig. 2.14.[10] Despite the noise in the experimental results,

[10]The experimental results for the gold nano-sphere presented in this chapter do not correspond exactly to the numerical results presented in Chap. 2 due to the different surrounding media. The experimental results were obtained with a NA=1.40 in a medium with $n = 1.518$ whereas the numerical results in Chap. 2 were obtained for a NA=0.95 in air, $n = 1.0$. Nevertheless, since the difference in angular semi-aperture

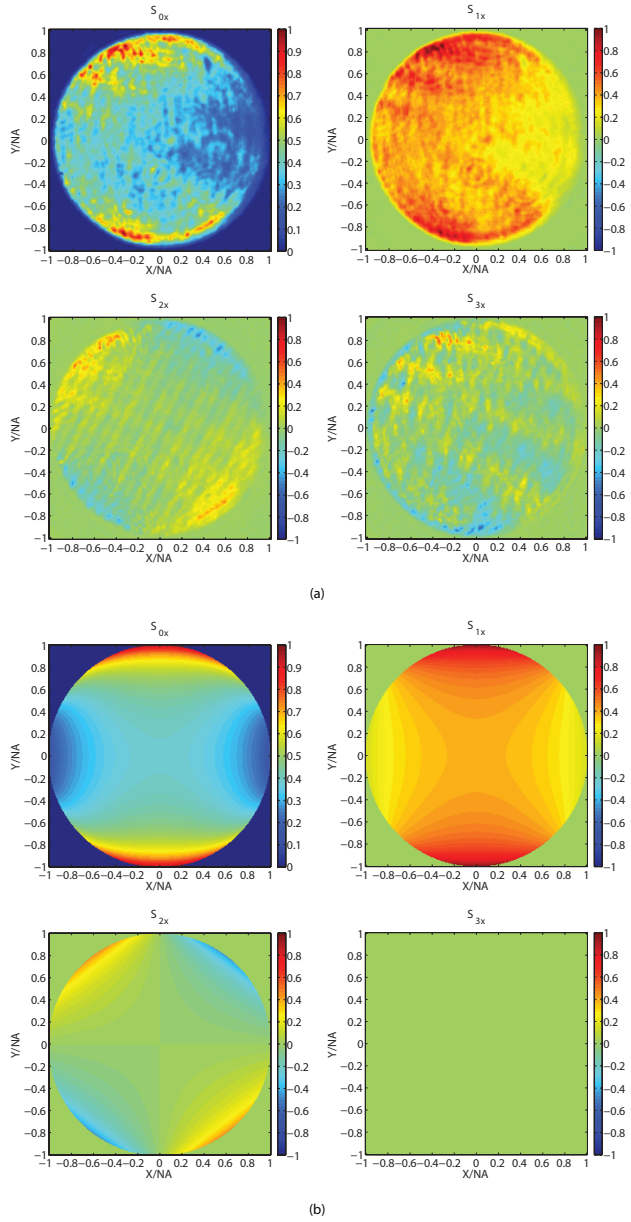

Figure 5.7: (a) Experimentally obtained Stokes parameters distribution in the exit pupil of the collector lens for an *on axis* gold nano-sphere with incident light linearly polarised in the horizontal direction. (b) Corresponding numerical results for a point-scatterer. The Stokes parameters are normalized with respect to the maximum S_{0x}.

and the asymmetry between the right and left hand sides of S_{0x} and S_{1x} not present in the numerical results, the basic structure of the polarisation state distribution is apparent and in agreement with the results presented in Fig. 5.7b. Furthermore, the noise in the experimental results is consistent with the noise in the Mueller matrix of the calibration samples (see Chap. 4). For instance, even though the noise is relatively high in S_{3x}, which according to the numerical results should be zero, the noise distribution follows the interference fringes discussed in §4.2. Thus, this distribution does not contain information about the specimen under observation but about the imperfections of our optical system.

Fig. 5.8a shows the experimental results obtained for the *on axis* gold nano-sphere for incident light circularly polarised to the left. The corresponding numerical results are shown in Fig. 5.8b. It is important to note that the numerical results are for incident light circularly polarised to the right whereas the experimental results are for incident light circularly polarised to the left. Even though these results have the opposite handedness they correspond because in the numerical results the reference coordinate system is different for incident and scattered light whereas it is the same in the experimental results; the calibration with the DP-ECM accounts for the difference. The noise in Fig. 5.8a is, again, consistent with the residual polarisation artefacts that remain after the calibration. However, once more, the basic structure of the Stokes parameters distribution in the exit pupil of the collector lens is apparent and in agreement with the numerical results.

So far, we have verified experimentally that it is possible, to a certain extent, to measure the inhomogeneous polarisation state distribution in the exit pupil of the collector lens for a point-scatterer. The next step is to verify the high sensitivity on the position of the point-scatterer, within the focal region of the objective, achieved with the analysis of the exit pupil polarisation state distribution.

Figs. 5.9a and 5.10a show the Stokes parameters distribution in the exit pupil for an *off axis* point-scatterer located in the focal plane at $x = -\lambda/3$ and $x = +\lambda/3$, respectively, with incident light linearly polarised in the horizontal direction. The corresponding numerical results are shown in Figs. 5.9b and 5.10b. Despite the noise in the measurements, the general form of the measured distributions is the same as in the numerical calculations. Furthermore, the mirror symmetry,

is only $\approx 3.81°$, the Stokes parameters pupil distributions in both cases are similar, as can be seen in Fig. 5.7b. These latter results were obtained assuming a perfect matching between the refractive indices of the immersion oil and the cover glass.

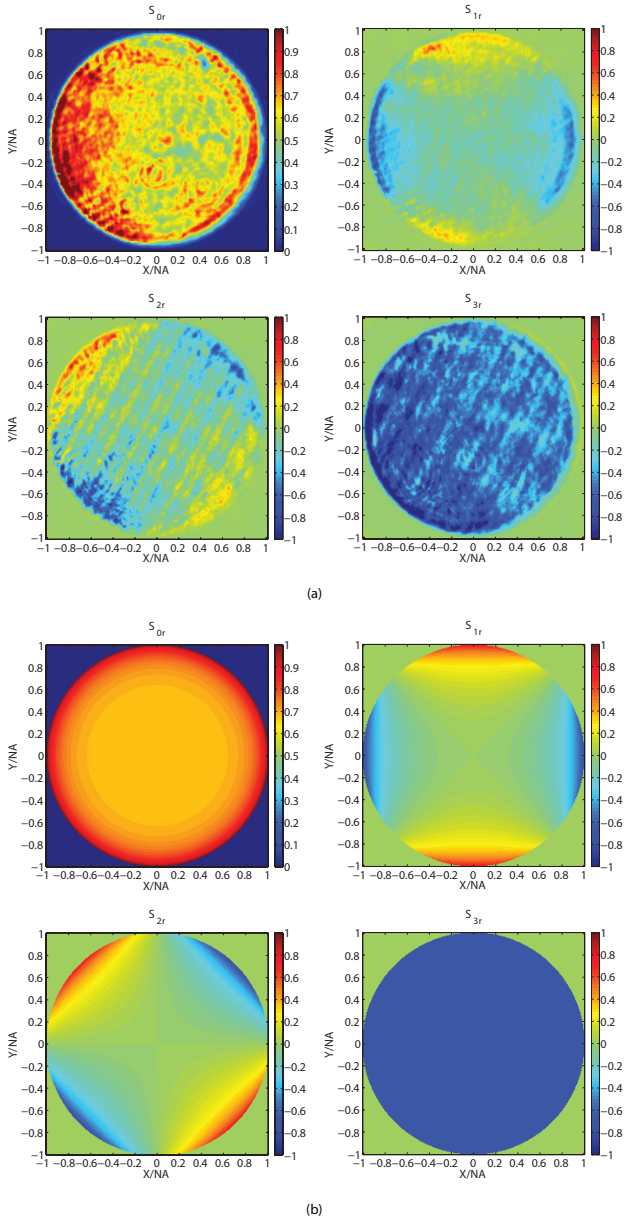

Figure 5.8: (a) Experimentally obtained Stokes parameters distribution in the exit pupil of the collector lens for an *on axis* gold nano-sphere with incident light circularly polarised to the left. (b) Corresponding numerical results for a point-scatterer. The Stokes parameters are normalized with respect to the maximum S_{0r}.

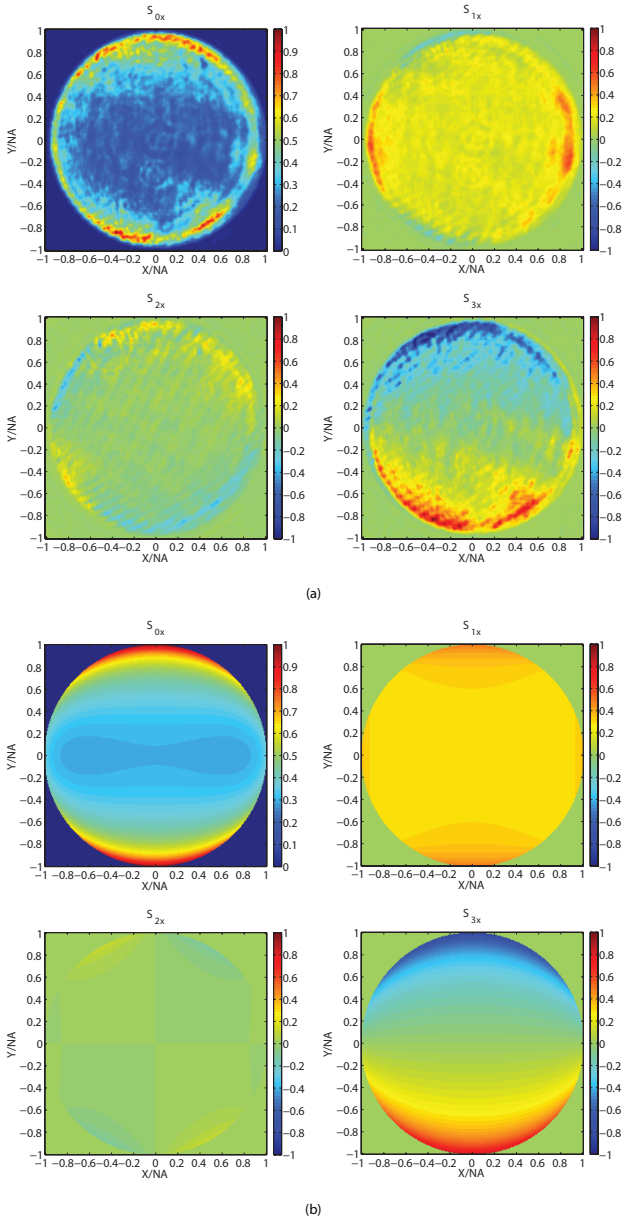

Figure 5.9: (a) Experimentally obtained Stokes parameters in the exit pupil of the collector lens for a gold nano-sphere in the focal plane at $x = -\lambda/3$ with incident light linearly polarised in the horizontal direction. (b) Corresponding numerical results for a point-scatterer. The Stokes parameters are normalized with respect to the maximum S_{0x}.

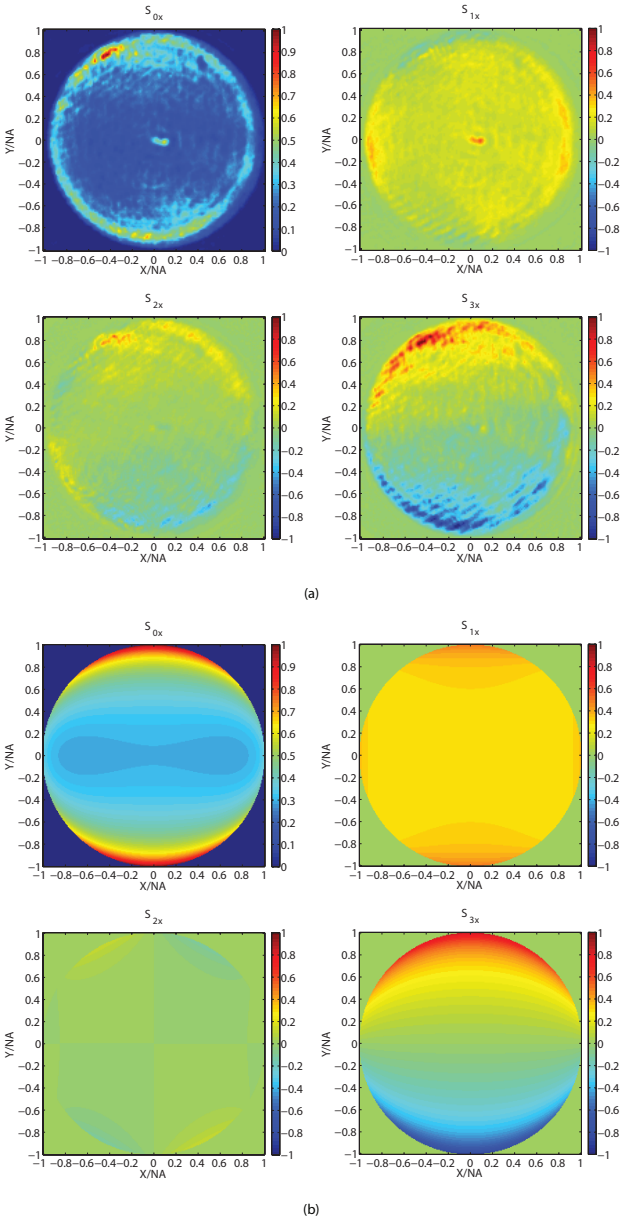

Figure 5.10: (a) Experimentally obtained Stokes parameters in the exit pupil of the collector lens for a gold nano-sphere in the focal plane at $x = +\lambda/3$ with incident light linearly polarised in the horizontal direction. (b) Corresponding numerical results for a point-scatterer. The Stokes parameters are normalized with respect to the maximum S_{0x}.

along the horizontal direction, predicted for S_{3x} between the $x = -\lambda/3$ and $x = +\lambda/3$ positions of the scatterer, is present in the experimental results. Thus, the results show that it is possible to determine if the sub-resolution scatterer has undergone a sub-resolution displacement, as well as the direction of the sub-resolution displacement, by analysing the polarisation state distribution in the exit pupil of the high NA collector lens.

As discussed in Chap. 2, and shown in the previous results, the high sensitivity on the position of the sub-resolution scatterer is limited to S_{3x} in the case of incident light linearly polarised; the other three elements exhibit essentially the same distribution independently of the direction of the displacement. It was shown in §2.6 that the use of incident light circularly polarised allows us to obtain the high sensitivity in any of the four Stokes parameters. Figs. 5.11a and 5.12a show the experimental results obtained for this case. The corresponding numerical results are shown in Figs. 5.11b and 5.12b. The agreement between numerical and experimental results is apparent, in most of the Stokes parameters, despite the noise in the measurements. The element with the worst agreement with its numerical counterpart, especially in the results for the gold nano-sphere at $x = -\lambda/3$, is S_{2r}. Thus, due to the relatively high noise level in the experimentally determined S_{2r}, no conclusive remarks, based on this element, can be done concerning the displacement of the gold nano-sphere. Nevertheless, as can be seen in Figs. 5.11 and 5.12, the direction of the sub-resolution displacement of the gold nano-sphere is encoded in the other three Stokes parameters, as predicted by the numerical calculations.

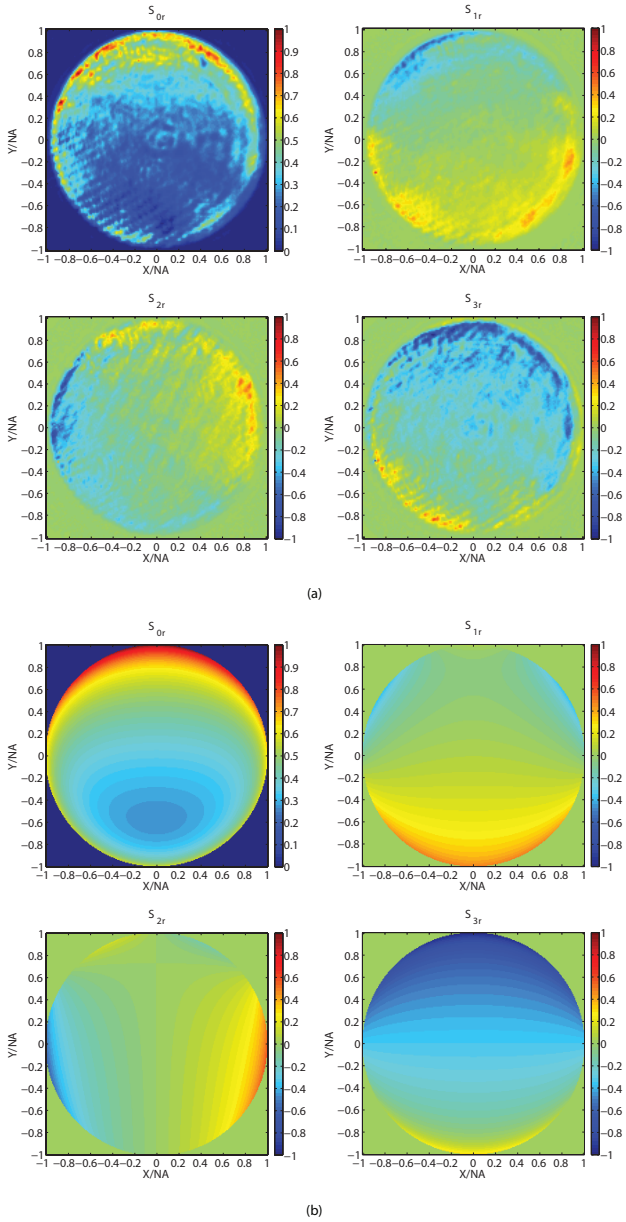

Figure 5.11: (a) Experimentally obtained Stokes parameters in the exit pupil of the collector lens for a gold nano-sphere in the focal plane at $x = -\lambda/3$ with incident light circularly polarised to the left. (b) Corresponding numerical results for a point-scatterer. The Stokes parameters are normalized with respect to the maximum S_{0r}.

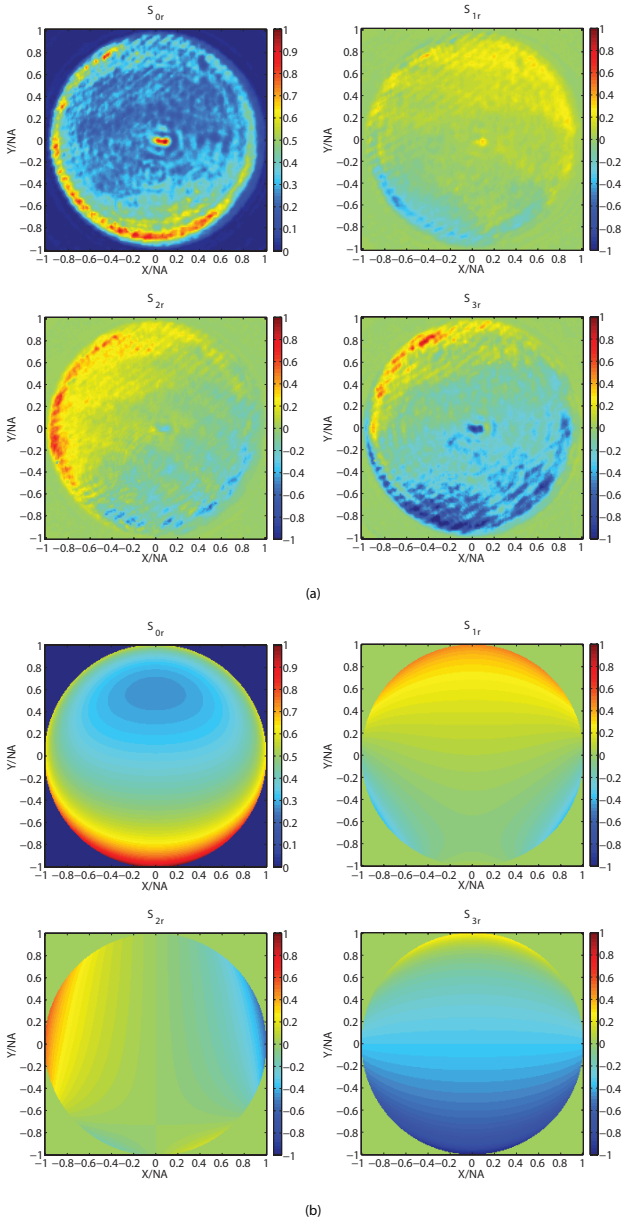

Figure 5.12: (a) Experimentally obtained Stokes parameters in the exit pupil of the collector lens for a gold nano-sphere in the focal plane at $x = +\lambda/3$ with incident light circularly polarised to the left. (b) Corresponding numerical results for a point-scatterer. The Stokes parameters are normalized with respect to the maximum S_{0r}.

Chapter 6

Conclusions

The results presented in the previous chapter constitute an experimental proof of concept of the *vectorial polarimetry* method. Even with the unavoidable experimental errors, the agreement between the numerical and the experimental results is apparent.

In this chapter, we shall give some final remarks about the results obtained and discuss possible directions for the future of this research.

6.1 Field distribution in the focal region

Although the most used method to calculate the field distribution in the focal region of a high NA objective lens is the direct integration of Debye-Wolf integrals, McCutchen's method offers a suitable alternative. The comparison between McCutchen's method and Debye-Wolf integrals presented in §2.5 shows that the field distribution in the focal region is, in both cases, essentially the same. The slight differences observed between the two methods are due to the different samplings used. An alternative method for the calculation of the field distribution in the focal region of a lens, based on the Fourier transform of a pupil function, was introduced by Leutenegger *et al.* in [61]. This method, however, is fundamentally the same as McCutchen's method and does not represent any real advantage.

One of the strengths of McCutchen's method in comparison with the direct integration of Debye-Wolf integrals, in the context of modern digital computers, is the possibility of applying an FFT algorithm to reduce the computational time. Leutenegger *et al.* discussed in their work the best way to implement their method in a digital computer to achieve maximum speed in the calculations. They even included a comparison

between their optimized implementation and a simple implementation of an FFT algorithm. Their conclusion is that, whereas the latter takes $\approx$ 1min to complete the calculations, the former only takes $\approx$ 30sec. Even though the optimized method halves the computational time, this does not represent a real advantage in applications where the calculations do not need to be done in real time.

Another appealing feature of McCutchen's method is that it is relatively easy to calculate the focused field distribution for inhomogeneous incident polarisation states; this is not the case in the direct integration of Debye-Wolf integrals. As discussed in Chap. 2, the electric field distribution in the focal region is a function of the NA of the focusing lens as well as the polarisation state of the incident light. In this work, only results for homogeneous incident polarisation states —i.e. states for which the polarisation is the same at any position within the aperture of the beam— have been presented. Using only this kind of incident distributions limits the amount of possible field distributions in the focal region; recall that the sensitivity of the *vectorial polarimetry* method depends on the electric field distribution in the focal region. Thus, by engineering the polarisation state distribution of the incident light, it is possible to tailor the field distribution in the focal region to increase the sensitivity of the method. In the laboratory, incident polarisation state engineering can be done using a tandem of spatial light modulators (SLMs), as proposed by Iglesias and Vohnsen [36]. In this case, the correct alignment between corresponding pixels of the SLMs is an important practical issue to be considered.

The engineering of the incident polarisation state, as a means to tailor the field distribution in the focal region, has been explored by several authors in the past [36, 61–63]. However, most work done in this field has only addressed the problem of finding the field distribution in the focal region for a given incident polarisation distribution. Increasing the sensitivity of our method will require the solution of the inverse problem. That is, finding the polarisation state distribution of the incident light for a prescribed field distribution in the focal region. Albeit this problem is not trivial, at least one paper tackling it can be found in the literature [64].

To conclude our discussion on inhomogeneous incident polarisation states we note that for homogeneous incident polarisation states, even though the light is focused on the sample, the polarisation state distribution of the scattered light in the exit pupil of the collector lens can be considered as a scattering-angle-resolved Mueller matrix; each pixel

in the pupil corresponds to a different pair of azimuthal and spherical scattering-angles. However, for incident light with an inhomogeneous polarisation state, the interpretation of the pupil distribution of polarisation states for the scattered light is not straightforward and will require further analysis.

6.2 Calculation of the scattered field

The calculation of the scattered field is an important part in the modelling of the performance of the *vectorial polarimetry* method. The results presented in this work, numerical and experimental, are limited to the case of a point-scatterer. This was the first example examined because the analytical solution for the field radiated by a dipole is well known [54]. Although interesting results were obtained in this simple case, it is of interest to analyse the performance of the method for sub-resolution scatterers with a more complex structure. For spherical objects, for instance, the analytical solution for the scattered field is given by Mie's theory. However, Mie's scattering solution is only given for incident monochromatic plane waves. Thus, the modelling of a focused field interacting with a spherical sample should be obtained as the scattered field resulting from the coherent superposition of Mie's scattered fields for a number of plane waves, with a given polarisation state, incident on the sample at different angles. In this case, the calculation of the focused field, using either of the methods discussed in the previous section, is unnecessary.

As discussed in Chap. 2, in the most general case the interaction of the focused field with the sample can be modelled using numerical methods. Even though several numerical methods for the solution of scattering problems are readily available, the method chosen in this work is the FDTD method; the fundamental ideas of the method were introduced in Chap. 2. In the same chapter, the NTFF transformation proposed by Török *et al.*, and used in this work, was discussed. Our implementation of the NTFF transformation was tested with excellent results but, when used in combination with the FDTD method, unreliable results were obtained. Part of the problem is in the poor performance of the ABCs implemented in the programme. However, the main source of errors is the incapability to model the boundary conditions accurately. That is, within the context of the NTFF transformation, since the integration surface has to enclose a volume containing all the sources and sinks of EM field, it is impossible to model an infinite half-space made of a PEC.

Thus, an integration surface enclosing a volume large enough, in comparison with the scatterer, can be used to approximate an infinite PEC half-space. This solution is impractical since the size of the space region modelled with the FDTD method is limited by the amount of computer resources available. An alternative to avoid this problem is modelling more realistic scatterers. This shall be done in the next stage of this research to model, for instance, a metallic scatterer over a dielectric substrate.

The use of the FDTD method was an arbitrary choice. Thus, another research direction worth exploring is the use of a different method for the calculation of the scattered field. Discrete Dipole Approximation (DDA) is a suitable alternative. An important characteristic of the DDA method is that the solution of the scattered field is given only for incident monochromatic plane waves. This is a characteristic that DDA shares with Mie's theory. Therefore, just as for Mie's theory, the total scattered field has to be obtained as the coherent superposition of the scattered field obtained for a set of plane waves, with a given polarisation state, incident at different angles on the sample. Again, as mentioned above for Mie's scattering, the use of any of the methods discussed for the calculation of the focused field is unnecessary.

6.3 Gold nano-sphere as a point-scatterer

The numerical and experimental results obtained in this work show that high sensitivity on sub-resolution displacements of a sub-resolution scatterer is achieved by analysing the polarisation state distribution in the exit pupil of a high NA collector lens. The results also show that the high sensitivity is linked to the longitudinal component of the focused field; the symmetry break between the value of that component at $x = -\lambda/3$ and $x = +\lambda/3$ is the key to differentiate between the two positions (see §2.6).

The main limitation of the high sensitivity achieved with the *vectorial polarimetry* method is that there is not an obvious way to relate the pupil polarisation state distribution with the actual value of the displacement of the point-scatterer. This means that, at the moment, there is not a quantitative way to differentiate between two polarisation distributions corresponding to two slightly different positions of the point-scatterer. As can be expected, this also limits the assessment of the minimum sensitivity achievable for a given incident polarisation state.

The role of the NA in the *vectorial polarimetry* method is paramount.

The information necessary to determine if the point-scatterer has undergone a displacement, as well as the direction of the displacement, is mostly contained in the rim of the exit pupil, revealing the importance of using a high NA collector lens. This can be further appreciated by noting that in the center of the pupil, which corresponds to low NA, the polarisation state distribution is mostly homogeneous. Thus, it is important to minimize the aberrations introduced by the imaging system at the edge of the pupil. This can be done by keeping the aperture of the pupil within the central region of the relay imaging system.

At this point it is appropriate to discuss the spot that can be observed in the center of some of the experimental results (see Figs. 5.10 and 5.12). The spot is a backreflection produced in the interface between the immersion oil and the microscope slide interface due to the finite size of the gold nano-sphere. The experimental evidence available indicates that the presence or absence of the central spot is related to a slight defocus of the gold nano-sphere. Whether the sphere is better focused when the central spot is present or not, is not clear from the experimental data.

Even though the calibration of the vectorial polarimeter with the DP-ECM reduced the polarisation artefacts introduced by the elements in the setup, residual artefacts can be observed in the experimental data. These artefacts represent a drawback in the performance of the vectorial polarimeter. For instance, the effect of the irradiance variations due to the interference fringes is one of the most important limitations of the system. The high frequency fringes, as discussed in Chap. 4, have their origin in the transmission properties of the dichroic polariser at 45° in front of CCD3. The low frequency fringes come from parasite reflections in the glass cover attached to the CCD detectors. To get rid of the high frequency fringes, the 45° dichroic polariser may be substituted with a linear crystal polariser, like the Glan-Taylor polariser in the experimental setup. The low frequency fringes may be reduced by using CCD cameras with no glass cover attached to the CCD detector or by using a single CCD camera with a sequential PSA. In the latter case, the experimental results may be normalized, pixel by pixel, with respect to m_{11} to remove the irradiance variations and keep only the polarisation distributions, just as described in [59] and [58].

An alternative to reduce the effects of the interference fringes in the measurements with the vectorial polarimeter is to change the highly temporally and spatially coherent laser source in the vectorial polarimeter by a source with good spatial coherence but reduced temporal coherence. Such a source might be, for instance, a superluminescent diode.

Finally, it is possible to change the detection scheme to achieve coherent detection. In this case, a reference light beam can be use to interfere with the image of the exit pupil of the collector lens in the plane of the detectors. From the analysis of the interference pattern it would be possible to retrieve information about a sub-resolution specimen.

6.4 Future work

A suitable quantitative method to relate the polarisation state distribution in the exit pupil with the actual displacement of the point-scatterer shall be developed as part of the future of this project. This may be done with an statistical analysis of the pupil distributions together with the definition of an appropriate metric and a threshold.

Since the results presented in this work are limited to the case of a point-scatterer, the range of applications in which they could be useful is extremely limited. A possible application of the results is in material inspection; this possibility is currently being explored in collaboration with Shimadzu Corporation, Japan. However, to increase the range of possible applications of the method, in the next stage of this research we shall model and measure the pupil polarisation distribution for sub-resolution samples with a more complex structure.

Although having information about the three-dimensional field scattered by the sample is of interest *per se*, for most applications it is desirable to obtain an actual image of the specimen. The vectorial polarimeter measures the scattering-angle-resolved polarisation state distribution of the scattered field. Thus, this method can be used to retrieve the electric field components of the scattered filed and the relative phase between them. The information about the electric field can then be used as the input to solve the inverse problem and retrieve the shape of the specimen.

In the theory, the solution of the inverse problem is conditioned to the uniqueness of the far-field distribution of the scattered field for sub-resolution specimens; this is part of the analysis that shall be done in the future. In the experiment, the solution of the inverse problem is also conditioned by the accuracy of the measurements and the signal-to-noise ratio. Therefore, reconstructing an image of an unknown specimen from the data obtained with the vectorial polarimeter, via the solution of an inverse problem, is not trivial neither in the theory nor in the experiment.

The analysis presented in this work only considers aberration-free systems. Even though this is an appropriate assumption for modern high quality microscope objectives, the impact of aberrations in the per-

formance of the method shall be studied in the future. An analytical method for the calculation of the effect of aberrations in the focused field distribution of a high NA system, based on the extended Nijboer-Zernike (ENZ) representation, has been introduced by Braat *et al.* [65]. Alternatively, the effect of aberrations in the focusing system can be studied by introducing appropriate phase variations in the *generalized aperture* within the context of McCutchen's method.

Finally, the further increase in the sensitivity of the method, by engineering the incident polarisation state, is part of the issues to be addressed in the future. The experimental control of the focused field distribution shall include a couple of SLMs to engineer the incident inhomogeneous polarisation state. The number of active pixels in the SLMs will have an influence in the polarisation distributions that can be achieved. However, the numerical results reported in [36] show that a sampling of $32 \times 32 \times 32$ points in the object space is sufficient to control the field distribution in the focal region. This does not represent a problem since a sampling density of 32×32 pixels, across the aperture of the incident beam, is well below the number of active pixels in currently available SLMs.

Bibliography

[1] J. Tersoff and D. R. Hamann. Theory of the scanning tunneling microscope. *Phys. Rev. B*, 31(2):805–813, 1985.

[2] D. Sarid. *Scanning Force Microscopy*. Oxford Series in Optical Imaging Sciences. Oxford University Press, 1991.

[3] M. Born and E. Wolf. *Principles of Optics*. Cambridge University Press, 7th edition, 1999.

[4] E. Wolf. Electromagnetic diffraction in optical systems I. An integral representation of the image field. *Proc. R. Soc. London A*, 253(1274):349–357, 1959.

[5] S. Quabis, R. Dorn, M. Eberler, O. Glöckl, and G. Leuchs. Focusing light to a tighter spot. *Opt. Commun.*, 179:1–7, 2000.

[6] I. J. Cooper, M. Roy, and C. J. R. Sheppard. Focusing of pseudo-radial polarized beams. *Opt. Express*, 13(4):1066–1071, 2005.

[7] C. J. R. Sheppard and A. Choudhury. Annular pupils, radial polarization, and superresolution. *Appl. Opt.*, 43(22):4322–4327, 2004.

[8] Alexander Neumann, Yuliya Kuznetsova, and S. R. J. Brueck. Optical resolution below $\lambda/4$ using synthetic aperture microscopy and evanescent-wave illumination. *Opt. Express*, 16(25):20477–20483, 2008.

[9] Patrick C. Chaumet, Kamal Belkebir, and Anne Sentenac. Superresolution of three-dimensional optical imaging by use of evanescent waves. *Opt. Lett.*, 29(23):2740–2742, 2004.

[10] Tony Wilson and Colin Sheppard. *Theory and Practice of Scanning Optical Microscopy*. Academic Press, London, 1984.

[11] Stefan W. Hell. Far-field optical nanoscopy. *Science*, 316:1153–1158, 2007.

[12] A. F. Fercher, W. Drexler, C. K Hitzenberger, and T. Lasser. Optical coherence tomography-principles and aplications. Technical Report 66, Institute of Physics Publishing, 2003. Reports on Progress in Physics.

[13] Stefan W. Hell and Jan Wichmann. Breaking the diffraction resolution limit by stimulated emission: stimulated-emission-depletion fluorescence microscopy. *Opt. Lett.*, 19(11):780–782, 1994.

[14] V. Westphal, M. A. Lauterbach, A. Di Nicola, and S. W Hell. Dynamic far-field fluorescence nanoscopy. *New J. Phys.*, 9:435, 2007.

[15] E. Ramsay, N. Pleynet, D. Xiao, R. J. Warburton, and D. T. Reid. Two-photon optical-beam-induced current solid-immersion imaging of a silicon flip chip with a resolution of 325 nm. *Opt. Lett.*, 30(1):26–28, 2005.

[16] B. Richards and E. Wolf. Electromagnetic diffraction in optical systems. II. Structure of the image field in an aplanatic system. *Proc. R. Soc. London A*, 253(1274):358–379, 1959.

[17] K. A. Serrels, E. Ramsay, R. J. Warburton, and D. T. Reid. Nanoscale optical microscopy in the vectorial focusing regime. *Nat. Photonics*, 2(5):311–314, 2008.

[18] R. A. Chipman. Polarization analysis of optical systems. *Opt. Eng.*, 28:90–99, 1989.

[19] Dennis Goldstein. *Polarized Light*. Marcel Dekker, 2nd edition, 2003.

[20] R. M. A. Azzam and N. M. Bashara. *Ellipsometry and Polarized Light*. Elsevier, Amsterdam, 2003.

[21] Eric Compain, Stéphane Poirier, and Bernard Drevillon. General and self-consistent method for the calibration of polarization modulators, polarimeters, and Mueller-matrix ellipsometers. *Appl. Opt.*, 38(16):3490–3502, 1999.

[22] Alexander B. Kostinski, Clark R. Givens, and John M. Kwiatkowski. Constraints on Mueller matrices of polarization optics. *Appl. Opt.*, 32(9):1646–1651, 1993.

[23] C. R. Givens and A. B. Kostinski. A Simple, Necessary and Sufficient Condition on Physically Realizable Mueller Matrices. *J. Mod. Opt.*, 40(3):471–481, 1993.

[24] R. Sridhar and R. Simon. Normal Form for Mueller Matrices in Polarization Optics. *J. Mod. Opt.*, 41(10):1903–1915, 1994.

[25] E. Landi Degl'Innocenti and J. C. del Toro Iniesta. Physical significance of experimental Mueller matrices. *J. Opt. Soc. Am. A*, 15(2):533–537, 1998.

[26] Shih-Yau Lu and Russell A. Chipman. Interpretation of Mueller matrices based on polar decomposition. *J. Opt. Soc. Am. A*, 13(5):1106–1113, 1996.

[27] William S. Bickel and Wilbur M. Bailey. Stokes vectors, Mueller matrices, and polarized scattered light. *Am. J. Phys.*, 53(5):468–478, 1985.

[28] R. M. A. Azzam. Photopolarimeter using two modulated optical rotators. *Opt. Lett.*, 1(5):181–183, 1977.

[29] R. W. Collins and Joohyun Koh. Dual rotating-compensator multichannel ellipsometer: instrument design for real-time Mueller matrix spectroscopy of surfaces and films. *J. Opt. Soc. Am. A*, 16(8):1997–2006, 1999.

[30] Juan M. Bueno and Pablo Artal. Double-pass imaging polarimetry in the human eye. *Opt. Lett.*, 24(1):64–66, 1999.

[31] G. E. Jellison Jr. and F. A. Modine. Two-modulator generalized ellipsometry: experiment and calibration. *Appl. Opt.*, 36(31):8184–8189, 1997.

[32] F. Delplancke. Automated high-speed Mueller matrix scatterometer. *Appl. Opt.*, 36(22):5388–5395, 1997.

[33] David Lara-Saucedo. *Three-dimensional Complete Polarisation Sensitive Imaging using a Confocal Mueller Matrix Polarimeter*. PhD thesis, Imperial College, London, 2005.

[34] A. De Martino, E. García-Caurel, B. Laude, and B. Drévillon. General methods for optimized design and calibration of Mueller polarimeters. *Thin Solid Films*, 455-456:112–119, 2004.

[35] J. Ellis and A. Dogariu. Optical polarimetry of random fields. *Phys. Rev. Lett.*, 95(20):203905, 2005.

[36] Ignacio Iglesias and Brian Vohnsen. Polarization structuring for focal volume shaping in high-resolution microscopy. *Opt. Commun.*, 271:40–47, 2007.

[37] P. Török, P. Varga, Z. Laczik, and G. R. Booker. Electromagnetic diffraction of light focused through a planar interface between materials of mismatched refractive indices: an integral representation. *J. Opt. Soc. Am. A*, 12(2):325–332, 1995.

[38] P. Török, P. Varga, and G. R. Booker. Electromagnetic diffraction of light focused through a planar interface between materials of mismatched refractive indices: structure of the electromagnetic field. I. *J. Opt. Soc. Am. A*, 12(10):2136–2144, 1995.

[39] P. Török, P. Varga, and G. Németh. Analytical solution of the diffraction integrals and interpretation of wave-front distortion when light is focused through a planar interface between materials of mismatched refractive indices. *J. Opt. Soc. Am. A*, 12(12):2660–2671, 1995.

[40] S. S. Sherif and P. Török. Eigenfunction representation of the integrals of the Debye-Wolf diffraction formula. *J. Mod. Opt.*, 52(6):857–876, 2005.

[41] Sherif S. Sherif, Matthew R. Foreman, and Peter Török. Eigenfunction expansion of the electric fields in the focal region of a high numerical aperture focusing system. *Opt. Express*, 16(5):3397–3407, 2008.

[42] T. Wilson, R. Juškaitis, and P. Higdon. The imaging of dielectric point scatterers in conventional and confocal polarization microscopes. *Opt. Commun.*, 141:298–313, 1997.

[43] A. Taflove and S. C. Hagness. *Computational Electrodynamics: The Finite-Difference Time-Domain Method*. Artech House, 3th edition, 2005.

[44] Karl S. Kunz and Raymond J. Luebbers. *The Finite Difference Time Domain Method for Electromagnetics*. CRC Press, 1993.

[45] W. A. Challener, I. K. Sendur, and C. Peng. Scattered field formulation of finite difference time domain for a focused light beam in dense media with lossy materials. *Opt. Express*, 11(23):3160–3170, 2003.

[46] Kyongsik Choi, James W. M. Chon, Min Gu, and Byoungho Lee. Characterization of a subwavelength-scale 3D void structure using the FDTD-based confocal laser scanning microscopic image mapping technique. *Opt. Express*, 15(17):10767–10781, 2007.

[47] Dianwen Zhang, X.-C. Yuan, S. C. Tjin, and S. Krishnan. Rigorous time domain simulation of momentum transfer between light and microscopic particles in optical trapping. *Opt. Express*, 12(10):2220–2230, 2004.

[48] K. S. Yee. Numerical solution of initial boundary value problems involving Maxwell's equations in isotropic media. *IEEE Trans. Antennas Propag.*, 14(3):302–307, 1966.

[49] P. Török, P. R. T. Munro, and E. E. Kriezis. Rigorous near- to far-field transformation for vectorial diffraction calculations and its numerical implementation. *J. Opt. Soc. Am. A*, 23(3):713–722, 2006.

[50] J. A. Stratton and L. J. Chu. Diffraction Theory of Electromagnetic Waves. *Phys. Rev.*, 56:99–107, 1939.

[51] C. W. McCutchen. Generalized Aperture and the Three-Dimensional Diffraction Image. *J. Opt. Soc. Am.*, 54(2):240–244, 1964.

[52] C. W. McCutchen. Generalized aperture and the three-dimensional diffraction image: erratum. *J. Opt. Soc. Am. A*, 19(8):1721–1721, 2002.

[53] J. W. Goodman. *Introduction to Fourier Optics*. Roberts & Company, 3th edition, 2005.

[54] J. D. Jackson. *Classical Electrodynamics*. John Wiley and Sons, USA, 3th edition, 1999.

[55] R. M. A. Azzam, I. M. Elminyawi, and A. M. El-Saba. General analysis and optimization of the four-detector photopolarimeter. *J. Opt. Soc. Am. A*, 5(5):681–689, 1988.

[56] J. Scott Tyo. Design of optimal polarimeters: maximization of signal-to-noise ratio and minimization of systematic error. *Appl. Opt.*, 41(4):619–630, 2002.

[57] Antonello De Martino, Yong-Ki Kim, Enric Garcia-Caurel, Blandine Laude, and Bernard Drévillon. Optimized Mueller polarimeter with liquid crystals. *Opt. Lett.*, 28(8):616–618, 2003.

[58] S. Ben Hatit, M. Foldyna, A. De Martino, and B. Drévillon. Angle-resolved Mueller polarimeter using a microscope objective. *Phys. Status Solidi A*, 205(4):743–747, 2008.

[59] Chas N. Archie, editor. *Mueller polarimetry in the back focal plane*, volume 6518 of *Metrology, Inspection, and Process Control for Microlithography XXI*. SPIE, Proc. of SPIE, 2007.

[60] Klas Lindfors, Arri Priimagi, Tero Setälä, Andriy Shevchenko, Ari T. Friberg, and Matti Kaivola. Local polarization of tightly focused unpolarized light. *Nat. Photonics*, 1:228–231, 2007.

[61] Marcel Leutenegger, Ramachandra Rao, Rainer A. Leitgeb, and Theo Lasser. Fast focus field calculations. *Opt. Express*, 14(23):11277–11291, 2006.

[62] Weibin Chen and Qiwen Zhan. Three-dimensional focus shaping with cylindrical vector beams. *Opt. Commun.*, 265:411–417, 2006.

[63] Ayman F. Abouraddy and Kimani C. Toussaint. Three-dimensional polarization control in microscopy. *Phys. Rev. Lett.*, 96(15):153901–(1–4), 2006.

[64] Farnnaz Massoumian, Sanaz Alali, and Taha Mansouri. Evolutionary algorithm for solving the inverse problem of finding the incident field on a high-aperture lens for generating a desired focused field. *Opt. Lett.*, 34(1):67–69, 2009.

[65] Joseph J. M. Braat, Peter Dirksen, Augustus J. E. M. Janssen, and Arthur S. van de Nes. Extended Nijboer-Zernike representation of the vector field in the focal region of an aberrated high-aperture optical system. *J. Opt. Soc. Am. A*, 20(12):2281–2292, 2003.